U.PORTO

FEUP FACULDADE DE ENGENHARIA
UNIVERSIDADE DO PORTO

Master Thesis in Mechanical Engineering

Development of an Additively Manufactured Bio-structure for Impact Absorption in Vehicles

Author:

Luís Pedro Fernandes Garrido

Supervisor:

Prof. Dr. Eduardo A. S. Marques

Co-Supervisors:

Dr. Mehdi M. Kasaei

Dr. Ricardo J. C. Carbas

Prof. Dr. Lucas F. M. da Silva

Master in Mechanical Engineering

Porto, July 2023

Acknowledgements

Firstly, I would like to express my gratitude to my supervisor, Eduardo Marques, for the opportunity to be a part and work on this project, constant availability and the always optimistic way of facing problems.

A special thanks to my co-supervisor, Mehdi Kasaei, for the guidance and expertise shared along the course of this work, along with the constant availability and patience to help me.

I would also like to thank all of the members of the AJPU unit for the tips and knowledge share. In one way or another, all helped me to achieve the objectives of this project.

To all my friends, with which so much time was spent and many great memories were made during this long academic journey, thank you for being my second family.

Finally, to my family and Ana, a thank you is not enough to express the gratitude for the unconditional support that you gave me along this journey.

Abstract

Due to the high number of fatalities, the effort to increase road safety has been great in the last few years. Furthermore, there has been a high demand for making vehicles more sustainable and eco-friendlier. The development of optimized, light-weight energy absorption structures (EAS) that can be incorporated in vehicles to attenuate the impact of a collision, while decreasing the emission of CO_2 by reducing the weight of a vehicle, can contribute to both safety and sustainability. Bio-structures, such as honeycombs or spider webs, are naturally designed to endure foreign solicitations, and serve as inspiration for high performance mechanical structures. On the other hand, functionally graded structures have proved to enhance load-bearing efficiency and overall crashworthiness. Moreover, the employment of these can also be a way of reducing the mass of a structure.

This study aims to develop and assess the crashworthiness of a bio-inspired multi-material and a single material graded EAS. Fused deposition modelling (FDM) technology is employed as the mean of production due to the freedom of design that it allows, and possibility to manufacture of complex parts in a variety of thermoplastics. Adhesive bonding was used to join sections of different materials.

A tensile characterization of different materials was made in order to select the ones with the most promising mechanical properties to integrate an energy absorption structure. Among the tested, polycarbonate (PC), polyethylene terephthalate glycol (PETG), and thermoplastic polyurethane (TPU) emerged has the most promising. Based on the tensile tests, a numerical model, able to predict the behaviour of complex 3D printed structures under compression, was developed. This model resorted to the Hill's yield model to translate the anisotropic behaviour of such structures. An Abaqus® subroutine was employed to possibilitate the prediction of fracture, according to multiple ductile damage criteria. A reference EAS was developed and tested to compression, for validation of numerical model.

Furthermore, experimental quasi-static, high-rate and impact test were performed on the designed single and multi-material EAS, and a comparison regarding the crashworthiness potential was made, taking into account various performance parameters.

The novelty of this work resides in the development of a numerical tool capable of accurately capturing the deformation behaviour and failure modes of complex geometry 3D printed polymeric structures, under different loading conditions. Furthermore, the design and testing of a multi-material honeycomb structure and as a spider web graded provide new insights about the potential of these geometries and configurations for integration in energy absorption applications. The experimental and numerical analysis performed in this work intends to positively contribute to the ongoing research on this field, providing further tools and data for the development of optimized energy absorption structures for implementation in vehicles.

Resumo

Devido ao elevado número de fatalidades, o esforço para aumentar a segurança rodoviária tem sido significativo nos últimos anos. Além disso, há uma emergente necessidade de tornar os veículos mais sustentáveis e ecologicamente amigáveis. O desenvolvimento de estruturas de absorção de energia (EAE) otimizadas e leves, que possam ser incorporadas em veículos para atenuar o impacto de uma colisão, ao mesmo tempo em que reduzem a emissão de CO_2 através da diminuição do peso do veículo, pode contribuir tanto para a segurança quanto para a sustentabilidade. Estruturas biológicas, como favos de mel ou teias de aranha, são naturalmente projetadas para suportar solicitações externas e servem de inspiração para estruturas mecânicas de alto desempenho. Por outro lado, estruturas com gradiente funcional das propriedades mecânicas têm se mostrado capazes de melhorar a eficiência de suporte de carga e de atenuação de impacto. Além disso, a utilização dessas estruturas pode ser uma forma de reduzir a massa destas.

Este estudo tem como objetivo desenvolver e avaliar a capacidade de absorção de impactos de duas estruturas funcionalmente gradadas, inspiradas na natureza: uma estrutura multi-material e uma que incorpora apenas um único material. A tecnologia de modelagem por deposição fundida (FDM) foi utilizada como meio de produção devido à liberdade de design que permite, bem como a possibilidade de fabricação de peças complexas em uma variedade de termoplásticos. A união adesiva foi utilizada para unir seções de diferentes materiais.

A caraterização de diferentes materiais, à tração, foi realizada de forma a permitir a seleção daqueles com as propriedades mecânicas mais promissoras para integrar uma estrutura de absorção de energia. Entre os materiais testados, o policarbonato (PC), o polietileno tereftalato glicol (PETG) e o poliuretano termoplástico (TPU) surgiram como os mais promissores. Com base nos testes de tração, foi desenvolvido um modelo numérico capaz de prever o comportamento de estruturas complexas impressas em 3D sob compressão. Esse modelo recorreu ao modelo de Hill para traduzir o comportamento anisotrópico dessas estruturas, e uma sub-rotina do Abaqus® foi utilizada para prever a fratura, de acordo com vários modelos de dano dúctil. Uma estrutura de referência foi desenvolvida e testada à compressão para validação do modelo numérico.

Finalemnte realizados testes experimentais quase-estáticos e de impacto nas EAS de material único e múltiplo desenvolvidas, e foi feita uma comparação em relação à capacidade de absorção de impacto.

A análise experimental e numérica realizada neste trabalho visa contribuir de forma positiva para a pesquisa em curso nesta área, fornecendo ferramentas e dados adicionais para o desenvolvimento de estruturas de absorção de energia otimizadas, para implementação em veículos.

Contents

List of Figures

List of Tables

List of Acronyms

ABS	Acrylonitrile Butadiene Styrene
AM	Additive Manufacturing
CFE	Crushing Force Efficiency
EAS	Energy Absorption Structure
FDM	Fused Deposition Modelling
FFF	Fused Fillament Fabrication
MCF	Mean Crushing Force
PCF	Peak Crushing Force
PC	Polycarbonate
PETG	Polyethylene Terephthalate Glycol
PLA	Polylactic Acid
SEA	Specific Energy Absorption
TPU	Thermoplastic Polyurethane

1 Introduction

1.1 Background and motivation

Contemporary civilization heavily depends on a vast and interconnected global transportation system that facilitates the swift and efficient movement of individuals and goods. Within this expansive network, road transportation plays a crucial role. However, it faces significant safety concerns that have resulted in alarmingly high fatality rates, necessitating dedicated endeavors to enhance road safety. In this regard, there has been an extensive amount of research on novel and enhanced energy absorption structures for implementation in vehicles.

At the same time, there is a noticeable regulatory impetus to enhance the sustainability of vehicles, forcing manufacturers to reduce the CO_2 emissions and moving towards the electrification of these. Hence, the employment of lightweight materials, such as composites, has greatly increased, in detriment of aluminium, steel and other metal alloys. However, these materials are expensive, cannot be used in high-value recycling processes, and lack flexible, high-volume manufacturing techniques. There is so an utmost necessity for sustainable, environment friendly solutions that can withstand the required loads.

In addition to the material, geometry tuning can also be an efficient way for performance enhancement and reduction of weight of energy absorption structures. For many times has nature inspired the human being to create high performance engineering features. Bio-structures are naturally designed to be able to endure and damp foreign solicitations, and so the integration of these on energy absorption structures has been studied. Furthermore, functional structural grading can enhance the crashworthiness performance of such structures and improve their energy absorption efficiency, as well as contributing to their lightweight.

However, such complex structures are not possible to manufacture through traditional processes. Due to the design freedom that it allows, additive manufacturing, commonly known as 3D printing, stands out as an optimal manufacturing method for the production of intricate parts. Moreover, adhesively bonded parts can also contribute to a more feasible solution, contributing to design freedom and a safer uniform stress distribution.

With this in mind, the development of a 3D printed bio-inspired energy absorption structure with a functionally graded stiffness was conducted in this study, resorting to fused deposition modelling (FDM) technology.

1.2 Objectives

The present thesis had the following main objectives:

- Characterization of the candidate materials and assessment of the influence of the raster orientation on the mechanical properties of the printed parts, in order to select the ones with better characteristics to integrate a energy absorption structure.
- Design of a single material graded EAS and behaviour characterization under quasi-static compression, high-rate compression and impact.
- Design of a multi-material EAS and behaviour characterization under quasi-static compression, high-rate compression and impact.
- Assessment of the crashworthiness performance of the developed structures.
- Development of a numerical model capable of accurately simulating the compression behaviour of complex structures.

1.3 Research methodology

To achieve the mentioned objectives, the following research methodology was followed:

- Carrying out a literature review mainly focused on the state of art of energy absorption structures and the employment of 3D printing in their manufacturing.
- Execution of mechanical tests on 3D printed parts under different regimes, namely quasi-static, high-rate and impact.
- Employment of anisotropy and ductile damage models to numerically simulate 3D printed structures under different loading conditions.
- Assessment of the crashworthiness performance of the developed structures.
- Assessment of the effect of functional grading and geometry on the behaviour under compression of 3D printed energy absorption structures.

1.4 Thesis outline

This thesis is divided is divided in seven main parts. This introductory part describes the background and motivation for the development of the thesis, as well as the key objectives and the main employed methods to achieve them.

Chapter 2 consists of a literature review and it focuses on the fused deposition modelling 3D printing technology, the materials employed in it and the influence of the printing

parameters on the obtained mechanical properties. A review on energy absorption structures, the materials and geometries employed, the influence of functional grading, and the criteria used to assess crashworthiness is also done.

Chapter 3 clarifies the experimental procedures used throughout this work. The materials, geometry and manufacturing specifications of the 3D printed specimens used for testing are detailed. Furthermore, the testing setup is also described.

Chapter 4 describes the material modelling procedure and specifications of the performed numerical analysis, such as boundary conditions, mesh and failure criteria employed.

Chapter 5 overviews the main results of the study and chapter 6 outlines the main conclusions that were taken from it.

Finally, as appendixes, two papers are presented. While the first consists of the characterization and numerical modelling of 3D printed parts, the second addresses the development of two bio-inspired energy absorption structures and the influence of geometry and stiffness grading on its crashworthiness.

2 Literature review

2.1 3D printing

2.1.1 General considerations

Additive manufacturing (AM) technologies, commonly known as three-dimensional (3D) printing, first started being brought to light in the 1980s. The increase in research on this field led to a rapid evolution of the 3D printing technologies, being that in the last recent years there has been an exponential step forward with the additive manufacturing market growing beyond projections [1].

3D printing has become an essential tool for rapid prototyping and production of complex shape parts, in a wide variety of materials. It accelerates the product development process by allowing the fast and cost-effective production of prototypes. This helps in iterative design improvements and reduces the time-to-market. When compared to traditional manufacturing processes, 3D printing technologies allow the production of components with a much higher degree of intricacy and with near net shape, substantially reducing material wastage. The dimensional accuracy can also be improved when resorting to additive manufacturing technologies. However, these pose some challenges too. One of them is the fact that these require a high manufacturing lead time, not being suitable to high volume production [2]. Nevertheless, these are used in a wide variety of industries and applications ranging from robotics to medical purposes, such as prostheses production.

2.1.2 Fused deposition modelling (FDM)

There are many additive manufacturing technologies, such as fused deposition modelling (FDM), electron beam melting (EBM), selective laser sintering (SLS), multi jet fusion (MJF), and stereolithography (SLA). These differ from each other mainly on the printing mechanism and physical form of raw materials. Among the stated, FDM technology is the most widely implemented due to its process simplicity, cost-effectiveness, and high printing speed. FDM printers use a thermoplastic filament that is heated to its melting temperature and extruded layer-by-layer to create a 3D structure. Firstly, a 3D model should be created with a computer aided design (CAD) software, and then sliced in thin layers with a slicing software. The printing parameters may also be set in this stage. This model will be printed layer-by-layer as the thermoplastic filament is heated by the nozzle and extruded in a controlled manner. Depending on the 3D printer, the extruder or print bed move vertically to accommodate the three-dimensional part.

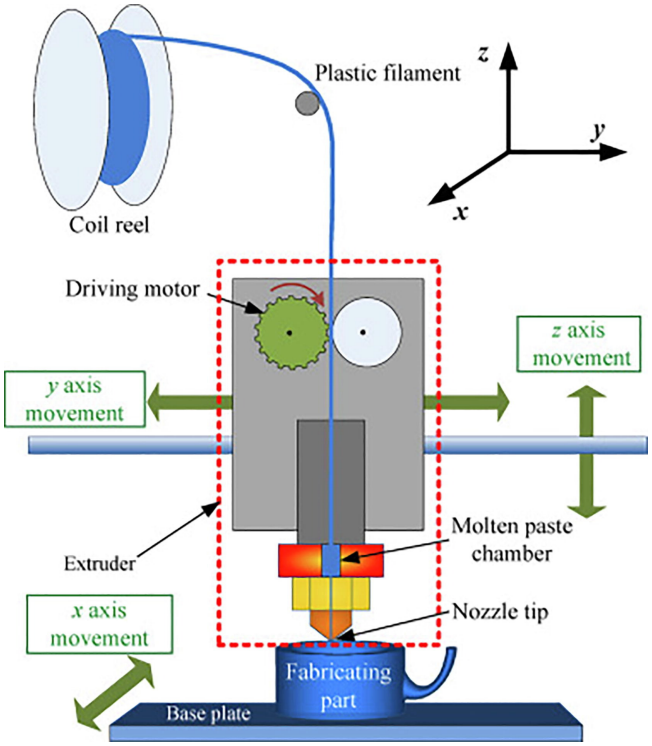

Figure 1: FDM process representation scheme [2].

2.1.3 Materials

Fused deposition modelling technology uses thermoplastics to produce 3D parts. Thermoplastics are easily processed since these have low melting points, and can be repeatedly melted and solidified without suffering significant chemical changes nor degradation of the mechanical properties. A wide range of thermoplastics can be used when printing with FDM. Amongst the most common are acrylonitrile butadiene styrene (ABS), polycarbonate (PC), polyethylene terephthalate glycol (PETG), polylactic acid (PLA) and thermoplastic polyurethane (TPU).

ABS is widely used in FDM printed parts. Its dimensional stability and low glass transition temperature favour its processability by this technology. High impact resistance, toughness, and moderate strength are some the mechanical properties that characterize this copolymer [3].

Polycarbonate (PC) is used in a wide variety of engineering applications. Its high strength and inertness provide resistance to harsh environments and make it suitable for optical, medical, electronic, and aeronautical purposes [4].

PETG is an amorphous copolymer of PET, that differs from the latter by having present an additional glycol group along the copolymerizing agent, PCT. While PET is used in many high-volume commercial and consumer applications, due to its ability to crystallize upon deformation at the subjected temperatures and strain rates during the processing, PETG does not have the ability to undergo strain induced crystallization.

PETG presents good chemical resistance, durability and formability, as well as higher strength and impact resistance than PET. The low forming temperature that it requires makes it suitable for 3D printing and other heat-forming processes [5].

PLA is one of the most used materials in FDM 3D printing due to its ease in being thermally processed. Its low warping behaviour provides good dimensional accuracy to the printed parts, whereas the multicolour and furnished appearance make the parts visually attractive. Moreover, it has the advantage of being a sustainable material since it is biodegradable and recyclable. On the other hand, its poor mechanical properties, such as low strength, low toughness, and high brittleness, make this material not suitable for structurally demanding applications [6].

TPU is a thermoplastic elastomer. It combines the properties of vulcanized rubber with the processability of thermoplastic polymers. It is widely used due to its high tensile strength, abrasion and tear resistance, oil and solvent resistance, low-temperature flexibility, and paintability [7].

2.1.4 Mechanical properties

The quality and mechanical properties of FDM 3D printed parts depend on the set printing parameters, such as printing speed, nozzle and heat bed temperatures, layer thickness, infill density, and orientation of material deposition (raster angle). The latter has great influence on the mechanical properties, being that the best tensile properties are obtained when a part is printed by extruding the filament in a parallel orientation to the applied force [8–10]. During the material deposition, the newly extruded filament is not able to completely melt the adjacent layers, causing weak interlayer bonding. Hence, the interlayer regions act as discontinuities that promote the premature failure of a part when loaded perpendicularly to the printing direction [11].

Furthermore, FDM printed parts are prone to some defects that can affect their properties and appearance, like high surface roughness, void content and warping. The occurrence of these can be reduced by correctly tuning the printing parameters. A lower layer thickness will reduce the staircase effect and, consequently, the surface roughness, as well as reduce the air gaps and void content. Adequate temperatures of the heat bed and nozzle will also reduce the occurrence of internal stresses and consequent warping or layer separation, by maintaining a uniform temperature gradient [12].

Multiple studies have been focused on determining the optimal parameters for 3D printing. Studies conducted on the influence of these parameters on printed parts determined that the tensile strength increases with the increase of infill density [2, 8, 13]. The infill pattern was also stated as influencing the surface quality of printed parts [2]. Moreover, the tensile strength was reported as reaching its maximum when the raster orientation is parallel to the applied force [8]. This improvement in the obtained mechanical

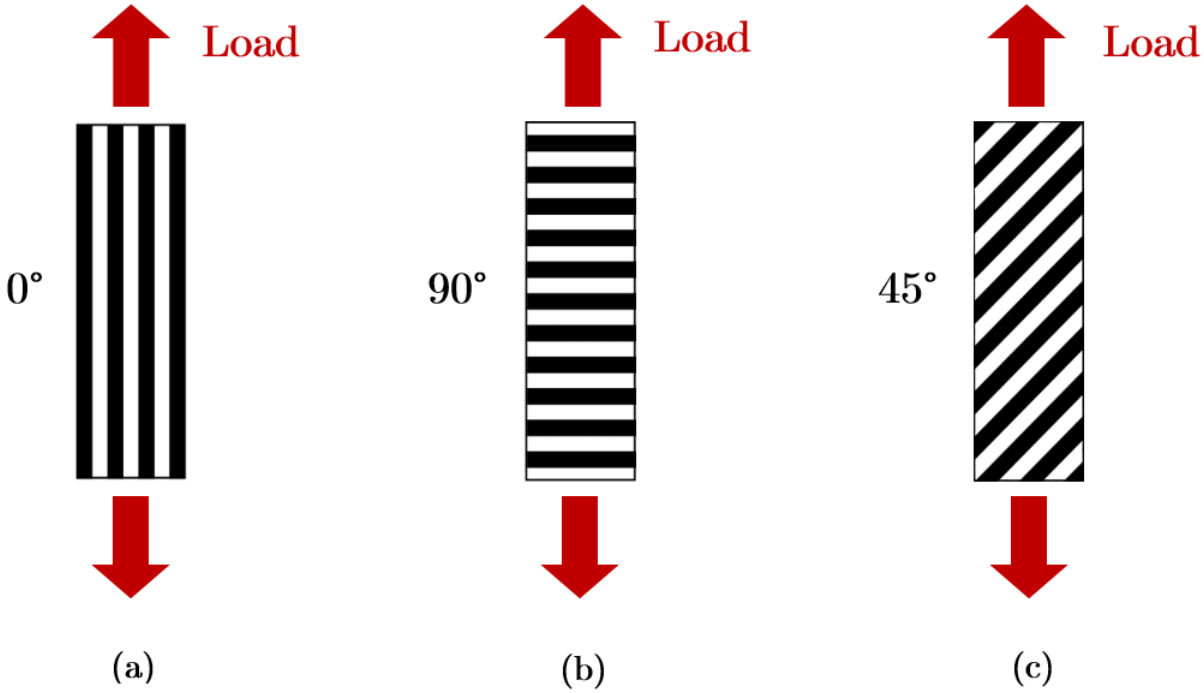

Figure 2: Representation of different raster angles.

properties when the raster angle is 0° was also stated in a torsion analysis of ABS printed specimens, conducted in [9]. The tensile strength is also enhanced by increasing layer height [13]. However, a lower layer height can be an effective way of reducing the volume of printing defects [14].

There are a great number of printing parameters and these should be tuned in order to decrease the number of defects and enhance mechanical properties of printed parts, having in mind that a trade-off may be imposed when setting them. Moreover, the adequate parameters will vary according to the application and requirements of the component.

2.2 Adhesive bonding of FDM 3D printed parts

Along with the benefits and advantages that come from the use of 3D printing, when comparing to traditional processes, come some limitations that hamper its widespread industrial acceptability. One of those is the limited printing volume. Adhesive bonding can play a major role on mitigating this by allowing the joining of different parts. In this kind of bonding, intermolecular forces develop between the 3D printed parts and the adhesive, resulting in a joint [15]. Adhesive joining allows a uniform stress distribution along the bond line, corrosion resistance, good damping properties, and good thermal and electric insulation, making this type of bonding very attractive. Furthermore, it can be used to bond dissimilar 3D printed parts, being a solution when multi-material printing isn't possible.

However, the extensive preparation of the areas to be bonded that is required sets one

of the major drawbacks regarding the employment of adhesive bonding on 3D printed parts. The research conducted in [16] studied the effect of surface treatments, such as sanding and plasma, on the bond shear strength of 3D printed high performance polymers (PEEK, PEI and PEEK/CF). Two adhesive were employed in joint fabrication: an epoxy film adhesive and a two-part epoxy liquid adhesive. It was concluded that both sanding and plasma treatment enhanced the bond strength of the joints, being that the second had a more pronounced effect on this properties. Furthermore, more pronounced improvements were obtained when employing the liquid adhesive, aspect attributed to its better wettability.

The selection of the adhesive should be done regarding its compatibility with the substrate's material. In [17], the shear strength of 3D printed Acrylonitrile Styrene Acrylate (ASA) and Nylon 12 Carbon Fiber (NCF) adhesively bonded joints was evaluated. A cyanoacrilate and an epoxy adhesives were employed. The latter was determined to be unsuitable to join the tested materials, due to poor bondability. The cyanoacrilate adhesive revealed to be suitable for bonding ASA adherends, whereas full printed NCF specimens showed a substantially higher strength than the bonded counterparts. On the other hand, J.M. Arenas et al. [18] conducted a multi-criteria analysis for the selection of the most adequate structural adhesive for joining ABS 3D printed parts via FDM technology, based on suitability, economic and technological aspects. Among the epoxy, silicone, cyanoacrilate, polyurethane and acrylics tested adhesives, the last two were determined to be the best options to bond ABS parts.

The integrity of 3D printed bonded joints depends not only on the employed substrate material and adhesive, but also on the set printing parameters. The influence of these were studied in [19], where 3D printed PETG single lap joints (SLJ), under different printing parameters, were tested to quasi-static tension. Among the range of the studied parameters, a 0°raster angle and a raster width of 1 mm (over a raster width of 0.75 mm) were determined as granting the most favourable mechanical properties regarding strength. Moreover, in all cases, a thinner adhesive layer contributed to enhanced mechanical properties.

2.3 Energy absorption structures

2.3.1 Crash box

In what concerns vehicle design and engineering, the capacity of managing and attenuating the energy transmitted by a collision is a key factor for vehicle safety. The integration of energy absorption structures has become a practical mean to reduce the harm caused by accidents, and increase passenger safety. These structures are intended to deform and absorb the energy in a controlled manner, thereby reducing the force transmitted to the occupants. These are distributed by the vehicle and consist on specially engineered parts

that can be in the form of collapsible structures, crumple zones, or impact beams.

Amongst the energy absorption features of a vehicle, there is the crashbox. It consists on a deformation device that is mounted between the front rail and bumper of the car, to reduce the damage caused by low-speed crashes. During a collision, crashboxes must collapse prior to adjacent structures, in order to dissipate the kinetic energy and minimize the damage inflicted to the cabin and passengers [20].

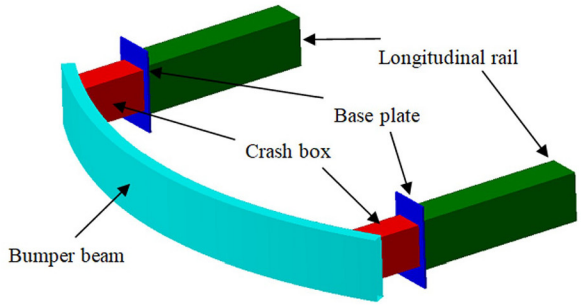

Figure 3: Frontal impact absorption features of a vehicle.

2.3.2 Materials

In what concerns the materials used in crash box structures, these are traditionally made of steel or aluminium, being that the latter is the most common material to integrate in these applications due to its lightweight, yet strong profile.

Weight-saving demands in the automotive industry have lead manufacturers to invest in new structure designs and implementation of new materials with crashworthiness potential [21]. A potential reduction in weight of such structures allows a greater fuel efficiency and helps to reduce the ecological footprint caused by polluting gases emissions, while a more efficient energy absorption contributes to vehicle safety and can help to reduce road fatalities. The implementation of composites and hybrid materials on these energy absorption structures can be an effective way to achieve this.

Studies on the development of a glass reinforced plastic EAS, and the influence of different geometries on the rate of energy absorbed, when subjected to axial crush loading are reported in [21]. Furthermore, a hybrid aluminium/CFRP cylindrical EAS was compared to aluminium and CFRP net structures when submitted to different quasi-static loading angles [22]. Also, natural fibres have been being studied for a long time as substitutes of synthetic fibres, for a more environmentally friendly production. Hemp was considered as a promising candidate for sustainable energy absorption structures, with hemp fibre composite and carbon fibre composite structures obtaining similar specific energy absorption (SEA) values [23].

2.3.3 Geometry

Along with material properties, geometry is the most influencing parameter on the efficiency of the absorption of the kinetic energy transmitted by a collision. Hence, multiple studies have been conducted on testing novel energy absorption structures configurations, integrating non-traditional materials or geometries, such as lattice structures [**?**, 24], honeycomb structures [25–27], and multi-tubular structures [28]. Specially designed features such as foam-filled structures, functionally graded thicknesses or nested tubes have been reported as enhancers of the energy absorption capability of such structures [21].

In [29], a mild-steel pre-deformed EAS was numerically submitted to crushing loads and compared to its non-deformed counterpart. The inclusion of imperfections (triggers) such as grooves or pre-deformations on energy absorption structures, in order to stabilise the deformation and reduce the peak force, has also been indicated as performance enhancer of such structures. These "crash initiators" have been reported has having an significant effect on the energy absorption performance can help reduce the rate of energy absorption, what is desirable for the safety of the passengers.

Moreover, cellular structures, such as honeycombs, are able to dissipate a large amount of energy and so, these have been a topic of interest among the research community. In [30], the hexagonal honeycomb emerged as the most capable of efficient energy absorption,when nine different honeycomb structures were numerically tested to compression.

2.3.4 Functional grading

During the compression of a structure, it first undergoes elastic deformation with a linear load-displacement relation, before yielding. It then enters the crushing phase when there is plastic deformation and collapse of the structure, before being totally compacted and the load values increasing rapidly. The absorbed energy can be calculated by calculating the area below the load-displacement curve (Figure 4). High peak forces might cause deceleration peaks that are harmful to the vehicle and its occupants.

The stiffness grading of an energy absorption structure allows a lower energy absorption rate by decreasing the peak force generated when there is an impact. Hence, the energy dissipated, for the same time period, also decreases. This leads to more stable load values during the compression process and a more phased energy absorption. Consequently, the the stress transmitted to other parts will also be reduced.

The functional grading of these structures, in order to optimize their energy absorption capabilities has been extensively studied. Different size graded lattice/honeycomb single material structures were numerically tested in [31], along with dual-material honeycomb structures. the conclusion was made that the graded structures were effectively more capable of energy absorption, as were the multi-material solutions when compared to their single material counterparts. The same argument was made in [25], where an

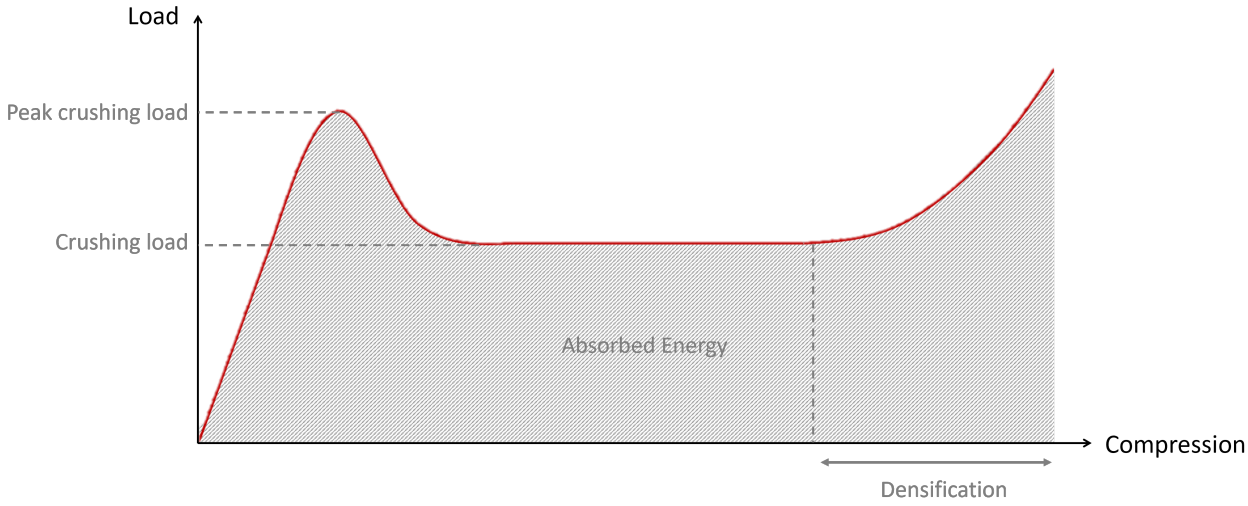

Figure 4: Representative curve of a compression test.

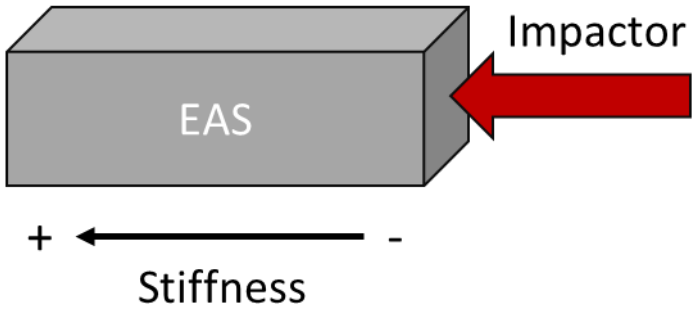

Figure 5: Schematic representation of a graded EAS.

analytical model was used to predict the stress-strain behaviour of 3-stage density graded honeycomb structures. Furthermore, the density grading of a 3D printed (FDM) thermoplastic polyurethane (TPU) honeycomb structure allowed the increase of the densification strain and, consequently, of the total energy absorbed up to that point, when submitted to impact [26]. The retardation of the densification onset allows a more gradual energy absorption and transfers a lower stress to the part being protected. Besides honeycomb cellular structures, other bio-structures such, as bamboo structural core, fish scales or even bone structure, have been studied as potential candidates to integrate an EAS [32].

2.3.5 Crashworthiness criteria

To investigate and quantify the energy absorption capabilities of such structures, multiple indexes should be taken in account. In [33], the specific energy absorption (SEA) and crushing force efficiency (CFE) were calculated to characterize the crashworthiness of different thin-walled steel structures. Likewise, these parameters were used in [27] to evaluate the crashworthiness potential of self-similar graded honeycomb-filled composite

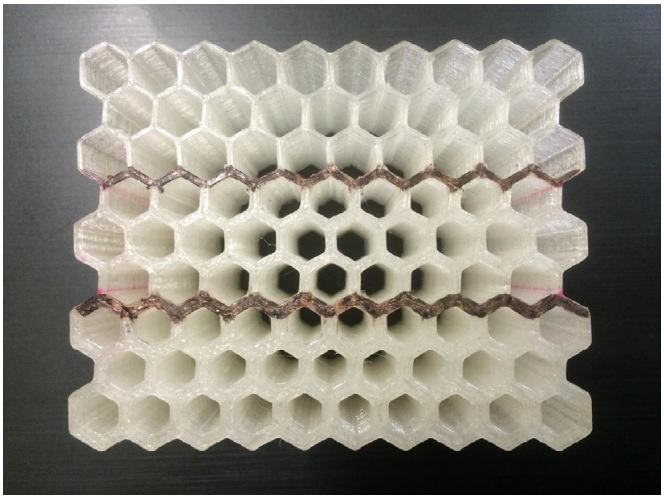

Figure 6: Density graded honeycomb structure [26].

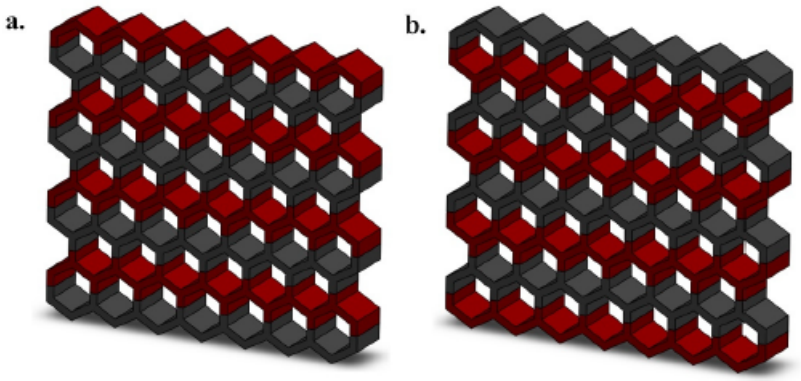

Figure 7: Dual-material honeycomb drawing [31].

circular structures when submitted to bending.

The specific energy absorption (SEA) is a very relevant performance indicator. It quantifies the energy absorbed by a structure during the compression process, per unit of mass. SEA can be calculated by the following equation:

$$SEA = \frac{EA}{m} \tag{1}$$

Where EA corresponds to energy absorbed and m is the mass of the structure. EA can be obtained by integrating the area under the load-displacement curve originated from the compression test:

$$EA = \int_0^{\delta} F(x)\, dx \tag{2}$$

Where δ is the crushing displacement and $F(x)$ is the instant crushing load. On the other hand, the peak crushing force (PCF) corresponds to the highest value of $F(x)$ registered during the compression of a structure, and is directly correlated to the damage caused to a vehicle and its occupants in a collision, being one of the injury-based metrics [27]. An excessive PCF can lead to injuries and casualties during an impact, due to the high stress that is transmitted to adjacent parts. It is then of great importance, to have a reduced value of this parameter. The crash loading efficiency (CLE) consists on the ratio between the peak crushing force and the mean crushing force (MCF):

$$CLE = \frac{PCL}{MCL} \tag{3}$$

Where MCF can be obtained by the following equation:

$$MCL = \frac{EA}{\delta} \tag{4}$$

The protection is enhanced for a high value of CLE, until a maximum of 1 when $PCL = MCL$.

3 Experimental procedures

In the following chapter, the experimental procedures used in this study are described.

3.1 Materials

In this study, five polymers (thermoplactics) were considered:

- Acrylonitrile butadiene styrene (ABS);
- Polycarbonate (PC);
- Polyethylene terephthalate glycol (PETG);
- Polylactic acid (PLA);
- Thermoplastic polyurethane (TPU).

These are typically used when 3D printing with FDM technology, and were selected based on their availability. Table 1 shows the mechanical properties and recommended printing temperatures for each material, according to the provided suppliers' technical data sheet.

Although all these materials were experimentally characterized, only three of them - PC, PETG and TPU - were selected to proceed with the study and be integrated in the developed energy absorption structures.

Furthermore, Plexus MA590, a two-part methacrylate adhesive designed for structural bonding of thermoplastics, composite and metal assemblies, was used to bond the different parts of the developed multi-material honeycomb EAS. Table 2 shows the tensile properties of the adhesive, according to the supplier's technical data sheet.

Table 1: Mechanical properties and printing temperatures of the considered thermoplastics (obtained from suppliers' data sheet).

	Filament PM ABS-T	Prusament PC Blend	Prusament PETG	Prusament PLA	Fillamentum Flexfill TPU 98A
Young's modulus (GPa)	-	1.9 ± 0.1	1.5 ± 0.1	2.3 ± 0.1	-
Yielding stress (MPa)	-	63 ± 1	47 ± 2	59 ± 2	-
Tensile stress at break (MPa)	-	-	-	-	53.7
Elongation at yield (%)	-	5.8 ± 0.3	5.1 ± 0.1	3.2 ± 1.0	-
Elongation at break (%)	-	-	-	-	318
Nozzle temperature (° C)	230-250	275 ± 10	250 ± 10	210 ± 10	220-240
Build plate temperature (° C)	100-110	110 ± 10	80 ± 10	40-60	50-60

Figure 8: Plexus MA590 adhesive.

Table 2: Tensile mechanical properties of Plexus MA590 adhesive (obtained from suppliers' data sheet).

Strength (MPa)	Modulus (MPa)	Strain to failure (%)
13.8 - 17.2	482 - 827	> 130

3.2 Specimens manufacturing

3.2.1 Tensile specimens

The tensile tests were conducted with specimens shaped according to BS 2782 standard 9. A tensile specimen was modelled in SolidWorks software. An .stl file was generated and inputted in a slicer software (PrusaSlicer), where the printable G-code file was generated. The Prusa i3 MK3S+ 3D printer was used.

At least 3 specimens were produced for each material and raster orientation (0°, 45° and 90°). The specimens were printed with a 100% aligned rectilinear infill. Since the influence of the raster angle on the mechanical properties was a key point of this study, these were printed without any horizontal top or bottom shells, and with the vertical shell reduced to one perimeter, in order to minimize the effect of features other than the unidirectional infill on the tensile properties of the parts. All the specimens were printed with the same build orientation - flat on the print bed. A representation of the position of the specimens on the print bed is shown in figure 10.

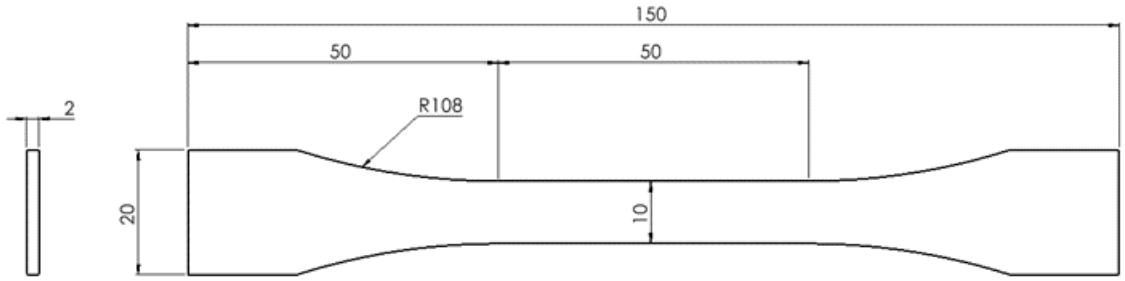

Figure 9: BS 2782 standard tensile specimen geometry (dimensions in mm).

In order to obtain high quality specimens, these were printed at a reduced speed and with a layer height of 0.05 mm, with exception of the first layer that had a height of 0.2 mm to grant improved adhesion and tolerance, by mitigating possible slight leveling errors. The printing temperatures for each material were set according to the default temperatures defined by PrusaSlicer software, being that the nozzle temperatures were increased by 5 °C for each material, to allow a good adhesion between the layers and enhance the properties of the printed specimens.

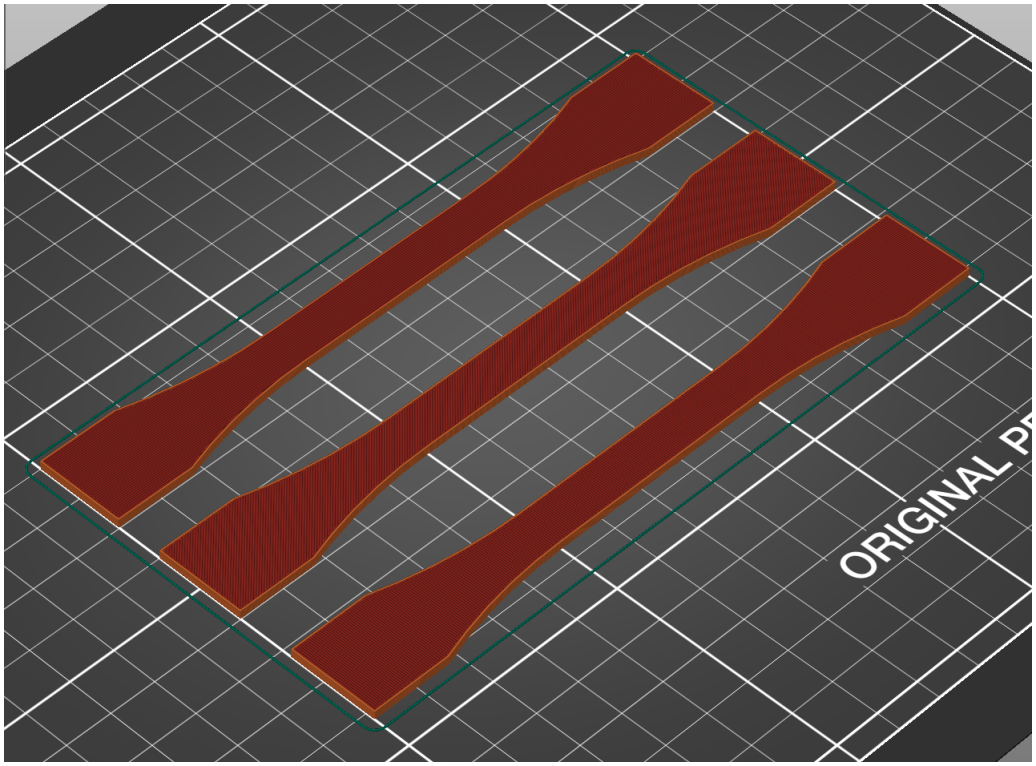

Figure 10: Position of specimens on the print bed.

Table 3: Temperatures set for printing of the specimens.

Material	Printing temperature (°C)	
	Print bed	Nozzle
ABS	110	260
PC	115	280
PETG	90	255
PLA	60	220
TPU	50	245

3.2.2 Reference EAS

The open-cell honeycomb reference structure was modelled in SolidWorks software, from which an .stl file was exported. PrusaSlicer was used to generate the g-code files. Only PC, PETG and TPU were used in the production of these structures.

These were printed in two different build orientations (Figure 12) so its influence on the behaviour under compression could be analysed. At least 3 specimens, for each material and build orientation, were produced. The set printing temperatures were the same as in the tensile specimens production (see Table 3). PC specimens were printed with a

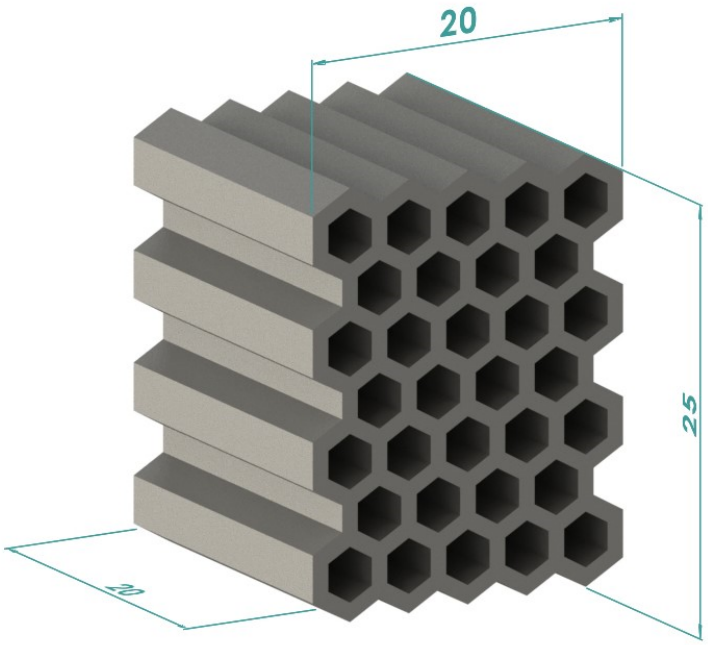

Figure 11: Dimensions (mm) of reference EAS.

high skirt, in order to avoid warping of the structure, by keeping a low the temperature gradient.

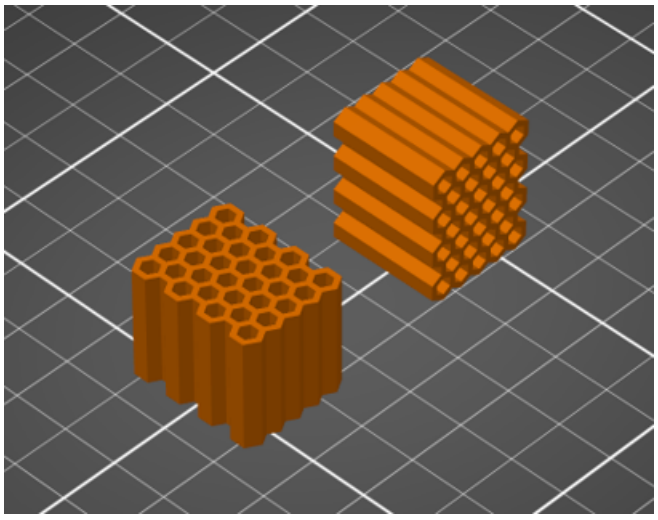

Figure 12: Position of 0° reference EAS (left) and 90° reference EAS (right) on the print bed.

3.2.3 Single material EAS

A graded single material EAS, inspired in the spider web structure was designed. A 3D model was developed in SolidWorks, in which there is a grading of the structural density by increasing the number of nested polygons as we progress along the length of the structure. Each nested polygon that appears along the length of the structure forms a continuous wall until the base of it, decreasing continuously its cross-sectional perimeter in order to accommodate other nested polygon walls is higher stiffness regions.

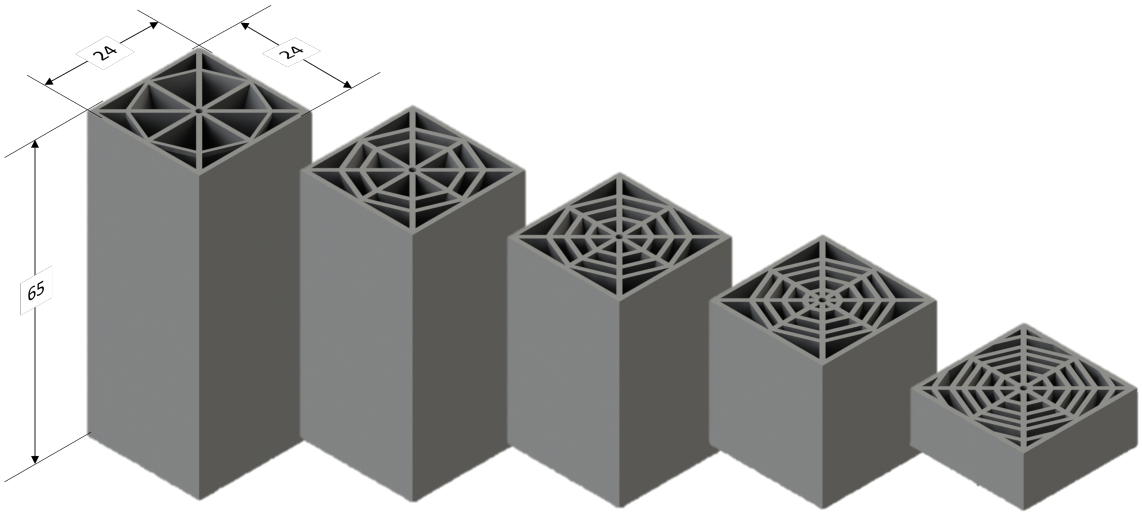

Figure 13: Dimensions (mm) and cross-section views of spider web inspired single-material EAS (3D model).

The slicing and generation of the g-code files were made resorting to PrusaSlicer software. As happened with the reference structure, PC, PETG and TPU were employed in the production of the single material EAS. At least 9 specimens were printed for each material, in order to perform quasi-static, low-rate and impact tests. The specimens were printed vertically, with the face where the stiffness is at its maximum (highest number of spiral structures) flat on the print bed. This build orientation avoided the printing of 90°overhangs, what would possibly lead to printing defects such as stringing and a deformation of the structure's wall.

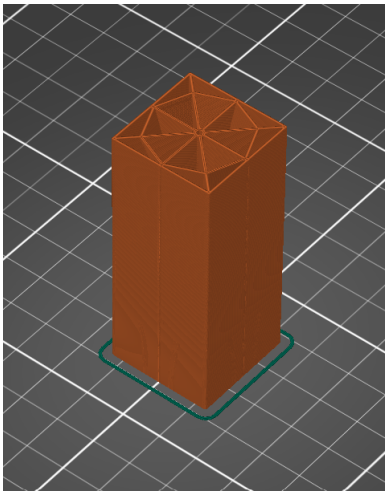

Figure 14: Position of single-material EAS on print bed.

3.2.4 Multi-material EAS

The multi-material EAS consisted of honeycomb-based structures, featuring stiffness grading through the integration of three different materials: PC, PETG and TPU. The order of these in the structure is set by their stiffness, with TPU, the less stiff, being integrated on one end, and PC, the stiffest, on the other of the EAS. PETG, with an intermediate stiffness, composed the middle part.

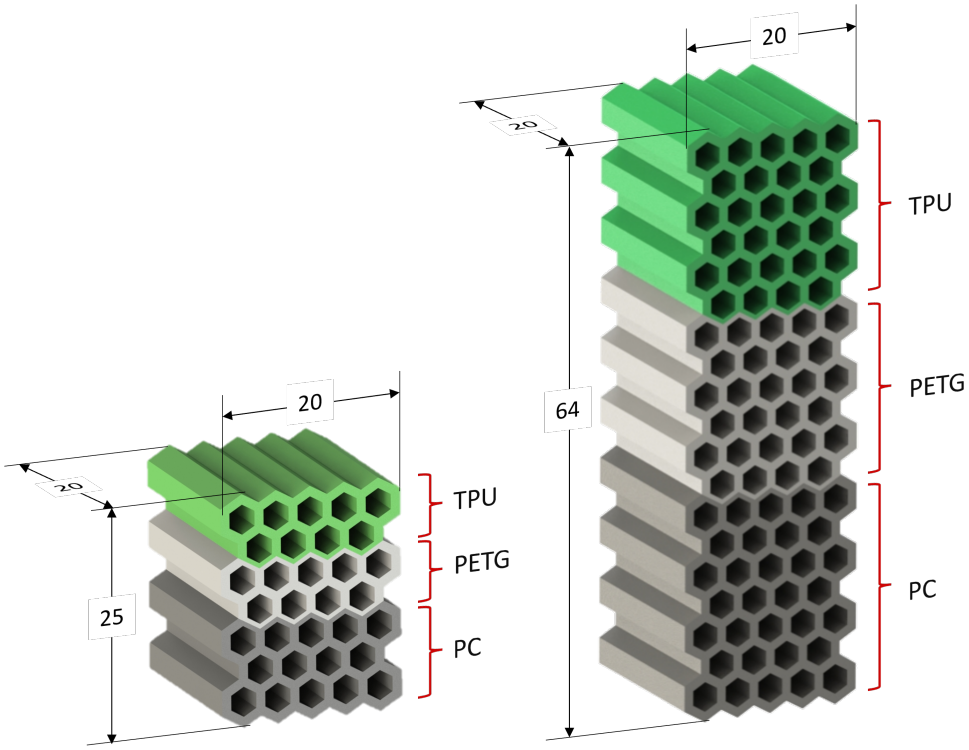

Figure 15: Dimensions (mm) and configuration of multi-material honeycomb EAS.

Similarly the other specimens, SolidWorks and PrusaSlicer softwares were used to

develop the 3D model and generate the G-code file, respectively. Prusa i3 MK3S+ 3D printer was used to produce the parts. Since the printing of the three part structure as one single part was not possible, each material's section was printed separately. These were printed with the honeycomb's in-plane parallel to the print bed, to avoid a brittle behaviour when compressed. At least 9 parts, for each material, were produced, in order to perform quasi-static, low-rate and impact tests on the assembled structures.

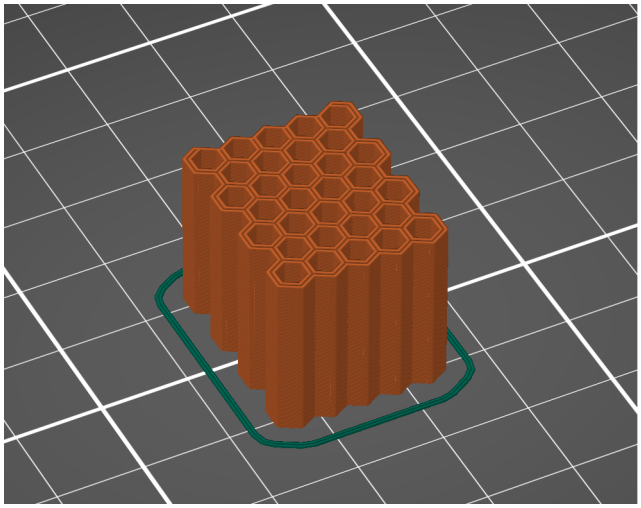

Figure 16: Build orientation of each section of the multi-material's EAS.

The assembly of the final structure was made by means of adhesive bonding. For this effect, the surfaces to be bonded were first subjected to a surface plasma treatment in order to increase surface energy for improved adhesion (Figure 17).

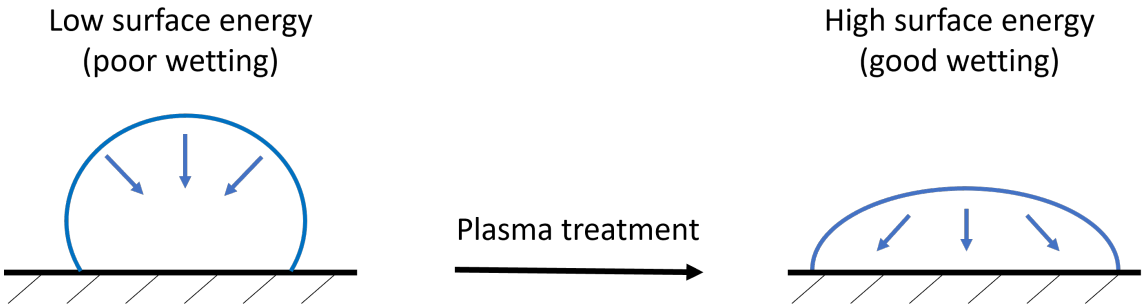

Figure 17: Influence of plasma treatment on surface energy.

After the surface treatment, the Plexus MA590 two-part methacrylate adhesive (Figure 8) was applied to the surfaces. The parts were then joined together and left for the adhesive to cure for at least 24 hours at room temperature before performing the tests.

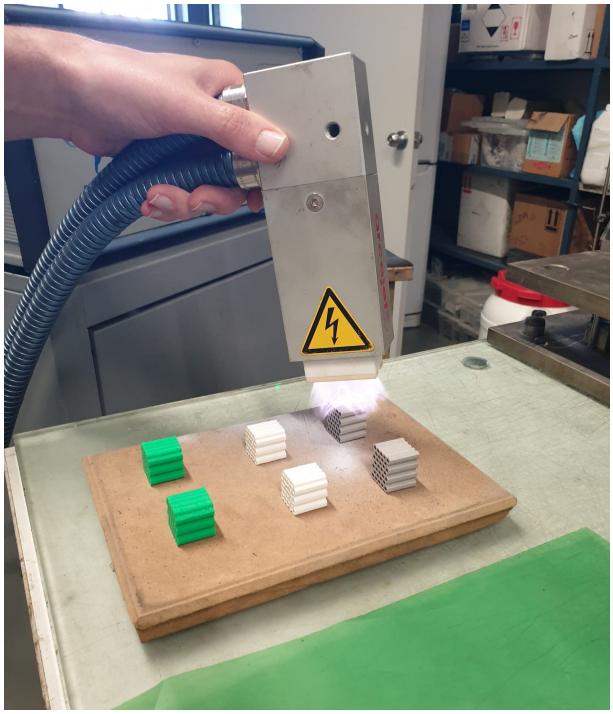

Figure 18: Surface plasma treatment of the surfaces to be bonded.

3.3 Testing setup

Different testing machines were used according to the desired cross-head displacement rate. Tensile and compression quasi-static tests were performed on Instron 3367 universal testing machine equipped with 30 kN load cell. Furthermore, high-rate compression tests were performed on a Instron 8801 servo-hydraulic testing machine, equipped with a 100 kN load cell, at a rate of 0.1 m/min. A drop-weight testing machine was used to perform impact tests.

3.3.1 Bulk tensile testing

The printed specimens were mounted on the universal testing machine and secured with the grips overlapping about 15 mm of each end. An extensometer was then attached to the specimens, to allow a more accurate measurement of the strain. The quasi-static tests would then be initiated and run until the rupture of the specimen occurred.

At least three tensile tests were performed for each material (PC, PETG, PLA, TPU and ABS) and raster orientation (0° 45° and 90°). Through these, the Young's modulus, tensile strength and strain to failure were obtained for each material/raster orientation configuration. Furthermore, the assessment of the anisotropic behaviour of the tested materials was possible.

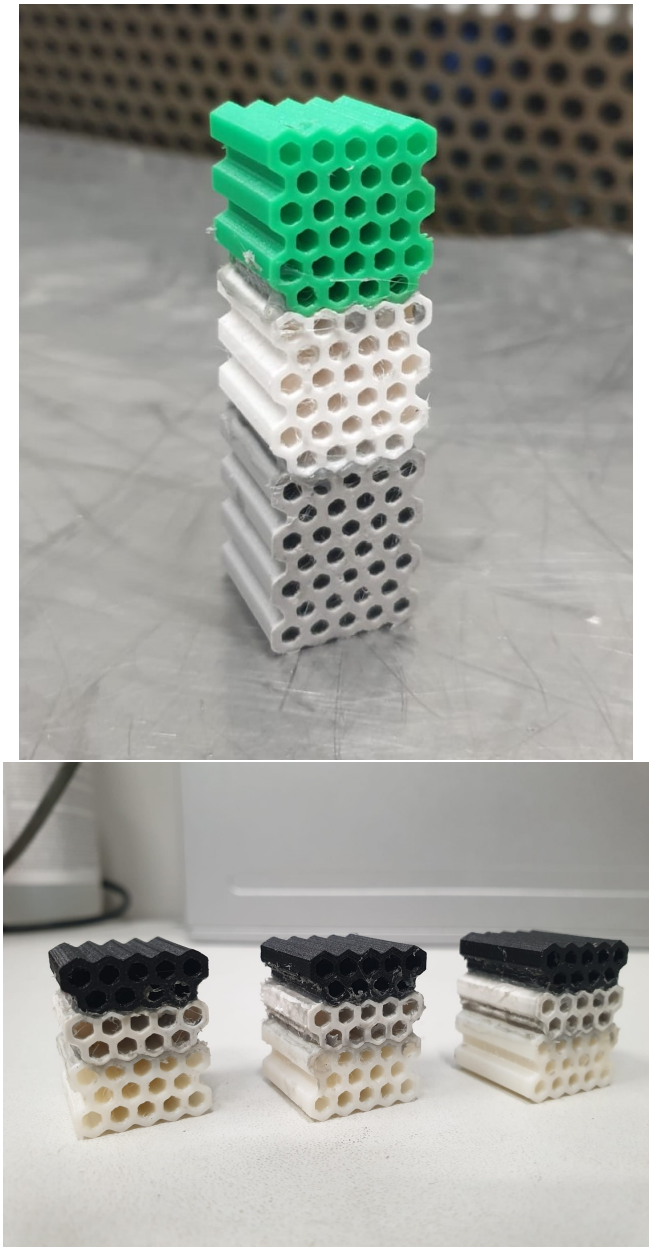

Figure 19: Assembled multi-material EAS.

3.3.2 Quasi-static compression testing

Quasi-static compression tests were performed on the reference EAS, single material EAS and multi-material EAS. The specimens were mounted between two plates on the Instron 3367 universal testing machine and were compressed at a rate of 1 mm/min until the load reached 30 kN, the load cell limit. To better analyse the deformation behaviour of the tested specimens, the tests were recorder in their full extent with a Nikon D5300, equipped with a AF-P DX Nikkor 18-55mm f/3.5-5.6G VR lens.

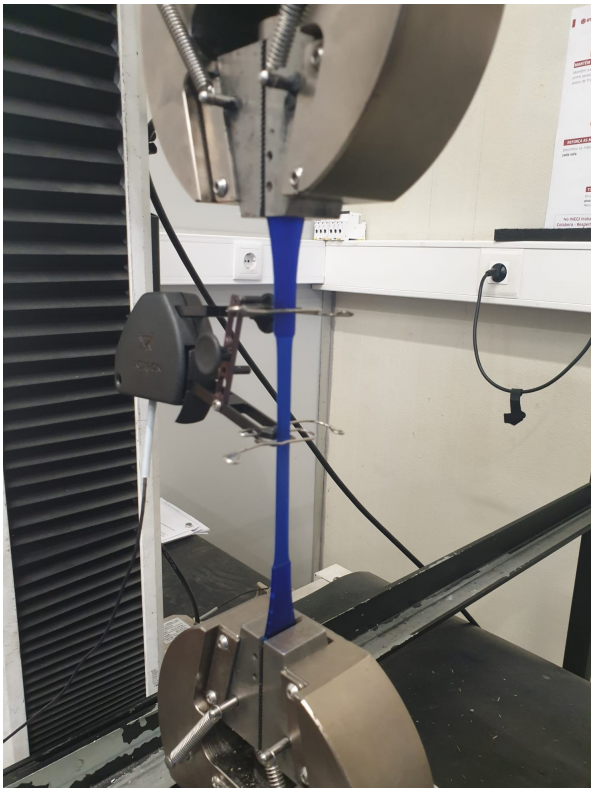

Figure 20: Tensile test apparatus.

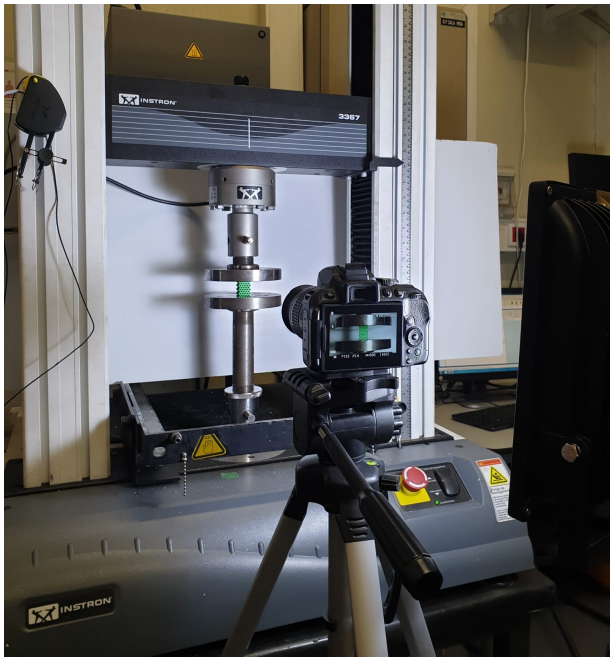

Figure 21: Quasi-static compression test apparatus.

3.3.3 High-rate compression tests

High-rate compression tests were performed on the developed single and multi-material EAS in a servo-hydraulic testing machine. The specimens were mounted between two plates and compressed at a rate of 0.1 m/min. For these to run at until past the onset of

densification, a 50 mm compression was set as the limit displacement of the moving plate. Hence, once the structures had a 50 mm reduction in height the tests would automatically stop. The tests were recorded with a Nikon D5300, equipped with a AF-P DX Nikkor 18-55mm f/3.5-5.6G VR lens.

3.3.4 Impact tests

To assess the energy absorption potential of the developed structures, these were submitted to impact tests in a drop-weight machine. The velocity of impact was set at 3 m/s, being that the impact energy varied according to the structure being tested. For the uniform honeycomb reference structures and their multi-material counterparts, a mass of 9.55 kg was employed, leading to a energy of impact of 42.98 J. On the other hand, for the larger multi-material honeycomb and graded spider web structures, a mass of 27.31 kg was used, leading to a energy of impact of 122,9 J. A high speed camera was used to capture the collapse of the specimens. Figure 22 shows the impact tests apparatus.

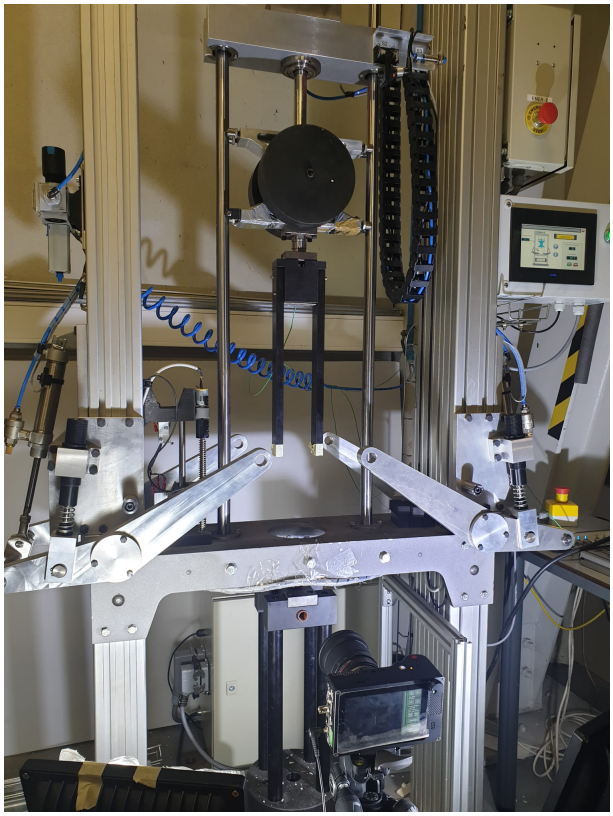

Figure 22: Impact test apparatus.

4 FEM analysis

4.1 General considerations

The development of a numerical model that could predict the behaviour of complex geometry energy absorption structures when submitted to compression was one of the goals of this study.

Firstly, an Abaqus/Explicit model was created and the experimental quasi-static tensile tests were numerically simulated, to calibrate the materials' hardening curves and validate the anisotropy model. An Abaqus subroutine was then employed to determine the damage values for which there was rupture of the specimens - critical damage values -, according to multiple ductile damage criteria. Only the selected materials (PC, PETG and TPU) were considered in the numerical analysis.

The model was validated to compression by numerically simulating the quasi-static compression tests of the reference structure. The obtained critical damage values were inputted to predict the failure onset of the structures during compression. An assessment was made on which ductile damage criterion allowed a more accurate correlation between numerical and experimantal data.

4.2 Anisotropy modelling

The materials' mechanical properties anisotropy was modelled, resorting to the Hill's yield model. In order to employ this model in Abaqus, the following six anisotropy coefficients need to be defined in the property module (Figure 23) - R_{11}, R_{22}, R_{33}, R_{12}, R_{13}, R_{23}. These can be obtained by the following expressions:

$$\frac{1}{R_{11}^2} = (G+H)\,\sigma_0^2, \quad \frac{1}{R_{22}^2} = (H+F)\,\sigma_0^2, \quad \frac{1}{R_{33}^2} = (F+G)\,\sigma_0^2, \quad \frac{3}{2R_{12}^2} = N\sigma_0^2,$$

$$\frac{3}{2R_{13}^2} = M\sigma_0^2, \quad \frac{3}{2R_{23}^2} = L\sigma_0^2$$

Where parameters F, G, H, L, M and N depend on the state of anisotropy. The calculated coefficients are shown in Table 4.

4.3 Quasi-static tensile tests

For the tensile test simulation, the specimen geometry was created. The end portions were the specimen would be clinched by the grips were left out, since these are not strained during the experimental test. Furthermore, a reference point, from which reaction force and displacement history output values could be obtained, was defined.

Table 4: Calculated anisotropy coefficients.

Material	R_{11}	R_{22}	R_{33}	R_{12}	R_{13}	R_{23}
PC	1	0.6892	0.6892	0.9654	1	1
PETG	1	0.7567	0.7567	0.6862	1	1
TPU	1	0.5448	0.5448	0.82	1	1

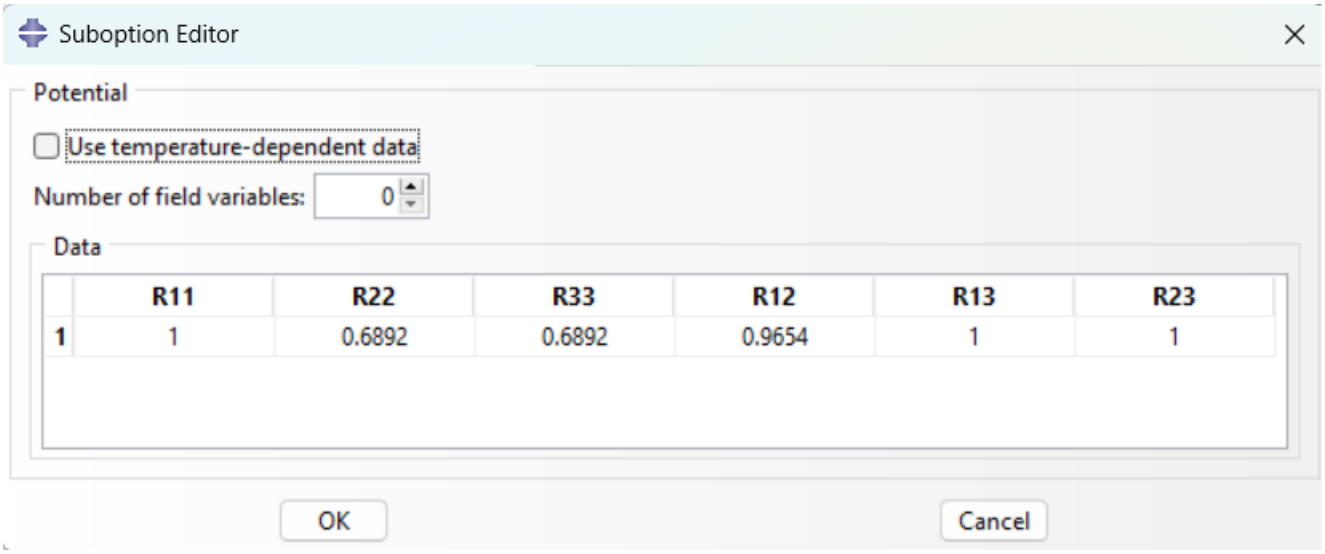

Figure 23: Hill's anisotropy coefficients input field in Abaqus.

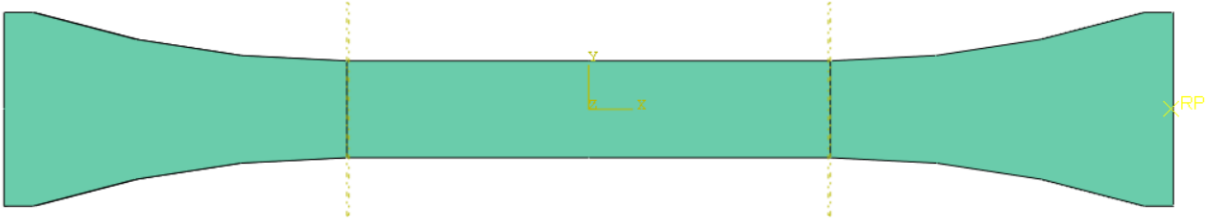

Figure 24: Tensile specimen defined in numerical model.

The elastic properties - Young's modulus, E and Poisson's coefficient, ν -, hardening curve, and anisotropy coefficients were defined for each material.

The boundary conditions were set by fixing one end of the specimen and applying an unidirectional displacement on the other. This displacement was defined based on the experimental tests, being that it should be greater than the maximum displacement recorded experimentally, for each each material. Only this way, the critical damage values could be obtained.

An approximate global mesh size of 2 mm and 8-node brick elements (C3D8R) were defined in all the performed simulations, with the exception of the TPU tensile test

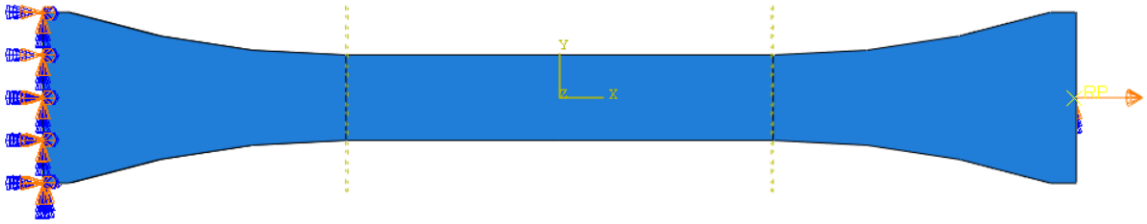

Figure 25: Representation of boundary conditions set for numerically simulating tensile test.

simulation, where a finer mesh size was defined along the length of the intermediate partition, due to the high elongation that the elements would be subjected to. The results obtained from the numerical simulations, as well as a comparison between those and the experimental data are detailed in Paper A.

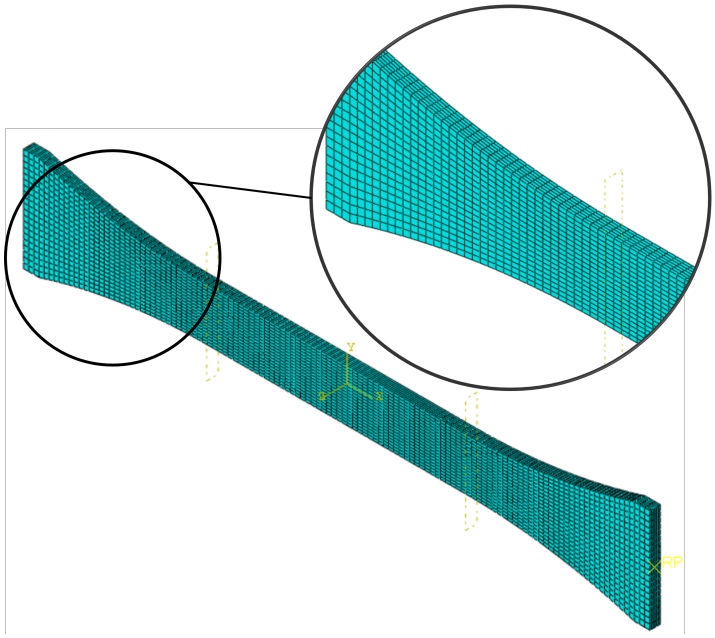

Figure 26: Defined mesh for numerical simulations of tensile tests.

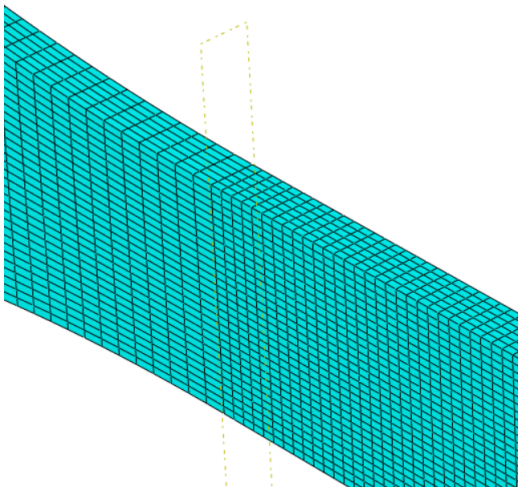

Figure 27: Mesh refinement of intermediate partition for numerical simulations of TPU tensile test.

4.4 Quasi-static compression tests

To validate the developed model, calibrated by the tensile tests, when applied to compression, the quasi-static compression tests of the reference EAS were numerically simulated.

The reference EAS 3D model, developed in SolidWorks software, was imported to Abaqus. The plates were defined as analytical rigid surfaces, to save computational time. A reference point, from which reaction force and displacement values were extracted, was defined in the plate.

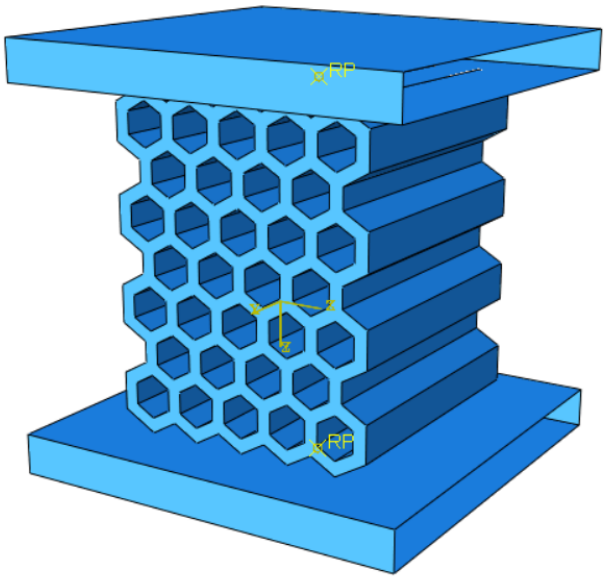

Figure 28: Reference EAS and compression plates Abaqus assembly.

Self-contact interaction was defined within the reference EAS. A surface-to-surface contact was defined between the structure and the plates. The friction coefficient, defined for each material, was iteratively determined. A high sensitivity of the deformation behaviour to the variation of that coefficient was observed.

The boundary conditions were set by fixing the bottom plate and imposing a displacement of 17 mm to the top plate in the descending direction. This displacement value was set, so the simulation would run past the displacement value for which there is total compaction of the structure (densification).

A global mesh size of 0.25 mm was defined in the core of the structure, and a more refined mesh size of 0.05 mm was defined on the contact surfaces, to improve contact behaviour between these (Figure 30). The numerically obtained load-displacement values and deformation behaviour of each structure are reported in Paper A.

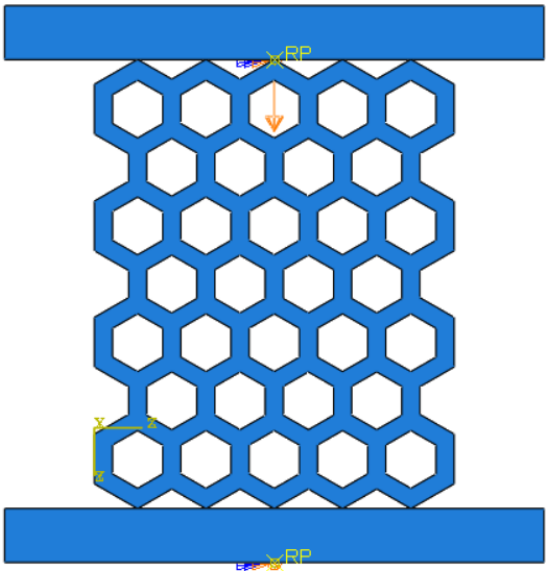

Figure 29: Representation of boundary conditions applied to compression test numerical simulations.

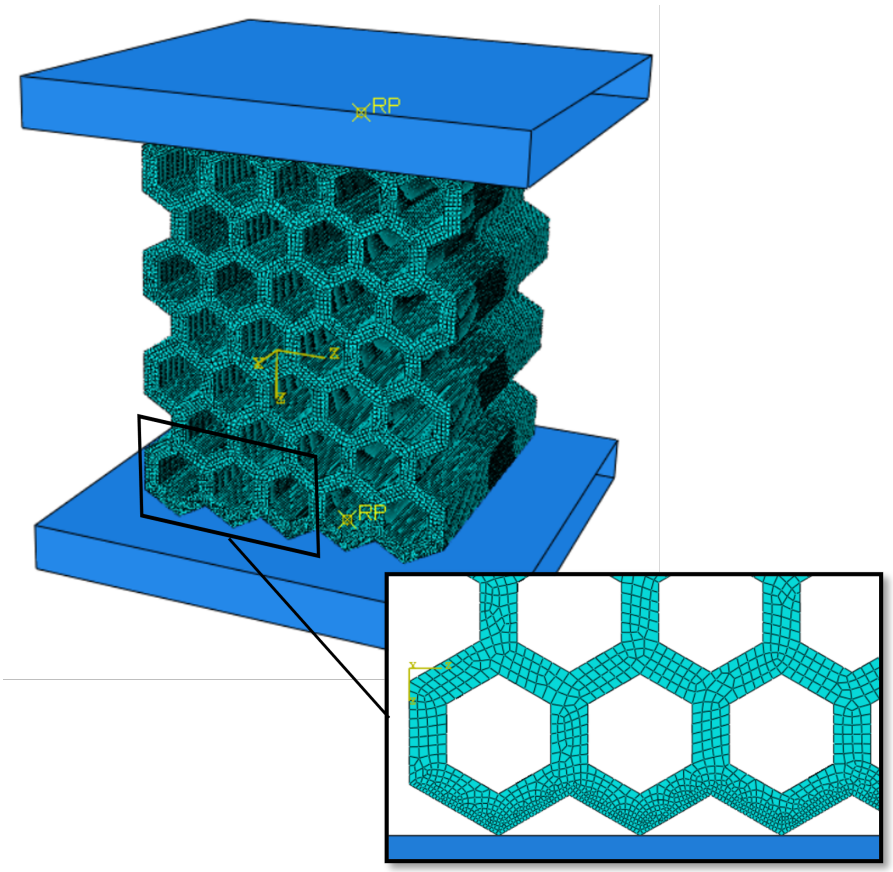

Figure 30: Defined mesh for numerical simulation of compression tests.

5 Results and discussion

5.1 Material characterization

A thorough material characterization was done by performing tensile tests. Properties such as ductility, stiffness and strength were assessed and it was possible to select the materials had the best properties to potentially integrate an energy absorption structure.

Figures 31-33 show a comparison of the measured properties for each material and raster orientation. Three materials stood out among the tested: PC, PETG and TPU. PC exhibited a favorable combination of stiffness and the highest strength relative to the other materials examined, while also demonstrating a satisfactory strain-to-failure ratio when printed with a 0°raster angle. Similarly, PETG displayed a moderate level of stiffness and strength, while being able to reach 200% strain to failure when printed with the same raster orientation. On the other, TPU's elasticity became evident, being able to elongate up to more than 400% its initial size. The load-displacement curves obtained for each material and printing orientation are exposed in Paper A.

The influence of the raster angle also became evident. A raster orientation parallel to the applied force (0°) provides the best mechanical properties, while the lowest properties are obtained for a 90°raster angle. The inability of the newly extruded filament to melt the adjacent ones leads to weak adhesion between layers and adjacent filaments while printing.

The suitability of these in a energy absorption structure would then be evaluated by developing two EAS: a single-material structure and multi-material one. The first would get its stiffness graded by changing the geometry along the extent of the structure, while the second would have an uniform geometry and integrate the three materials in a sequential order, according to their stiffness.

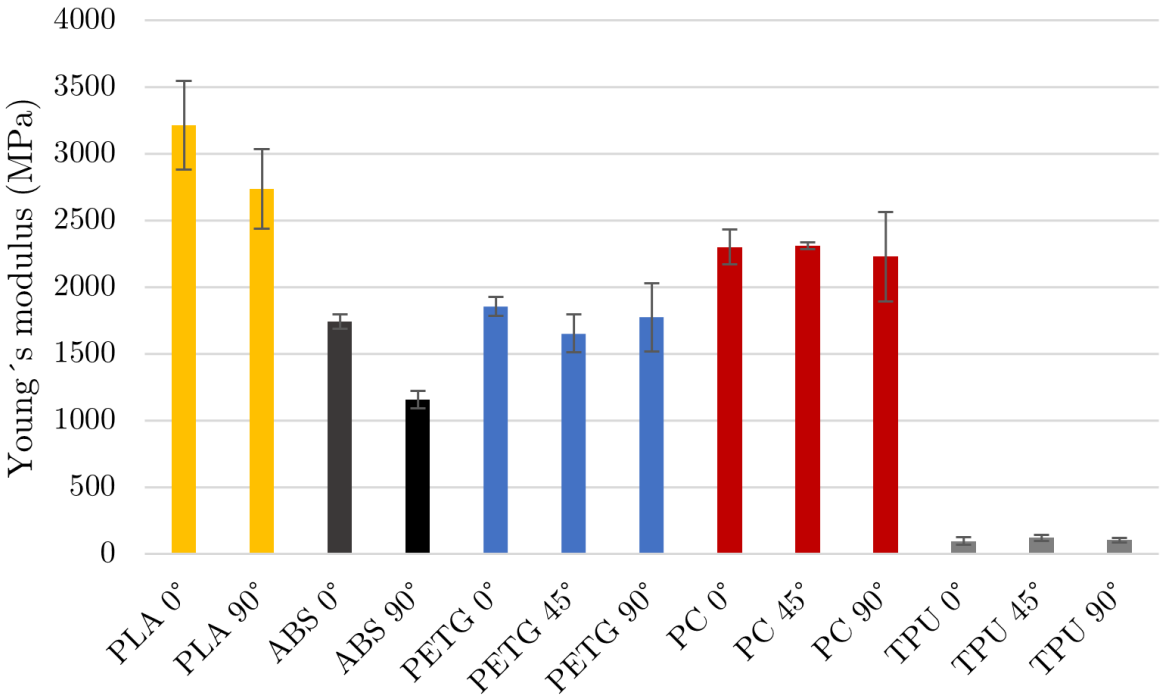

Figure 31: Materials' Young's modulus comparison.

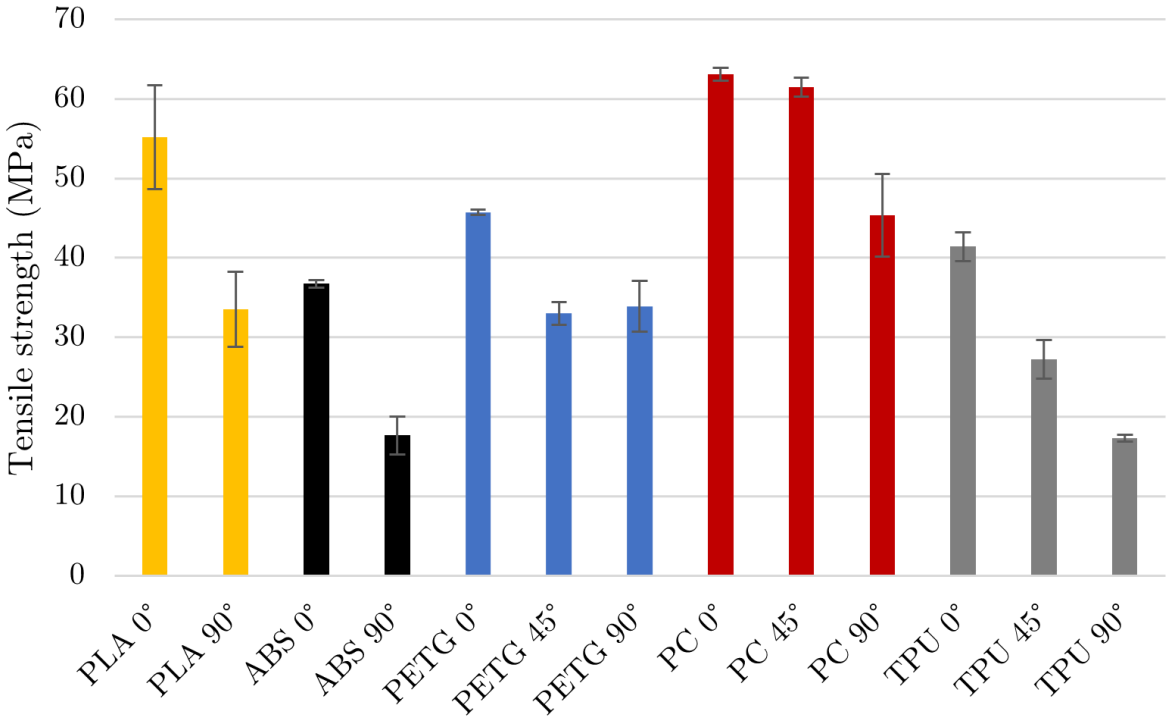

Figure 32: Materials' tensile strength comparison.

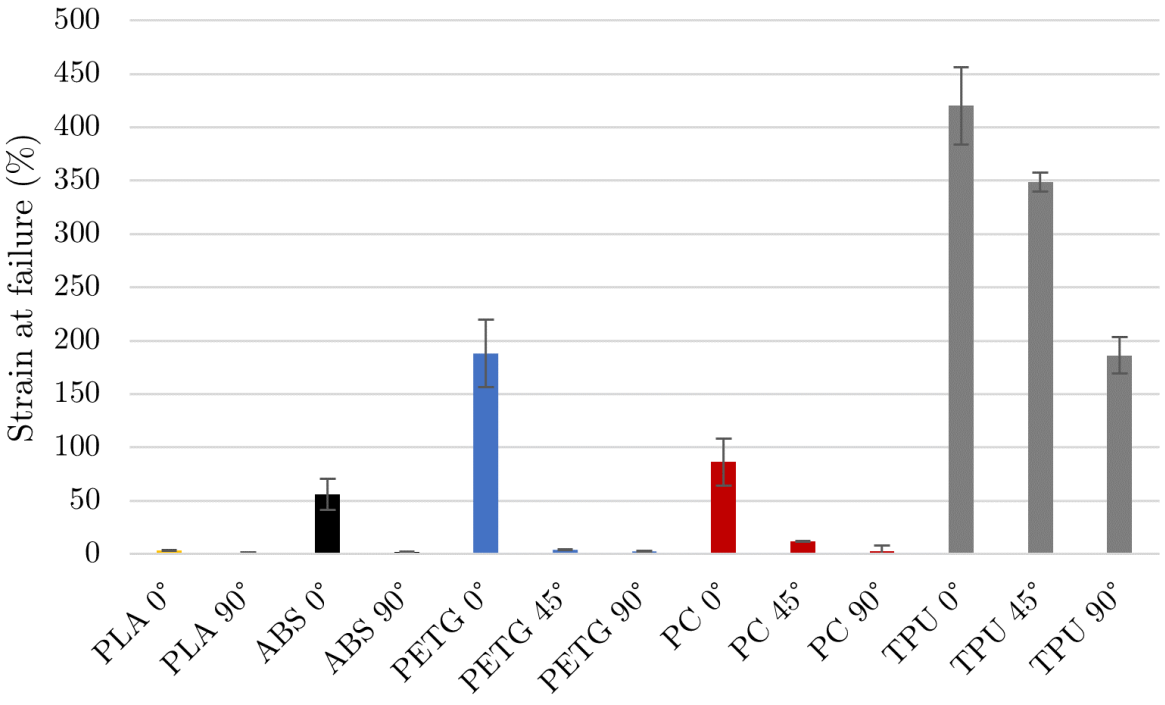

Figure 33: Materials' strain to failure comparison.

5.2 Reference EAS

Quasi-static compression tests were performed on PC, PETG and TPU honeycomb reference structures, printed in two different build orientations. Properties such as stiffness and energy absorption were evaluated (Figures 34 and 35).

The same trend of the tensile tests was observed. Ductile damage was observed in the PC and PETG structures where the layers were parallel to the loading direction (0°structures). On the other hand, when the layers where perpendicularly orientated to the loading direction (90°structures), a mixed failure with a great degree of brittle fracture was observed. This aspect made so that these structures had a more unpredictable failure mode and deformation behaviour. Moreover, for the same reduction in height, the 90°structures were not capable of absorbing the same amount of energy as the 0°ones. Regarding TPU, this brittle behaviour was not observed for the 90°structures. Nevertheless, the energy absorbed by these was slightly smaller, comparing to the 0°ones.

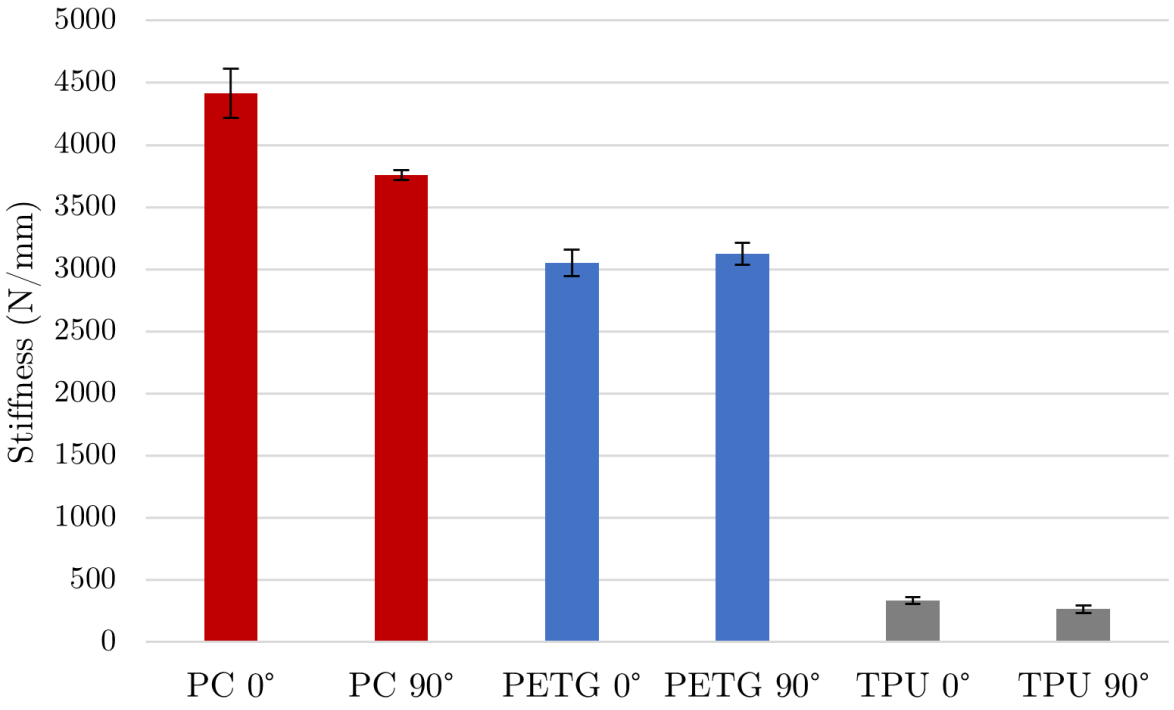

Figure 34: Comparison between the average stiffness, for each material and build orientation.

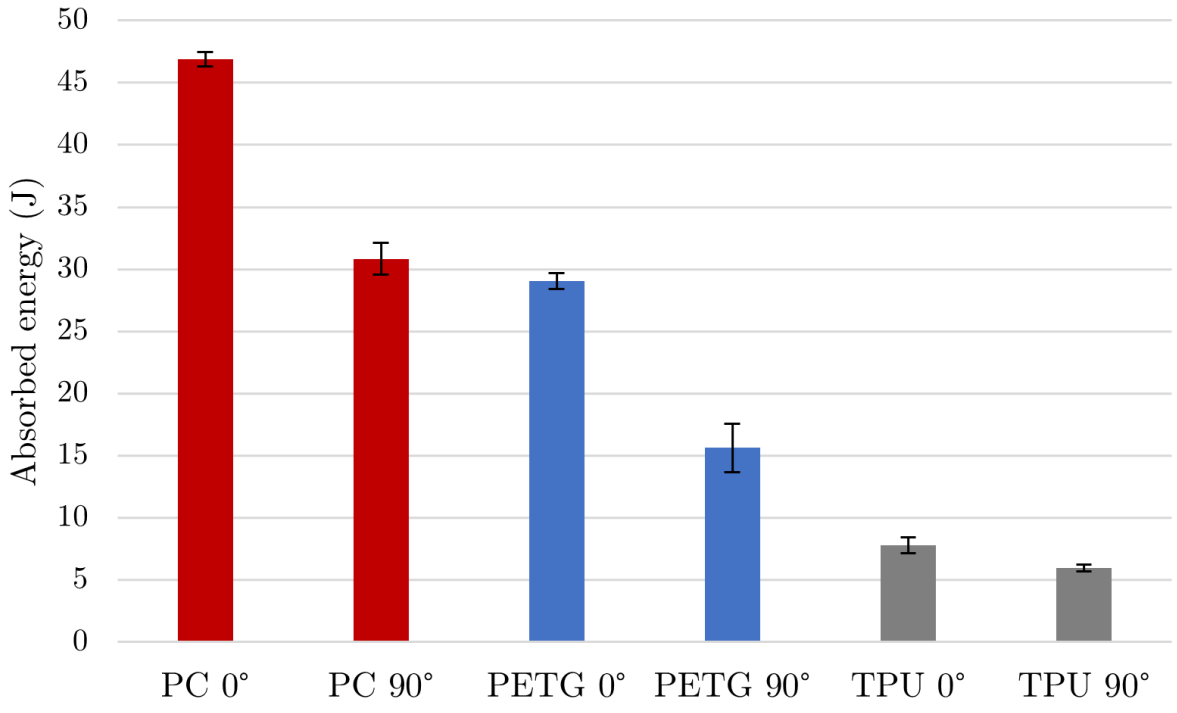

Figure 35: Comparison between the average absorbed energy values until a 10 mm reduction in height, for each material and build orientation.

5.3 Honeycomb multi-material EAS

Honeycomb multi-material structures were subjected to quasi-static compression, high-rate compression and impact. The effect of the multi-material grading was noticed on the collapse behaviour of the structures, where a clear staggered compression, with a sequential collapse was observed, as a results of the dissimilar stiffness values of the materials employed. Since the deformation of the intermediate and bottom parts of the structure only took place once the adjacent got full compacted, the overall densification of the EAS happened later when comparing to its uniform counterparts.

Moreover, four main parameters were calculated to assess the crashworthiness potential: PCF, MCF and CFE. The obtained values of these for the honeycomb structures are represented in Figure 37. It was noticed that the peak force measured during the compression of a structure only depends on the presence of the stiffer material, and not on its proportion.

The obtained load-displacement curves obtained and a more detailed description of the failure modes is presented in Paper B.

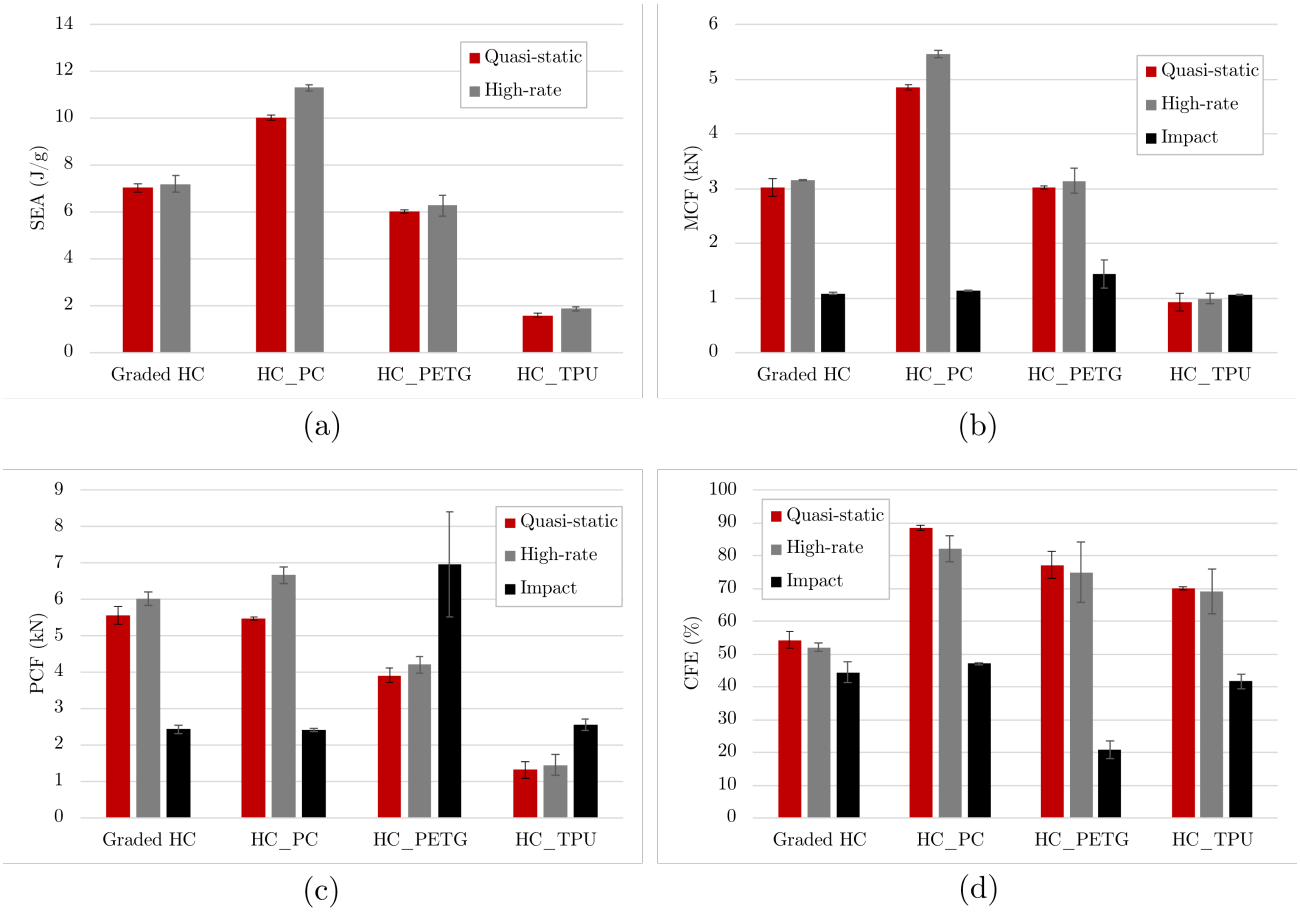

Figure 36: Crashworthiness indexes obtained for honeycomb multi-material structures, under different compression regimes.

Furthermore, the size effect on energy absorption capabilities was assessed by testing a larger multi-material honeycomb to compression under the same loading regimes. As expected, due to the longer compression stroke that it allowed, the energy absorbed by the large structure was higher than its smaller counterpart. Nevertheless, no influence of the size was noticed on the specific energy absorption and efficiency values. Hence, the prediction of energy absorption capability is possible through the testing of smaller counterparts.

Also, stability problems arose when testing the bigger size multi-material honeycomb. Its height facilitated buckling and consequent detachment of the adhesively bonded parts. Hence, the suitability of a bonded multi-material concept, such as the one presented, for integration in energy absorption applications becomes questionable.

5.4 Spider-web graded EAS

Likewise, specimens of the single-material spider web graded structures were printed in PC, PETG, and TPU, and subjected to quasi-static compression, high rate compression and impact. Collapse by folding was observed in the quasi-static tests along with interlayer crack formation and propagation, due to bending, for the PC and PETG structures. A high degree of brittle fracture was observed for PETG under high-rate and impact loading. Similar to the multi-material structure, a staggered compression was observed for the tested structure, with the sequential compression of increasingly stiffer stages of the structure. Crashworthiness parameters were calculated to assess energy absorption capabilities (see Figure 37). The obtained load-displacement curves obtained and a more detailed description of the failure modes is done in Paper B.

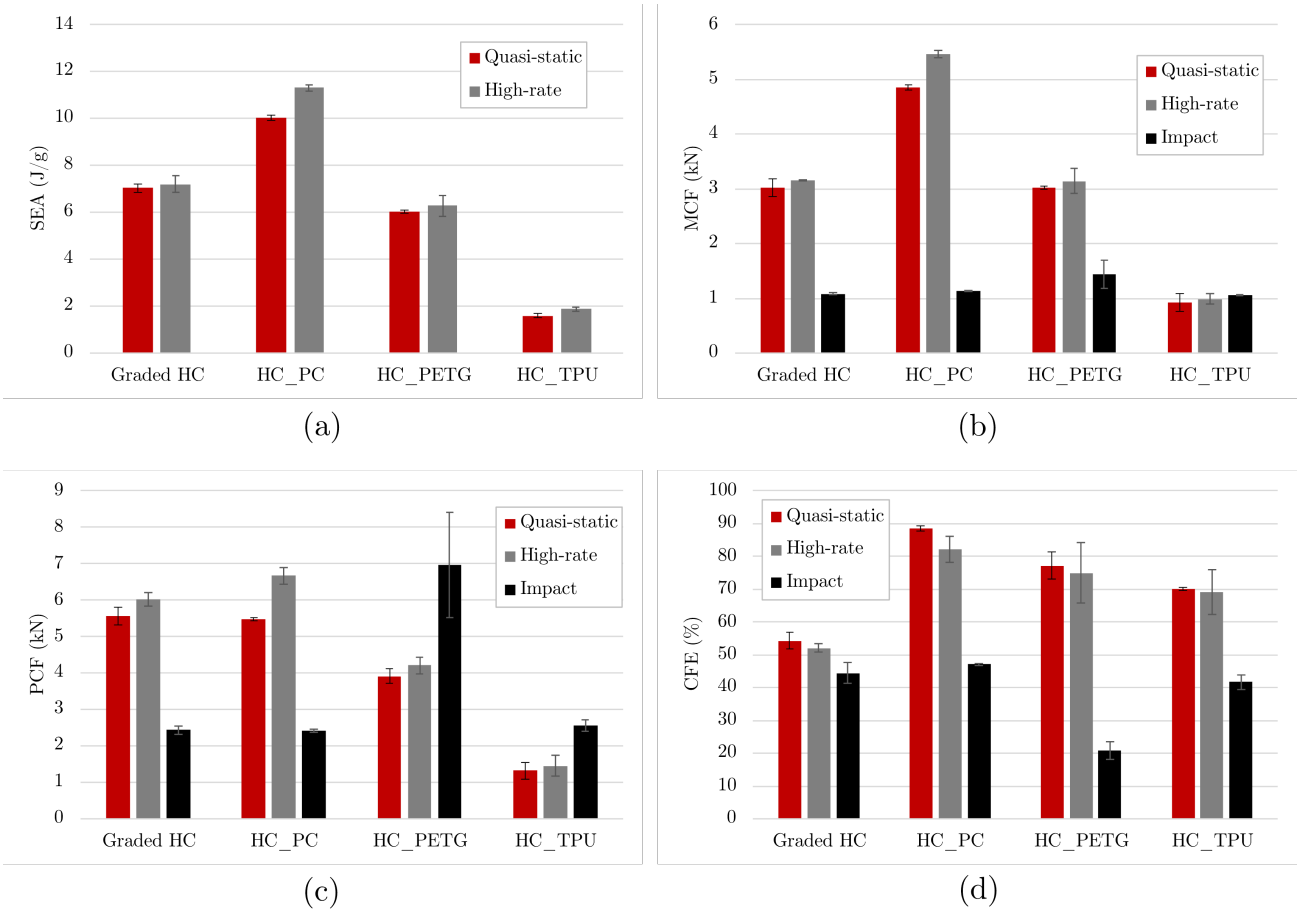

Figure 37: Crashworthiness indexes obtained for honeycomb multi-material structures, under different compression regimes.

6 Conclusions

This work aimed towards the development of a additively manufactured energy absorption structure for vehicle, more specifically, a crash box. A tensile characterization of diverse 3D printed thermoplastics was performed, from which three materials were selected to integrate the EAS, based on their superior properties. This characterization brought to light the severe anisotropic behaviour that FDM technology grants to the 3D printed parts. While the mechanical properties are favoured by a 0° raster angle, a significant deterioration of those is observed when the raster orientation is perpendicular to the applied force, due the weak adhesion between adjacent filaments.

Experimental compression tests were performed on a honeycomb reference structure, printed in two different build directions, where the 90° showed a brittle behaviour. Moreover, there was a higher proneness of these to the presence of printing defects.

A numerical model, calibrated by the tensile tests, was developed and applied to compression of the reference structure, for validation. While the anisotropy was modelled resorting to the Hill's yield model, multiple ductile damage criteria were employed in order to accuretaly simulate fracture: Brozzo, Normalized Cockroft-Latham and McClintock. The Normalized Cockroft-Latham criterion predicted more precisely the mixed tensile and shear fracture occurring during the compression of such structures. The developed model was able to predict accurately the deformation behaviour of the reference structures under compression.

Further development of two energy absorption structure concepts was put in place. A multi-material honeycomb structure and a single material spider web structure were deigned and printed, employing the selected materials: PC, PETG, and TPU. While the first got its grading from the variation of material properties, the second got it through the variation of the structural density.

These would be tested to compression under three different loading regimes to assess their crashworthiness: quasi-static compression, high-rate compression and impact.

The deformation behaviour and failure mechanisms of these structures was evaluated. A staggered collapse behaviour was observed, resulting in a staged compression with multiple crush plateaus, corresponding to each stiffness level. This behaviour was more evident for the multi-material structure. A collapse by folding of the spider web structures, under quasi-static loading was observed. For higher strain rates, PETG's brittleness was enhanced, leading to an accentuated brittle fracture mode of this material for high-rate compression and impact. Nevertheless, all three spider web graded structure showed to be efficient energy absorbers when submitted to impact.

The stiffness grading of the honeycomb structure led to a delay in the densification onset, when compared to uniform counterparts. However, the graded structure was unable to outperform the PC counterpart, regarding energy absorption capabilities. However, the

multi-material configuration can be an interesting concept to further explore, since the initial peak force resultant from an impact can be effectively reduced and the performance under close to real-world conditions, i.e. impact, can be enhanced.

Overall, the spider web structures revealed a higher potential for impact absorption when compared to the honeycomb counterparts. As a future project, a numerical analysis of a multi-material structure under impact can provide valuable insight for improvement of this concept, by exploring the ideal material properties for enhanced energy absorption performance. Furthermore, a topological analysis on the spider web graded structures can also be considered.

7 Summary of the appended papers

Paper A

Title: Mechanical characterization and numerical modelling of additively manufactured thermoplastics

Summary: The employment of additive manufacturing (AM) technologies has become an essential tool for the most varied industries. Among the available technologies, fused deposition modeling (FDM), also known as fused filament fabrication (FFF), has gained widespread adoption. However, owing to its layered construction, 3D printed components tend to exhibit anisotropic behavior, with the raster angle being a significant parameter contributing to this phenomenon. This study conducted o this paper aims to investigate the influence of the raster angle on the properties of 3D printed parts and evaluate the most promising materials for integrating a 3D printed energy absorption structure (EAS). Five materials, namely acrylonitrile butadiene styrene (ABS), polycarbonate (PC), polyethylene terephthalate glycol (PETG), polylactic acid (PLA), and thermoplastic polyurethane (TPU), are characterized through tensile tests to account for their distinct tensile behavior in various directions (0°, 45°, and 90°). Based on the results, a selection of the most promising materials for constructing an impact absorption structure. An open cell honeycomb structure is designed and 3D printed for each material and build orientation, followed by compression testing to assess crashworthiness parameters. Furthermore, a numerical analysis incorporating Hill's yield criterion for modeling anisotropy and a ductile damage model criterion for simulating failure are employed to predicted the deformation and collapse behavior of 3D printed open cell honeycomb structures subjected to in-plane compression.

Paper B

Title: Development and testing of additively manufactured bio-inspired structures for impact absorption

Summary: Having in mind the utmost necessity to increase road safety and promote sustainability, this research paper focuses on developing an optimized energy absorption structures (EAS) for vehicles. Inspired by bio-structures, such as honeycombs and spider webs, the study aims to create a multi-material and a single material, graded EAS using fused deposition modeling (FDM) technology. The materials chosen for this study are polycarbonate (PC), polyethylene terephthalate glycol (PETG), and thermoplastic polyurethane (TPU). The developed EAS designs are evaluated through the performance

of compression tests under different loading regimes to assess their energy absorption capabilities. The study also explores the impact of stiffness grading and size on the crashworthiness parameters. By comparing single and multi-material solutions, the paper seeks to provide valuable insights into the performance of the developed energy absorption structures.

References

[1] S M Kabir, Kavita Mathur, and Abdel-Fattah M. Seyam. A critical review on 3d printed continuous fiber-reinforced composites: History, mechanism, materials and properties. *Composite Structures*, 232:111476, 2020.

[2] I. John Solomon, P. Sevvel, and J. Gunasekaran. A review on the various processing parameters in fdm. *Materials Today: Proceedings*, 37:509–514, 2021.

[3] S. K. Selvamani, M. Samykano, S. R. Subramaniam, W. K. Ngui, K. Kadirgama, G. Kanagaraj, and M. S. Idris. 3d printing: Overview of abs evolvement. *AIP Conference Proceedings*, 2019.

[4] Sherri L. Messimer, Albert E. Patterson, Nasiha Muna, Akshay P. Deshpande, and Tais Rocha Pereira. Characterization and processing behavior of heated aluminum-polycarbonate composite build plates for the fdm additive manufacturing process. *Journal of Manufacturing and Materials Processing*, 2(1):12, 2018.

[5] Rebecca B. Dupaix and Mary C. Boyce. Finite strain behavior of poly(ethylene terephthalate) (pet) and poly(ethylene terephthalate)-glycol (petg). *Polymer*, 46(13):4827–4838, 2005.

[6] Eda Hazal Tümer and Husnu Yildirim Erbil. Extrusion-based 3d printing applications of pla composites: A review. *Coatings*, 11(4):390, 2021.

[7] Qi-Wei Lu and Christopher W. Macosko. Comparing the compatibility of various functionalized polypropylenes with thermoplastic polyurethane (tpu). *Polymer*, 45(6):1981–1991, 2004.

[8] Mohammadreza Lalegani Dezaki, Mohd Khairol Ariffin, Ahmad Serjouei, Ali Zolfagharian, Saghi Hatami, and Mahdi Bodaghi. Influence of infill patterns generated by cad and fdm 3d printer on surface roughness and tensile strength properties. *Applied Sciences*, 11(16):7272, 2021.

[9] Cesar Omar Balderrama-Armendariz, Eric MacDonald, David Espalin, David Cortes-Saenz, Ryan Wicker, and Aide Maldonado-Macias. Torsion analysis of the anisotropic behavior of fdm technology. *The International Journal of Advanced Manufacturing Technology*, 96(1-4):307–317, 2018.

[10] John Ryan Dizon, Alejandro H. Espera, Qiyi Chen, and Rigoberto C. Advincula. Mechanical characterization of 3d-printed polymers. *Additive Manufacturing*, 20:44–67, 2018.

[11] Sachini Wickramasinghe, Truong Do, and Phuong Tran. Fdm-based 3d printing of polymer and associated composite: A review on mechanical properties, defects and treatments. *Polymers*, 12(7):1529, 2020.

[12] J. Galante, G. M. F. Ramalho, M.Q. dos Reis, R. J. C. Carbas, E. A. S. Marques, and L. F. M. da Silva. *Mechanical Characterization of 3D Printed Specimens*, page 149–164. Springer, 2021.

[13] Manav Doshi, Ameya Mahale, Suraj Kumar Singh, and Samadhan Deshmukh. Printing parameters and materials affecting mechanical properties of fdm-3d printed parts: Perspective and prospects. *Materials Today: Proceedings*, 50:2269–2275, 2022.

[14] Patrich Ferretti, Christian Leon-Cardenas, Gian Maria Santi, Merve Sali, Elisa Ciotti, Leonardo Frizziero, Giampiero Donnici, and Alfredo Liverani. Relationship between fdm 3d printing parameters study: Parameter optimization for lower defects. *Polymers*, 13(13):2190, 2021.

[15] Vivek Kumar Tiwary, Arunkumar P., and Vinayak R. Malik. An overview on joining/welding as post-processing technique to circumvent the build volume limitation of an fdm-3d printer. *Rapid Prototyping Journal*, 27(4):808–821, 2021.

[16] Weijie Li, Lin Sang, Xigao Jian, and Jinyan Wang. Influence of sanding and plasma treatment on shear bond strength of 3d-printed pei, peek and peek/cf. *International Journal of Adhesion and Adhesives*, 100:102614, 2020.

[17] Yee Ling Yap, William Toh, Rahul Koneru, Rongming Lin, Keen Ian Chan, Huanyu Guang, Wai Yew Chan, Soo Soon Teong, Guoying Zheng, and Teng Yong Ng. Evaluation of structural epoxy and cyanoacrylate adhesives on jointed 3d printed polymeric materials. *International Journal of Adhesion and Adhesives*, 100:102602, 2020.

[18] José M. Arenas, Cristina Alía, Fernando Blaya, and Alfredo Sanz. Multi-criteria selection of structural adhesives to bond abs parts obtained by rapid prototyping. *International Journal of Adhesion and Adhesives*, 33:67–74, 2012.

[19] Mohammad Reza Khosravani, Payam Soltani, and Tamara Reinicke. Fracture and structural performance of adhesively bonded 3d-printed petg single lap joints under different printing parameters. *Theoretical and Applied Fracture Mechanics*, 116:103087, 2021.

[20] N.S.B. Yusof, S.M. Sapuan, M.T.H. Sultan, M. Jawaid, and M.A. Maleque. Design and materials development of automotive crash box: A review. *Ciência amp;amp; Tecnologia dos Materiais*, 29(3):129–144, 2017.

[21] N.A.Z. Abdullah, M.S.M. Sani, M.S. Salwani, and N.A. Husain. A review on crashworthiness studies of crash box structure. *Thin-Walled Structures*, 153:106795, 2020.

[22] Guohua Zhu, Guangyong Sun, Hang Yu, Shunfeng Li, and Qing Li. Energy absorption of metal, composite and metal/composite hybrid structures under oblique crushing loading. *International Journal of Mechanical Sciences*, 135:458–483, 2018.

[23] James Meredith, Richard Ebsworth, Stuart R. Coles, Benjamin M. Wood, and Kerry Kirwan. Natural fibre composite energy absorption structures. *Composites Science and Technology*, 72(2):211–217, 2012.

[24] Fatah Habib, Pio Iovenitti, Syed Masood, Mostafa Nikzad, and Dong Ruan. Design and evaluation of 3d printed polymeric cellular materials for dynamic energy absorption. *The International Journal of Advanced Manufacturing Technology*, 103(5–8):2347–2361, 2019.

[25] Oyindamola Rahman and Behrad Koohbor. Optimization of energy absorption performance of polymer honeycombs by density gradation. *Composites Part C: Open Access*, 3:100052, 2020.

[26] Simon R.G. Bates, Ian R. Farrow, and Richard S. Trask. Compressive behaviour of 3d printed thermoplastic polyurethane honeycombs with graded densities. *Materials amp; Design*, 162:130–142, 2019.

[27] Yuze Nian, Shui Wan, Mo Li, and Qiang Su. Crashworthiness design of self-similar graded honeycomb-filled composite circular structures. *Construction and Building Materials*, 233:117344, 2020.

[28] A. Praveen Kumar, M. Shunmugasundaram, S. Sivasankar, and L. Ponraj Sankar. Numerical analysis on the axial deformation and energy absorption behaviour of tri-tubular structures. *Materials Today: Proceedings*, 27:866–870, 2020.

[29] Abraham Segade, Alvaro J. Bolano, José A. López-Campos, Enrique Casarejos, J. R. Fernández, and J. A. Vilán. Study of a crash box design optimized for a uniform load profile. 2018.

[30] F. N. Habib, P. Iovenitti, S. H. Masood, and M. Nikzad. Cell geometry effect on in-plane energy absorption of periodic honeycomb structures. *The International Journal of Advanced Manufacturing Technology*, 94(5–8):2369–2380, 2017.

[31] Hafizur Rahman, Ebrahim Yarali, Ali Zolfagharian, Ahmad Serjouei, and Mahdi Bodaghi. Energy absorption and mechanical performance of functionally graded soft–hard lattice structures. *Materials*, 14(6):1366, 2021.

[32] Ngoc San Ha and Guoxing Lu. A review of recent research on bio-inspired structures and materials for energy absorption applications. *Composites Part B: Engineering*, 181:107496, 2020.

[33] Ibrahem Waleed, Ali Abdul Ruhaima, Zainab A Farhan, Nadia Salim Ismael, Muataz S Alhassan, Makram Skikara, Zeid Fadel Albahash, and Ahmed Najat Ahmed. Investigating energy absorption of thin-walled steel structures with combined mechanisms including inversion, foldingnbsp; and expansion. *Proceedings of the Institution of Mechanical Engineers, Part L: Journal of Materials: Design and Applications*, page 146442072311730, 2023.

A Paper A

Mechanical characterization and numerical modelling of additively manufactured thermoplastics

2 Institute of Science and Innovation in Mechanical and Industrial Engineering (INEGI), Porto, Portugal

Abstract: 3D printing, also known as additive manufacturing (AM), has become an essential tool for rapid prototyping and production of complex shape parts, in a wide variety of materials. Among all the existing technologies, fused deposition modelling (FDM), also known as fused filament fabrication (FFF), is the most widespread one. Due to its layer-by-layer nature, 3D printed parts tend to behave in an anisotropic way. To study the effect of the raster angle on printed parts, as well as evaluating the most promising materials for a 3D printed energy absorption structure (EAS), five materials were characterized: acrylonitrile butadiene styrene (ABS), polycarbonate (PC), polyethylene terephthalate glycol (PETG), polylactic acid (PLA) and thermoplastic polyurethane (TPU). To account for the different behaviour of these materials under tension, tensile tests were performed. For this purpose, bulk specimens of each material were produced in each main direction. As expected, the raster orientation played a major role on the properties obtained. PC, PETG and TPU emerged as the most promising materials for crashworthy applications. A novel numerical model for prediction of the deformation behaviour and fracture of 3D printed polymeric structures under tension and compression loads was developed. The Hill's yield criterion was employed to model anisotropy, whereas the Cockroft-Latham ductile damage model showed to be effective at predicting fracture. The collapse and failure mode of 3D printed cellular structures, under in-plane compression were accuretaly predicted, confirming the validity of the developed model when employed in the simulation of complex polymeric structures, with highly anisotropic properties.

Keywords: 3D printing, Raster orientation, Anisotropy, Ductile damage, Energy absorption structure, Finite element analysis

1 Introduction

Additive manufacturing (AM) technologies, commonly known as three-dimensional (3D) printing, first started being brought to light in 1980, around 40 years ago. The increase in research on this field led to a rapid evolution of the 3D printing technologies, being that in the last recent years there has been an exponential step forward with

the additive manufacturing market growing beyond projections [1]. When compared to traditional manufacturing processes, 3D printing technologies allow the production of components with a much higher degree of intricacy and with near net shape, substantially reducing material wastage. The dimensional accuracy can also be improved when resorting to additive manufacturing. However, those pose some challenges too. One of them is the fact that these require a high manufacturing lead time, not being suitable to high volume production [2]. Nevertheless, these are used in a wide variety of industries and applications ranging from robotics to medical purposes, such as prostheses production. These technologies have also been employed in research studies for the production intricate parts such as cellular and lattice structures [3–5].

There are many additive manufacturing technologies, such as fused deposition modelling (FDM), electron beam melting (EBM), selective laser sintering (SLS), multi jet fusion (MJF), and stereolithography (SLA). These differ from each other mainly on the printing mechanism and physical form of raw materials. Among the stated, FDM technology is the most widely implemented due to its process simplicity, cost-effectiveness, and high printing speed.

FDM printers use a thermoplastic filament that is heated to its melting temperature and extruded layer-by-layer to create a 3D structure. The mechanical properties and appearence of FDM printed parts are substantially affected by the definition of printing parameters, such as build orientation, raster angle, layer height, infill density, and temperatures of the nozzle and heat bed. The occurrence of defects such as high surface roughness, void content and warping can be minimized by correctly tuning those.

A lower layer thickness will reduce the staircase effect and, consequently, the surface roughness, as well as reduce the air gaps and void content. Furthermore, adequate temperatures of the heat bed and nozzle will also reduce the occurrence of internal stresses and consequent warping or layer separation, by maintaining a uniform temperature gradient [6].

Studies conducted on the influence of printing parameters on printed parts concluded that the tensile strength increases with the increase of infill density [2, 7, 8]. The infill pattern was also stated as influencing the mechanical properties [9] and surface quality of printed parts [2]. Moreover, the tensile strength is maximum when the raster orientation is parallel to the applied force (0° raster angle) [8]. This improvement in the obtained mechanical properties when the raster angle is 0° was also stated in a torsional analysis of ABS printed specimens [10]. The raster angle and build orientation were determined as being the most influential parameters in the mechanical properties of FDM 3D printed parts [11]. On the other hand, the tensile strength is also enhanced by increasing layer height [7]. However, a lower layer height can be an effective way of reducing the volume of printing defects [12].

Due to the significant increase in the adoption of 3D printing technologies in various

industries, it has become essential to accurately simulate and model additively manufactured parts. This allows for optimization and improvement of product designs, leading to the development of enhanced and more efficient products. In this regard, a numerical model for predicting FDM process-induced stresses and deflections has been developed in [13], and the influence of the infill pattern and density on those as been assessed. Good agreement between numerically simulated and experimental tensile tests was reached. Likewise, a phase-field fracture model was employed and an acceptable agreement between experimental and numerical results was achieved, when simulating 3D printed specimens, with unidirectional raster orientation, under tension [14]. Furthermore, a numerical model was developed capable of predicting the linear deformation phase of non-solid FDM 3D printed specimens under 4-point bending [15]. The elastic properties of a discretized gyroid pattern infill were also predicted by FEA [16].

The aim of this paper is to present a novel study on the numerical simulation of 3D printed honeycomb structures under compression, that serves as a validation for further simulation of additively manufactured energy absorption structures (EAS). There has been limited research conducted on the numerical simulation of complex 3D printed structures, capable of capturing the fracture and deformation behaviour of such. Therefore, the primary novelty of this study lies in addressing this research gap and contributing to the development of numerical tools for accurately simulating 3D printed parts under various types of solicitations.

In this regard, the characterization of the tensile mechanical properties of multiple 3D printed thermoplastics for further integration of those in an energy absorption structure (EAS) was done. The anisotropic behaviour of 3D printed specimens was modelled, resorting to the Hill´s yield model. A reference EAS was designed, printed, and tested to compression. The numerical model, calibrated by the tensile tests, was then applied to the simulation of the compression tests, used for validation purposes. A ductile damage criterion was employed to model fracture of the reference structure under compression loads.

2 Experimental procedures

2.1 Materials

In this study, five materials were tested: acrylonitrile butadiene styrene (ABS), polycarbonate (PC), polyethylene terephthalate glycol (PETG), polylactic acid (PLA), and thermoplastic polyurethane (TPU). These materials were selected based on their availability and potential to integrate an impact absorption structure.

ABS is widely used in FDM printed parts. Its dimensional stability and low glass transition temperature favour its processability by this technology. High impact resistance,

toughness, and moderate strength are some the mechanical properties that characterize this copolymer [17].

Along with ABS, PLA is one of the most used materials in FDM 3D printing as it can be easily thermally processed. Its low warping behaviour provides good dimensional accuracy to the printed parts, whereas the multicolour and furnished appearance make the parts visually attractive. Moreover, it has the advantage of being a sustainable material since it is biodegradable and recyclable. On the other hand, its poor mechanical properties, such as low strength, low toughness, and high brittleness, make this material not suitable for structurally demanding applications [18].

Polycarbonate (PC) is used in a wide variety of engineering applications. Its high strength and inertness provide resistance to harsh environments and make it suitable for optical, medical, electronic, and aeronautical purposes [19].

PETG is an amorphous copolymer of PET, that differs from the latter by having present an additional glycol group along the copolymerizing agent, PCT. While PET is used in many high-volume commercial and consumer applications, due to its ability to crystallize upon deformation at the subjected temperatures and strain rates during the processing, PETG does not have the ability to undergo strain induced crystallization. PETG presents good chemical resistance, durability and formability, as well as higher strength and impact resistance than PET. The low forming temperature that it requires makes it suitable for 3D printing and other heat-forming processes [20].

TPU is a thermoplastic elastomer. It combines the properties of vulcanized rubber with the processability of thermoplastic polymers. It is widely used due to its high tensile strength, abrasion and tear resistance, oil and solvent resistance, low-temperature flexibility, and paintability [21].

Table 1 shows the main mechanical properties and recommended printing temperatures for each material, according to the supplier.

Table 1: Main mechanical properties and printing temperatures (obtained from supplier's data sheet) [22–24].

	Filament PM ABS-T	Prusament PC Blend	Prusament PETG	Prusament PLA	Fillamentum Flexfill TPU 98A
Young's modulus (GPa)	-	1.9 ± 0.1	1.5 ± 0.1	2.3 ± 0.1	-
Yielding stress (MPa)	-	63 ± 1	47 ± 2	59 ± 2	-
Tensile stress at break (MPa)	-	-	-	-	53.7
Elongation at yield (%)	-	5.8 ± 0.3	5.1 ± 0.1	3.2 ± 1.0	-
Elongation at break (%)	-	-	-	-	318
Nozzle temperature (°)	230-250	275 ± 10	250 ± 10	210 ± 10	220-240
Build plate temperature (°)	100-110	110 ± 10	80 ± 10	40-60	50-60

2.2 Geometry

Regarding the characterization of the candidate materials, the tensile tests were conducted with specimens shaped according to BS 2782 standard, as Figure 1.

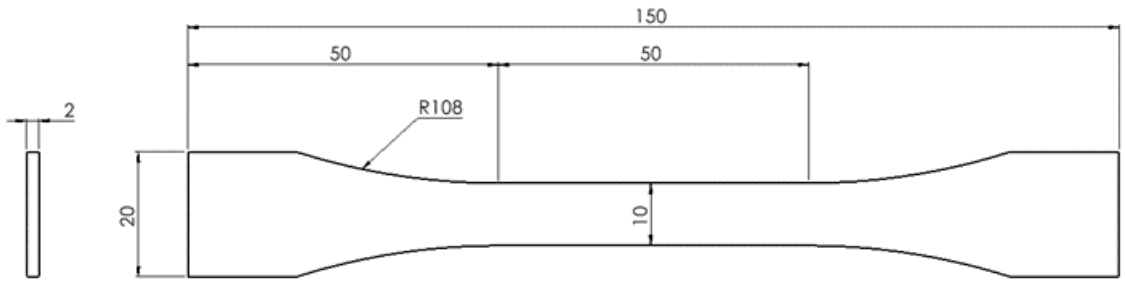

Figure 1: BS 2782 standard tensile specimen geometry (dimensions im mm).

Furthermore, a small-sized reference EAS with a honeycomb cellular geometry was

modelled and printed (Figure 2). The honeycomb structure consists of hexagonal cells that are interconnected, forming a pattern similar to that of a beehive. These cells create a lightweight and rigid structure, offering excellent strength and stiffness. Due to the high strength-to-weight ratio, honeycomb structures are used in multiple industries, such as aerospace, automotive, or construction.

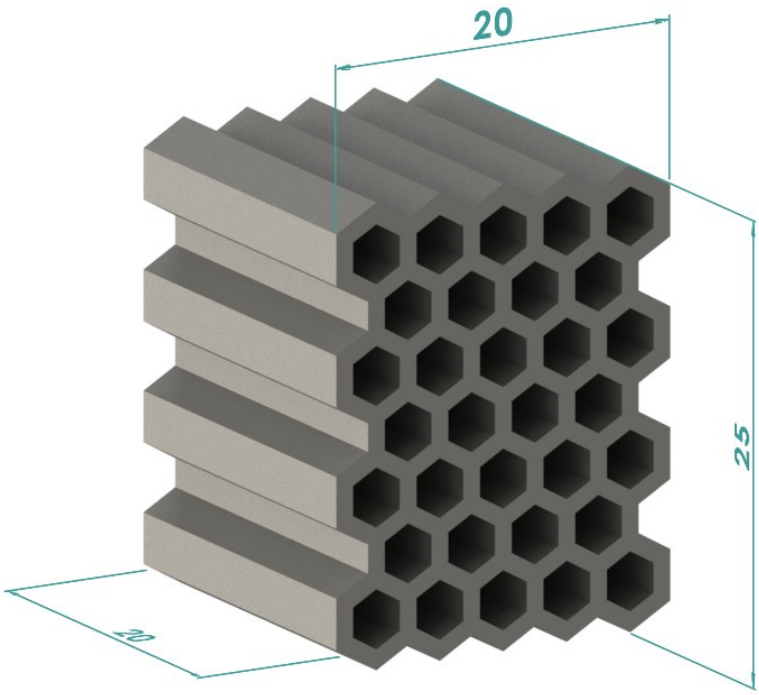

Figure 2: Dimensions of reference EAS (dimensions in mm).

2.3 3D printing

The equipment used to print the specimens was the Original Prusa i3 MK3S+. This 3D printer model uses FDM technology to create three-dimensional parts. It has a build volume of 250x210x210 [mm], being able to print small to medium parts. When it comes to printing capabilities, the minimum and maximum layer heights are 0.05 mm and 0.35 mm, respectively, and has a maximum travel speed of 200 mm/s. The printer nozzle and heat bed can reach up to 300 °C and 120 °C, respectively.

The raster angle has a major influence on the mechanical properties of printed parts, as the best tensile properties are obtained when a part is printed in a parallel orientation to the applied force [**?**,10,25]. During the material deposition, the newly extruded filament is not able to completely melt the adjacent layers, causing weak interlayer bonding. Hence, the interlayer regions act as discontinuities that promote the premature failure of a part when loaded perpendicularly to the printing direction [26].

In this study, the anisotropy phenomenon of FDM printed parts was a topic of interest. To determine the influence of raster angle on the mechanical properties, tensile tests were performed on unidirectional specimens printed in the three main directions, measured in relation to the orientation of the applied force - 0°, 45° and 90°. The anisotropic behaviour was then modelled, recurring to the Hill yield model.

Hence, at least 3 tensile specimens were produced for each material and raster orientation - 0°, 45° and 90° (see Figure 3). The specimens were printed with a 100% aligned rectilinear infill. Since the influence of the raster angle on the mechanical properties was a key point of this study, these were printed without any horizontal top or bottom shells, and with the vertical shell reduced to one perimeter, in order to minimize the effect of features other than the unidirectional infill on the tensile properties of the parts. All the specimens were printed with the same build orientation - flat on the print bed.

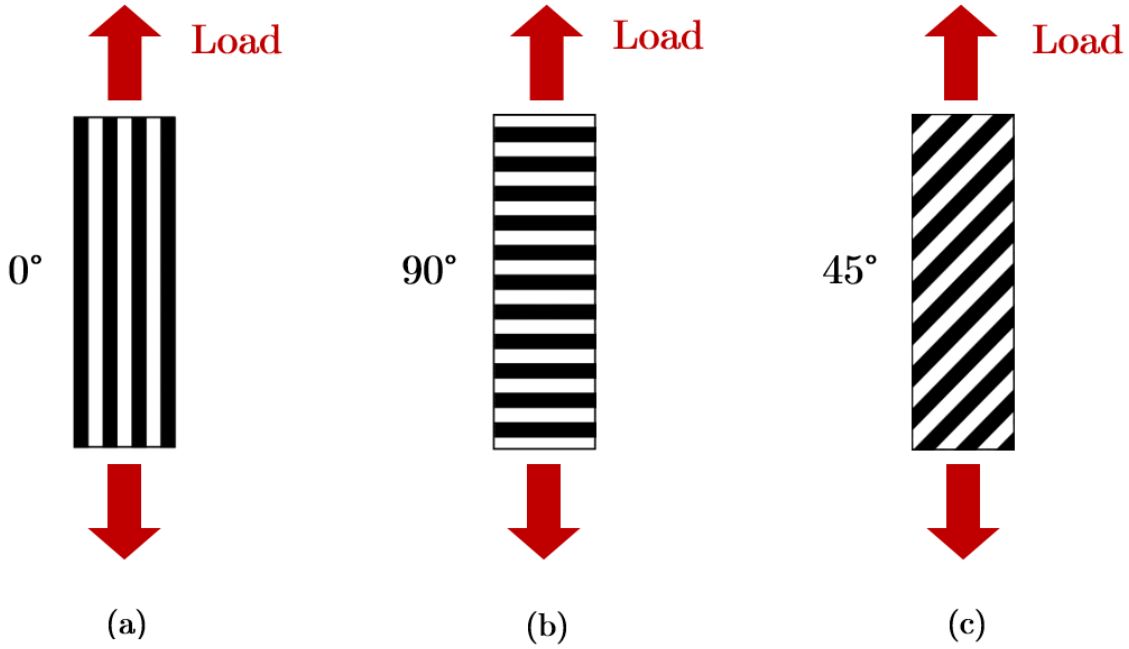

Figure 3: (a) Representative configuration of 0° specimen; (b) Representative configuration of 90° specimen; (c) Representative configuration of 45° specimen.

In order to obtain high quality specimens, the parts for testing were printed at a reduced speed and with a layer height of 0.05 mm, with exception of the first layer that had a height of 0.2 mm to grant improved adhesion and tolerance, by mitigating possible slight errors in leveling. The slicer software used to generate the G-code files for printing was PrusaSlicer. The printing temperatures for each material were set according to the default temperatures defined by PrusaSlicer software, being that the nozzle temperatures were increased by 5 °C for each material, to allow a good adhesion between the layers and adjacent filaments, and enhance the properties of the printed specimens. The printing temperatures are shown in Table 2.

After characterizing the before mentioned materials under tensile load, three of them were selected as candidates to integrate an energy absorption structure: PETG, PC and TPU. The choice was made based on the materials that offered the most promising mechanical properties to be apart of such structure, among the five tested. Hence, only those were employed when printing the reference EAS.

For each selected material, the reference EAS specimens were printed for two distinct build orientations, as Figure 4 shows. The different build orientations made so that one of the structures would have its layers aligned perpendicularly to the applied load (90° reference EAS) and the other would have its layers parallel to it (0° reference EAS) when compressed. The specimens were printed with a initial layer height of 0.2 mm and a height of 0.05 mm for subsequent layers. A 100% density aligned rectilinear infill was employed.

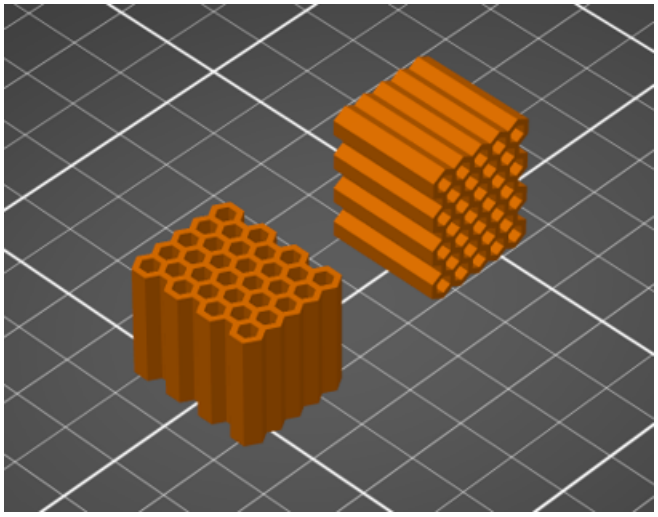

Figure 4: Position of 0° reference EAS (left) and 90° reference EAS (right) on the print bed.

Table 2: Temperatures set for printing of the specimens.

Material	Printing temperature (°C)	
	Print bed	Nozzle
ABS	110	260
PC	115	280
PETG	90	255
PLA	60	220
TPU	50	245

2.4 Material and reference EAS testing

In order to obtain the mechanical properties of the polymers under tension, quasi-static tensile tests were conducted on a Instron 3367 universal testing machine, equipped with a 30 kN load cell, at a constant cross-head displacement rate of 1 mm/min until failure. A high precision extensometer was attached to the specimens prior to the start of the tensile tests, to measure the strain during the latter. Since the extensometer could only measure strains up to 100%, the strain to failure of specimens that surpassed that value was indirectly estimated by dividing the gauge length by the cross-head displacement at failure. At least three specimens were tested, for each material/raster orientation configuration.

Moreover, quasi-static compression tests were performed on the printed reference structures, at a cross-head displacement rate of 1 mm/min, until past the point of densification. An Instron 3367 universal testing machine was used to perform the compression tests.

At least three tests were performed for each structure's material/build orientation configuration and the average absorbed energy until a 10 mm height reduction (d = 10 mm) and stiffness were calculated. All tests were performed at room temperature (23 °C).

3 Material modelling

3.1 Anisotropy

As already mentioned, FDM consists of a layer-by-layer process that grants anisotropic properties to the produced parts. In this study, the raster angle is considered as the main factor contributing to the anisotropic behaviour of the printed parts and, hence, affecting the mechanical properties. The coordinate systems 123 and xyz were implemented as the material and loading reference systems, respectively. Figure 5 shows the material and load orientations of a single layer.

During the deformation process, materials undergo a linear elastic deformation stage, before yielding and entering the plastic deformation stage, where they irreversibly elongate until fracture. The yielding point depends on the material and raster angle. Hence, Hill's criterion was used to model the anisotropic yield of each material. In [27], material anisotropy was successfully modelled by implementing this criterion on an elastoplastic model, obtaining a good agreement between experimental and numerical results. Likewise, a satisfactory agreement between theoretical and experimental results was obtained in the study conducted in [28] when predicting the anisotropic ultimate tensile strength of FDM printed parts resourcing to the Tsai-Hill criterion. The yield criterion proposed by Hill, in 1948, states the following:

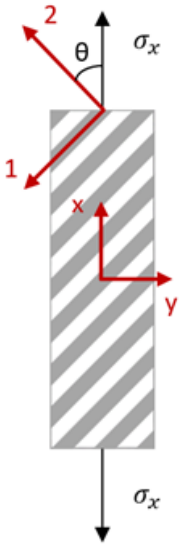

Figure 5: Representation of principal directions and raster angle.

$$\begin{aligned}(G+H){\sigma_1}^2 \ + \ (F+H){\sigma_2}^2 \ + \ (F+G){\sigma_3}^2 \ - \ 2H\sigma_1\sigma_2 \ - \ 2G\sigma_1\sigma_3 \\ -F\sigma_{23} \ + \ 2L{\tau_{23}}^2 \ + \ 2M{\tau_{31}}^2 \ + \ 2N{\tau_{12}}^2 \ = 1\end{aligned} \tag{1}$$

Where parameters F, G, H, L, M and N depend on the state of anisotropy. Let X, Y, Z be the ultimate tensile strength in the main three directions, respectively. Then, the following equations can be obtained:

$$\begin{aligned}\frac{1}{X^2} &= G+H, \quad & 2F &= \frac{1}{Y^2}+\frac{1}{Z^2}-\frac{1}{X^2} \\ \frac{1}{Y^2} &= H+F, \quad & 2G &= \frac{1}{Z^2}+\frac{1}{X^2}-\frac{1}{Y^2} \\ \frac{1}{Z^2} &= F+G, \quad & 2H &= \frac{1}{X^2}+\frac{1}{Y^2}+\frac{1}{Z^2}\end{aligned} \tag{2}$$

Furthermore, if U, V, W are the ultimate bearing strength in shear, regarding the principal anisotropy axes, the following equations can be written:

$$2L = \frac{1}{U^2}, \quad 2M = \frac{1}{V^2}, \quad 2N = \frac{1}{W^2} \tag{3}$$

By considering an isotropic transverse plane on the 3D printed specimens (plane 23), and a plane stress state ($\sigma_3 = \tau_{13} = \tau_{23} = 0$), the following equations can be obtained:

$$Y = Z \Rightarrow H = G = \frac{1}{2X^2}, \qquad F + H = \frac{1}{Y^2} \tag{4}$$

For an orthotropic, transversely isotropic materials under plane stress, the Tsai-Hill criterion can be written as follows:

$$\frac{\sigma_1^2}{X^2} + \frac{\sigma_2^2}{Y^2} - \frac{\sigma_1 \sigma_2}{Y^2} + \frac{\tau_{12}^2}{W^2} = 1 \tag{5}$$

The stress components in the material's reference system can be determined in the uniaxial tensile test, where $\sigma_{\mathrm{x}} \neq 0$, $\sigma_{\mathrm{y}} = \tau_{\mathrm{xy}} = 0$, by utilizing the following equation:

$$\begin{aligned} \sigma_1 &= \sigma_{\mathrm{x}}\ sin^2\theta \\ \sigma_2 &= \sigma_{\mathrm{x}}\ cos^2\theta \\ \tau_{12} &= -\sigma_{\mathrm{x}}\ sin\theta\ cos\theta \end{aligned} \tag{6}$$

By inserting Eq. 6 into Eq. 5 and solving for σ_{x}, we can derive the following expression:

$$\sigma_\theta = \sigma_{\mathrm{x}} = \left[\frac{sin^4\theta}{X^2} + \frac{cos^4\theta}{Y^2} + \left(\frac{1}{W^2} - \frac{1}{Y^2} \right) sin^2\theta\ cos^2\theta \right]^{-\frac{1}{2}} \tag{7}$$

Where σ_θ denotes the ultimate tensile strength in any given load direction, and X and Y represent the ultimate tensile strengths of the printed materials in the 0°and 90°directions, respectively. W can be determined by obtaining the ultimate tensile strength of the printed materials in the 45°direction and applying Eq. 7.

3.2 Ductile damage

Due to their straightforward formulation and calibration method, uncoupled fracture criteria have found extensive use in metal forming processes. The formulation of the damage accumulation function in these criteria is based on macroscopic variables. The general form of these criteria is represented as follows:

$$D = \int_0^{\bar{\varepsilon}_{\mathrm{p}}} f(macroscopic\ variables) d\bar{\varepsilon}_{\mathrm{p}} \tag{8}$$

Here, f represents the weighting function, D denotes the damage indicator, $\bar{\varepsilon}_{\mathrm{p}}$ and signifies the equivalent plastic strain. Empirical observations have led to the development of different weighting functions by incorporating various macroscopic variables such as principal stress components, stress triaxiality, and the Lode angle parameter. The fracture criteria presented in Eq.8 is commonly referred to as the phenomenological fracture model in the literature. In this study, three ductile fracture criteria with distinct weighting functions were examined. These include the Normalized Cockroft-Latham, Brozzo, and McClintock criteria, as outlined in Table 3, and correspond to the hydrostatic stress, σ_{m}, the equivalent stress, $\bar{\sigma}$, the maximum principal stress, $\sigma_{\max}$, the stress triaxiality, η, and the normalized Lode angle parameter $\bar{\theta}$, respectively. The critical damage parameter, D, for each criterion needs to be determined through an appropriate calibration procedure. In this study, a hybrid experimental-numerical method is utilized, where these criteria are incorporated into the finite element simulations of the tests conducted on the printed materials. This approach allows for the determination of the critical damage value at the displacement where failure initiates in the experimental tests. The calibrated criteria would subsequently be employed to simulate failure in the compression tests conducted on the reference structure. To identify the most suitable ductile damage criterion that accurately describes the deformation process of these structures under compression loads, a comparison is made between the numerical and experimental results of the compression tests.

Table 3: Candidate ductile damage criteria.

Ductile damage criteria	Damage accumulation funtion
Normalized Cockroft-Latham	$\mathrm{D}_1 = \int_0^{\bar{\varepsilon}_p} \left(\frac{\sigma_{max}}{\bar{\sigma}}\right) d\bar{\varepsilon}_p = \int_0^{\bar{\varepsilon}_p} \left(\eta + \frac{2}{3}\ \cos\left(\frac{\pi}{6}\left(1-\bar{\theta}\right)\right)\right) d\bar{\varepsilon}_p$
Brozzo	$\mathrm{D}_2 = \int_0^{\bar{\varepsilon}_p} \frac{2\sigma_{max}}{3(\sigma_{max}-\sigma_m)} d\bar{\varepsilon}_p = \int_0^{\bar{\varepsilon}_p} \frac{\eta+\frac{2}{3}\ \cos\left(\frac{\pi}{6}\left(1-\bar{\theta}\right)\right)}{\cos\left(\frac{\pi}{6}\left(1-\bar{\theta}\right)\right)} d\bar{\varepsilon}_p$
McClintock	$\mathrm{D}_3 = \int_0^{\bar{\varepsilon}_p} \frac{\sigma_m}{\bar{\sigma}} d\bar{\varepsilon}_p = \int_0^{\bar{\varepsilon}_p} \eta d\bar{\varepsilon}_p$

4 Finite element modelling

The development of a numerical model capable of predicting the behaviour of 3D printed structures under compression was an objective of the present study. Thus, in

order to calibrate the materials' hardening curves and validate the anisotropic yield criterion, a finite element analysis was conducted on Abaqus/Explicit software. This analysis consisted of simulating tensile tests for each raster orientation and material. The validated material models would then be employed in a FE model developed for simulating the reference EAS compression tests.

As mentioned before, Hill's yield model was employed to model the anisotropic behaviour of the printed parts. To implement Hill's criterion on Abaqus, six anisotropy coefficients (R_{11}, R_{22}, R_{33}, R_{12}, R_{13}, R_{23}) needed to be obtained. Since a plane stress state was assumed, $R_{13} = R_{23} = 1$. The remaining coefficients can be calculated by the following expressions:

$$\frac{1}{R_{11}^2} = (G+H)\,\sigma_0^2, \qquad \frac{1}{R_{22}^2} = (H+F)\,\sigma_0^2, \qquad \frac{1}{R_{33}^2} = (F+G)\,\sigma_0^2, \qquad \frac{3}{2R_{12}^2} = N\sigma_0^2 \tag{9}$$

Where σ_0 is the ultimate tensile strength of 0° printed specimens, for each material.

4.1 Tensile tests

The tensile specimens were described as 3D solid elements C3D8R with an approximate global mesh size of 2 mm and six elements through thickness were considered (see Figure 6). As boundary conditions, one end of the specimen was fixed while a displacement was applied to the other. The displacement applied depended on the maximum elongation obtained experimentally for each material. A dynamic explicit solver, along with a time scaling method, was employed to decrease the computational time. It is worth mentioning that the ratio between the kinetic and internal energy was negligible. The user subroutine VUSDFLD was utilized to define ductile damage criteria, enabling the calculation of damage evolution throughout the tests.

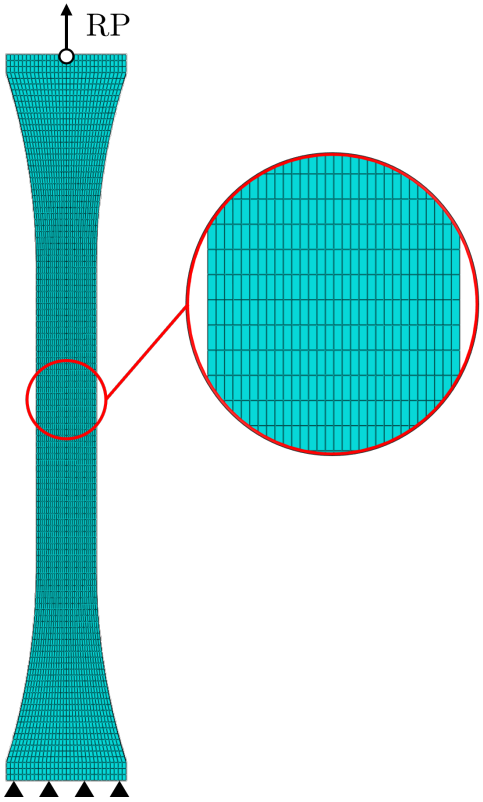

Figure 6: Mesh details and boundary conditions of FE model used for calibration.

4.2 Compression tests

The reference structure was defined as 3D solid elements C3D8R with an overall approximate global mesh size of 0.25 mm. A more refined mesh of 0.1 mm was implemented on the contact areas of the structure with the plates to accurately model contact between the parts, as shown in Figure 7. The plates were defined as analytical rigid surfaces to decrease computational time. The bottom plate was fixed, while a descending displacement was applied to the top plate.The displacement was set to 17 mm in order to ensure that the simulations would continue beyond the densification point of the structures. A surface-to-surface contact was established between the structure and the plates, taking into account the penalty friction formulation. A dynamic explicit solver was utilized, and it was observed that the ratio between kinetic and internal energy remained insignificant throughout the simulation. The ductile damage criteria were employed to simulate the failure behavior of the structures, utilizing the defined user subroutine VUSDFLD. In order to model crack initiation and propagation, element deletion was activated when the damage function reached its critical value in a specific element.

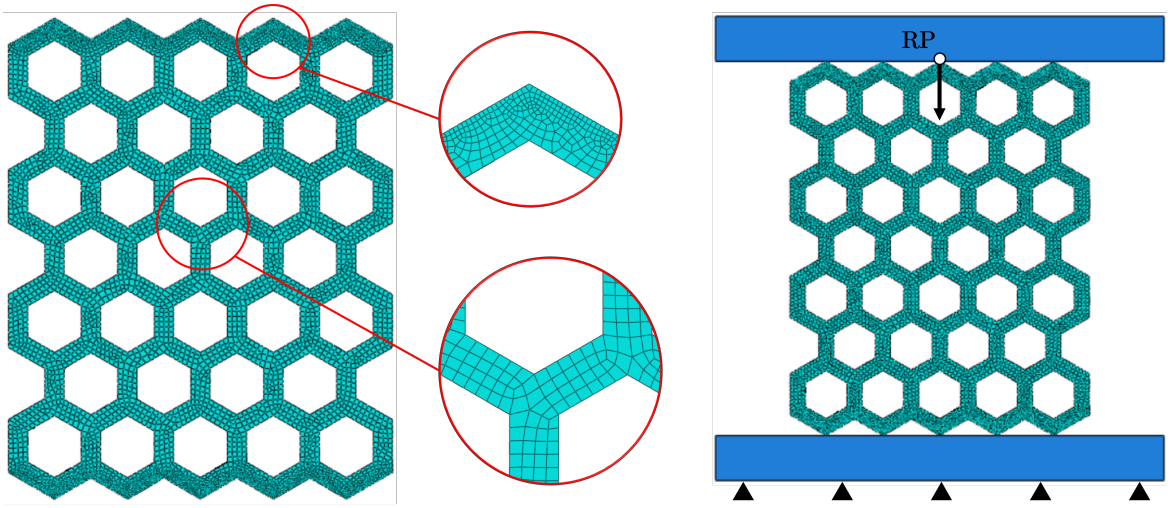

Figure 7: Mesh details (a) and boundary conditions (b) of FE model used to simulate compression tests of the reference EAS.

5 Results and discussion

5.1 Mechanical properties

In this section, the experimental results of the tensile tests conducted on each material will be presented and discussed. For ABS and PLA only 0° and 90° specimens were tested, while for the remaining materials specimens were printed and tested in the three main directions – 0°, 45° and 90°. The first two materials were disregarded for further characterization, since those were considered the ones with less potential to integrate a energy absorption structure. It should be noted that the reported mechanical properties were calculated as the average of three valid tensile tests.

5.1.1 PLA

PLA was found to be the material with the highest stiffness, with a maximum measured Young's modulus of 3558 MPa, for a 0° raster angle. On the other hand, its brittleness became evident, with a very low strain to failure for both 0° and 90° specimens. The measured mechanical properties are shown in Table 4.

While for the 90° specimen there was crack propagation through the adjacent filaments interface, resulting from poor adhesion, a transverse rupture of the filaments can be observed in the 0° specimen (see Figure 9). Figure 8 shows the obtained stress-strain curves.

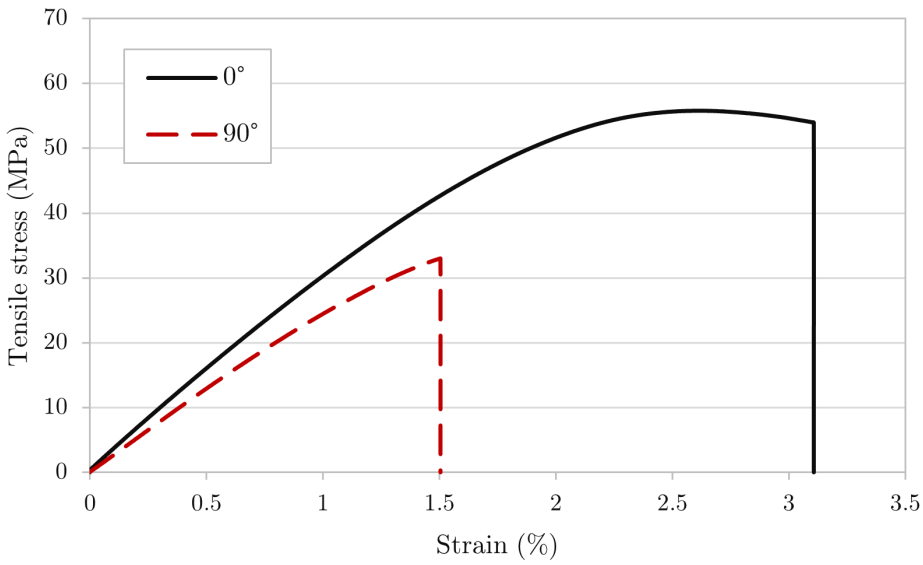

Figure 8: PLA experimental tensile stress vs strain curves.

Table 4: Experimentally obtained mechanical properties of PLA specimens.

	Young's modulus (MPa)	Tensile strength (MPa)	Strain to failure (%)
PLA 0°	3214 ± 331	55.2 ± 6.6	3.1 ± 0.3
PLA 90°	2738 ± 299	33.5 ± 4.7	1.5 ± 0.1

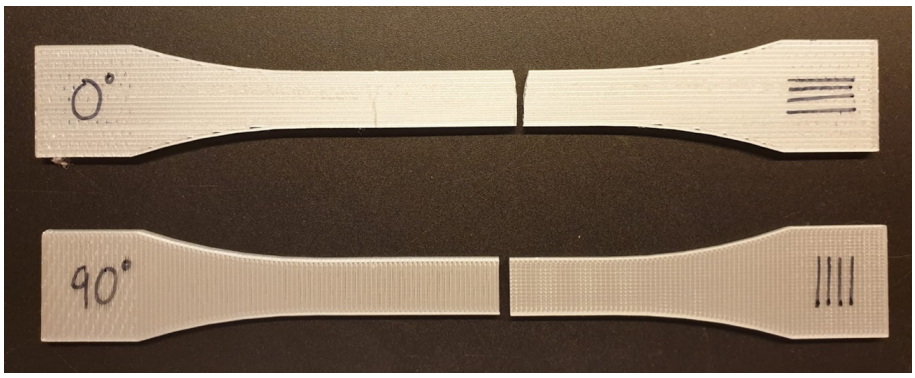

Figure 9: PLA tested specimens after failure.

5.1.2 ABS

Figure 10 shows experimentally obtained stress-strain curves for 0° and 90° specimens. For the 0° specimen, it is possible to observe the linear elastic deformation and yielding, after which there is plastic deformation with associated neck propagation, until the rupture of the specimen. On the other hand, the rupture of the 90° specimen happened on the elastic domain.

The average stiffness and strength for 90° specimens reached only 66% and 48%, respectively, of the values measured for 0° specimens. This comes as a result of the weak adhesion between adjacent filaments. The propagation of the crack through the longitudinal direction on the 0° specimen (see Figure 11) corroborates that fact.

The measured mechanical properties for ABS are shown in Table 5.

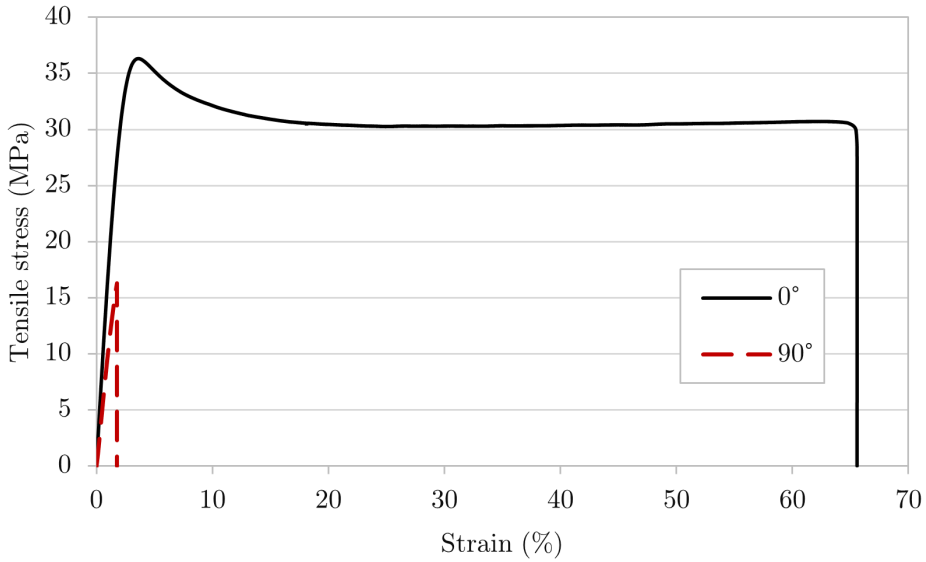

Figure 10: ABS experimental tensile stress vs strain curves.

Table 5: Experimentally obtained mechanical properties of ABS specimens.

	Young's modulus (MPa)	Tensile strength (MPa)	Strain to failure (%)
ABS 0°	1743 ± 54.1	36.7 ± 0.5	55.9 ± 14.7
ABS 90°	1157 ± 65.8	17.6 ± 2.4	2 ± 0.4

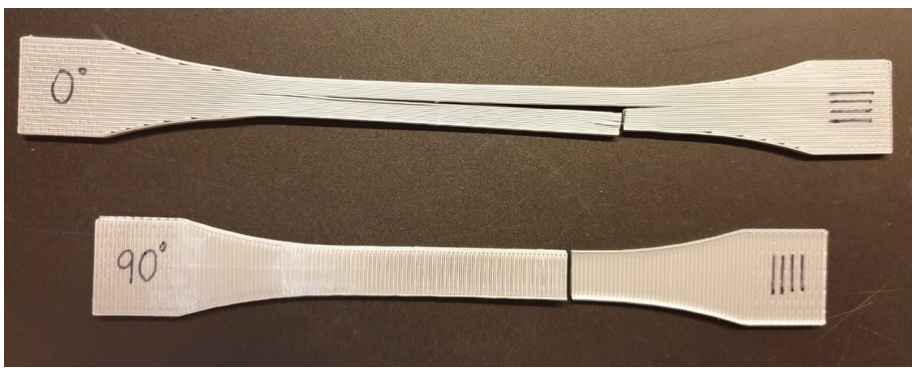

Figure 11: ABS tested specimens after failure.

5.1.3 PETG

PETG was found to have a good ductility when printed in the orientation of the applied load (0° specimens), having reached a maximum strain to failure of 220%. Nevertheless, the ductility of PETG is highly affected by the raster angle – regarding 45° and 90° specimens, the maximum strain to failure was of 4.2%. This abrupt decrease results from a poor adhesion between adjacent filaments. Figure 12 shows the obtained stress-strain curves.

It is possible to see, in Figure 13, the neck propagation that resulted from the high plastic deformation that the 0° specimen underwent before failure. Regarding the remaining specimens, there was brittle failure with the crack propagation occurring along the raster orientation.

Despite its accentuated anisotropic behaviour regarding elongation, the measured stiffness and tensile strength values for each printing direction were reasonably close. As expected, the maximum obtained values of stiffness and tensile strength were measured for 0° specimens (1933 MPa and 46 MPa, respectively). Table 6 shows the obtained mechancial properties.

Table 6: Experimentally obtained mechanical properties of PETG specimens.

	Young's modulus (MPa)	Tensile strength (MPa)	Strain to failure (%)
PETG 0°	1855 ± 71.3	45.7 ± 0.3	187.8 ± 31.7
PETG 45°	1653 ± 142.7	33 ± 1.4	3.8 ± 0.4
PETG 90°	1775 ± 255.9	33.9 ± 3.2	2.6 ± 0.3

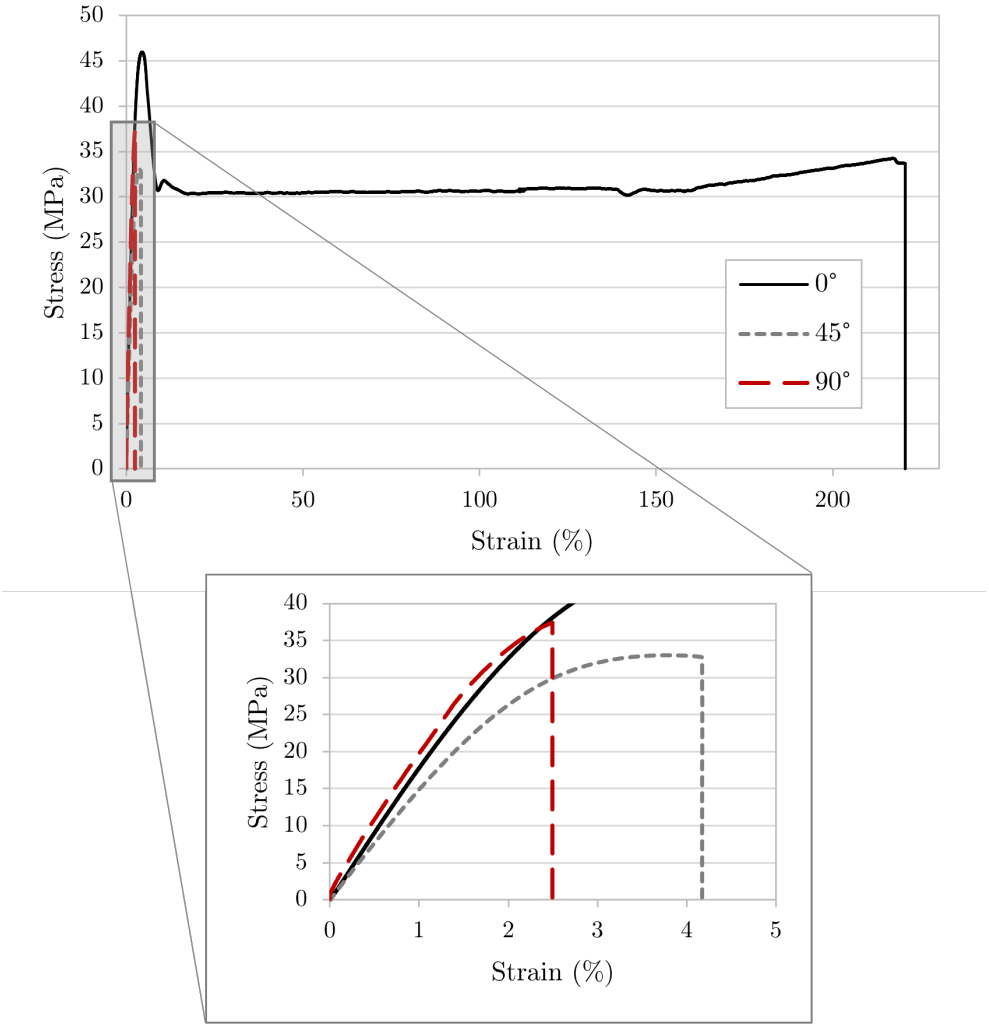

Figure 12: PETG experimental tensile stress vs strain curves.

Figure 13: PETG tested specimens after failure.

5.1.4 PC

Regarding PC, the average measured Young´s modulus and tensile strength were identical for 0° and 45° specimens. For 90° raster angle specimens the stiffness remained almost the same and there was a small decrease in strength, since the specimens failed

before yielding. As in all the studied materials, the biggest difference was noted in strain to failure, where a 0° raster angle allowed for a much higher elongation when compared to the other printing orientations. Figure 14 shows representative curves of the tensile tests performed, for each raster orientation. The measured mechanical properties are reported in Table 7.

Figure 15 shows the tested specimens after failure. It can be noted that for the 0° specimen there was a large plastic deformation, along with significant neck propagation. The same thing happens for the 45° specimen, where there is some plastic deformation, but in a much lower degree. For the 90° specimen, a brittle fracture, along the raster orientation was observed.

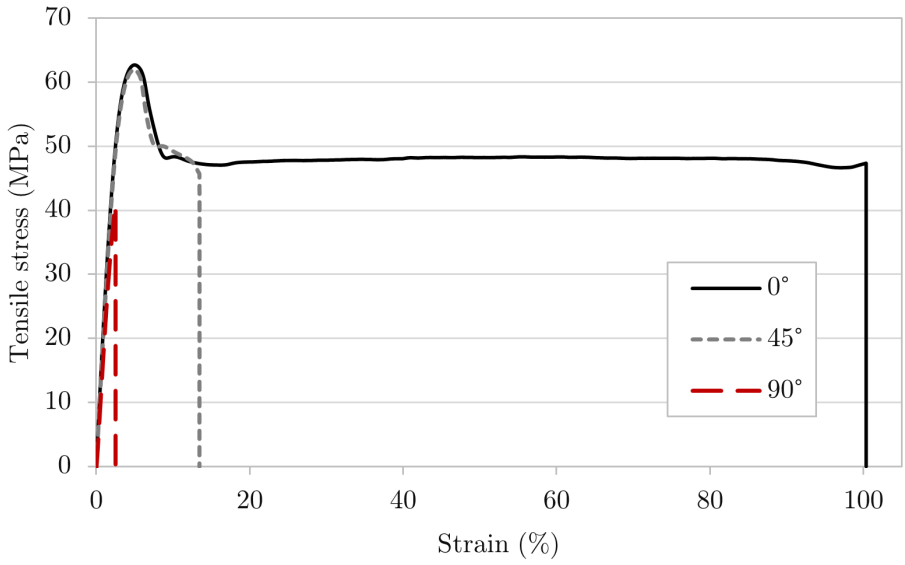

Figure 14: PC experimental tensile stress vs strain curves.

Table 7: Experimentally obtained mechanical properties of PC specimens.

	Young's modulus (MPa)	Tensile strength (MPa)	Strain to failure (%)
PC 0°	2300 ± 130.7	63.1 ± 0.8	86.2 ± 25.1
PC 45°	2309 ± 24.4	61.5 ± 1.2	11.8 ± 5.1
PC 90°	2230 ± 335.1	45.3 ± 5.2	2.7 ± 0.2

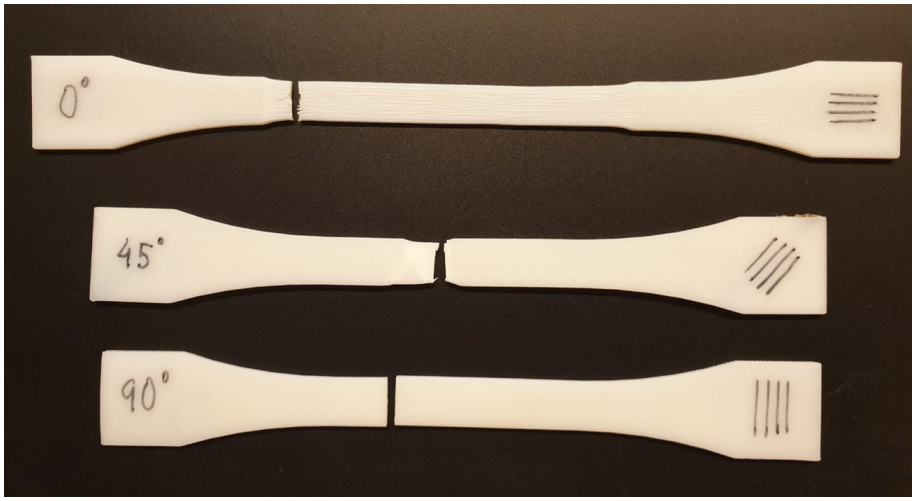

Figure 15: PC tested specimens after failure.

5.1.5 TPU

As expected, due to its elastomeric nature, TPU revealed very high elongation with a maximum measured strain to failure of 456%, for 0° specimens. It is relevant to note that although this material reaches high elongation values, it suffers very low plastic deformation, recovering almost to its initial shape after being unloaded (see Figure 17). Although TPU is able to reach a high degree of elongation regardless of the raster orientation,as shown by the stress-strain curves (Figure 16), the anisotropic mechanical properties become evident when comparing the tensile strength and strain to failure values for each printing direction. The strength and strain to failure values obtained with for 90° raster angle compose only about 42% and 44% of the ones obtained for 0° specimens, respectively. The measured mechanical properties are shown in Table 8.

Table 8: Experimentally obtained mechanical properties of TPU specimens.

	Young's modulus (MPa)	Tensile strength (MPa)	Strain to failure (%)
TPU 0°	96 ± 28.3	41.4 ± 1.8	420.1 ± 36.2
TPU 45°	121 ± 20.4	27.2 ± 2.4	348.5 ± 8.8
TPU 90°	104 ± 15.5	17.3 ± 0.5	186.1 ± 17.0

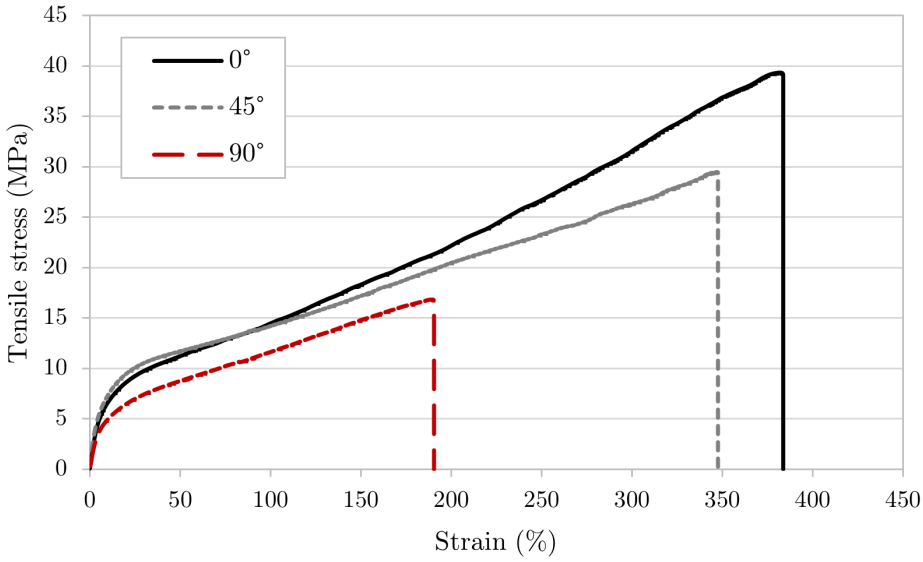

Figure 16: TPU experimental tensile stress vs strain curves.

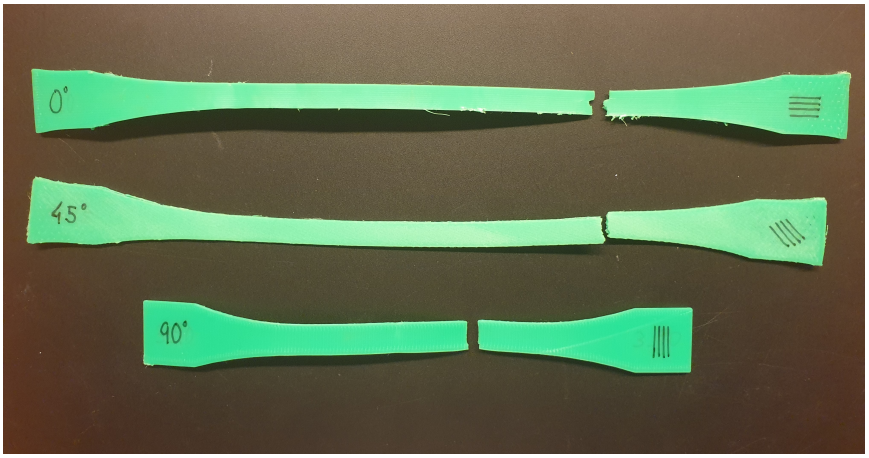

Figure 17: TPU tested specimens after failure.

5.1.6 Comparison of mechanical properties

Figures 18-20 show a comparison of the Young's modulus, strength and strain to failure, obtained for each material and raster orientation.

ABS and PLA were found to be the most brittle materials among the test. Out of the tested materials, ABS showed the most noutorious anisotropic behaviour concerning strength and stiffness. Although PLA is the material with the highest stiffness, it is also the most brittle one. Furthermore, PC stands out with a high stiffness, only falling behind PLA, and the highest strength, for each printing direction. Also, it showed similar stiffness and strength when printed with 0° and 45 ° raster angles.

TPU's elastomer nature became evident. While being the less stiff material, by a large margin when printed with a 0° raster orientation, it was able to quadriplicate its initial

size.

Regarding ductility, only TPU was able to undergo a higher elongation than PETG, when printed with a 0°raster angle. Although it could reach a strain to failure when loaded along the printing orientation, PETG's ductility revealed to be highly anisotropic, and fell abruptly when printed with 45°and 90°raster angles.

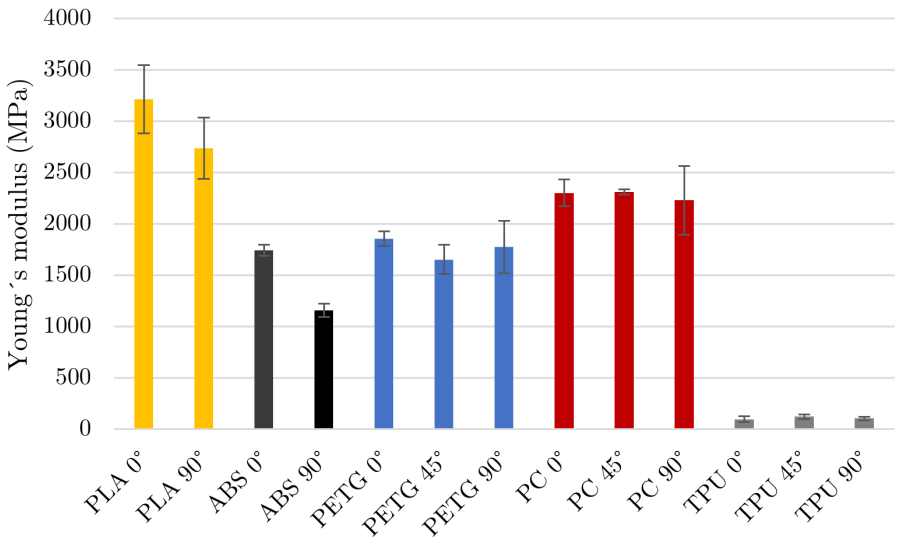

Figure 18: Materials' Young's modulus comparison.

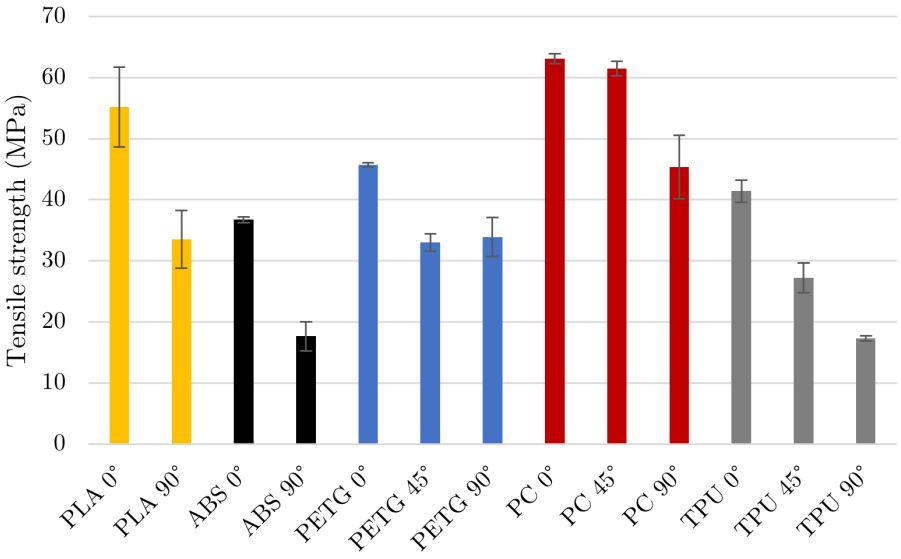

Figure 19: Materials' tensile strength comparison.

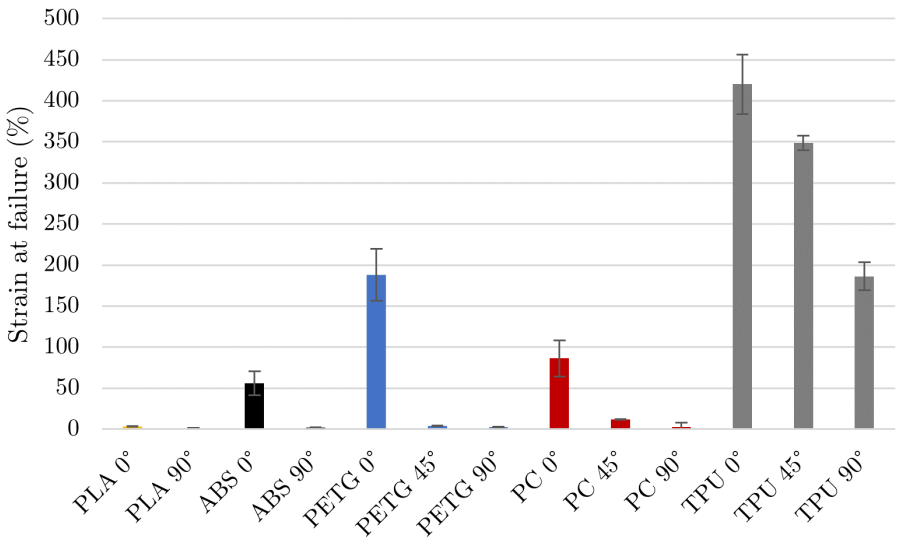

Figure 20: Materials' strain to failure comparison.

5.2 Compression testing

5.2.1 PC reference EAS

For the 0° reference structure there was smooth plastic deformation after yielding, with associated ductile damage. On the other hand, the 90° structure behaved in a brittle way. Although there was some degree of ductile damage inflicted on the structure, there was brittle fracture all around the structure. This is due to the bending stress that is generated around the layers' interface when the compression load is applied. Cracks are generated at those sites due to the weak interlayer adhesion, causing reasonable degree of brittle failure on the structure. The abrupt decreases in the load are a result of this phenomenon (see Figure 21). This behaviour follows the same trend of the tensile tests, where brittle failure was observed when the raster orientation was perpendicular to the applied load. Table 9 shows the calculated energy absorption and stiffness for PC structures.

Table 9: Calculated values of energy absorption until a 10 mm reduction in height and stiffness, for PC reference EAS.

	Energy absorbed until d = 10 mm (J)	Stiffness (N/mm)
PC 0°	46.9 ± 0.6	4415 ± 197
PC 90°	30.8 ± 1.3	3757 ± 39

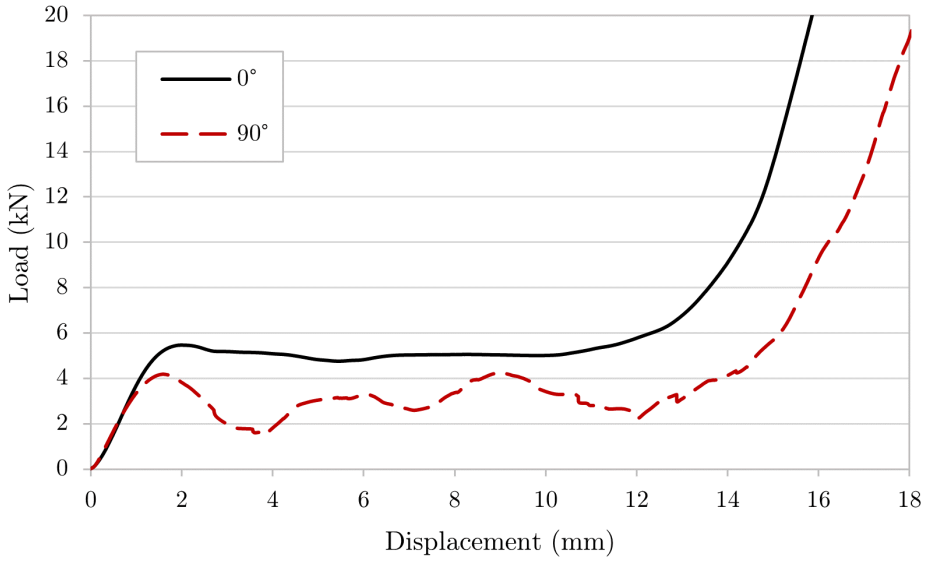

Figure 21: PC 0° and 90° reference EAS compression test load-displacement curve.

5.2.2 PETG reference EAS

Similarly to PC, the 0°PETG structure suffered a smooth plastic deformation when compressed, while brittle failure was observed in the 90° structure compression test, along with some degree of ductile damage, following the tensile tests trend. The abrupt decreases in the load-displacement curve of the latter are a product of that (see Figure 12). As expected, the force require to deform and compress the PETG structures (crush load) than for the PC counterparts, as was the energy absorbed by those. Table 11 shows the calculated energy absorption and stiffness for PETG structures.

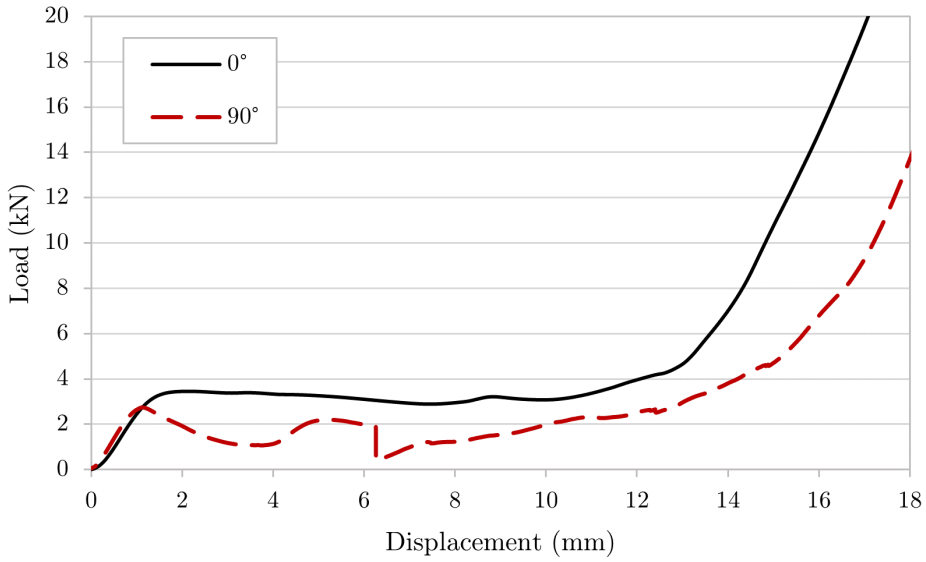

Figure 22: PETG 0° and 90° reference EAS compression test load-displacement curve.

Table 10: Calculated values of energy absorption until a 10 mm reduction in height and stiffness, for PETG reference EAS.

	Energy absorbed until d = 10 mm (J)	Stiffness (N/mm)
PC 0°	46.9 ± 0.6	3049 ± 106
PC 90°	15.6 ± 2.0	3124 ± 91

5.2.3 TPU reference EAS

TPU, being the most elastic material among the three, showed reduced plastic deformation and no fracture when compressed until densification was attained. Although the 0° structures were able to absorb a higher amount of energy than the 90° ones, the difference was negligible. Unlike the PC and PETG counterparts, TPU 90° structures did not fracture, resulting in a smooth deformation (see Figure 23). When decompressed the structures recovered elastically the greater part of their shape. Table 8 shows the calculated energy absorption and stiffness for TPU reference structures.

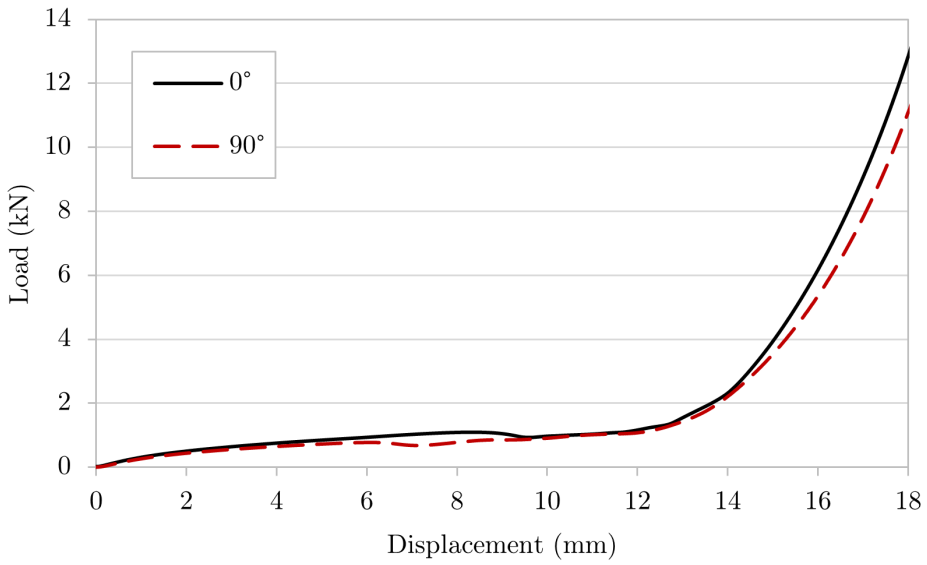

Figure 23: TPU 0° and 90° reference EAS compression test load-displacement curve.

Table 11: Calculated values of energy absorption until a 10 mm reduction in height and stiffness is attained, for TPU reference EAS.

	Energy absorbed until d = 10 mm (J)	Stiffness (N/mm)
TPU 0°	7.8 ± 0.6	336 ± 28
TPU 90°	6.0 ± 0.3	266 ± 32

5.2.4 Comparison of reference EAS tests results

Figures 24 and 25 show the comparison between the average absorbed energy until a 10 mm compression and stiffness of each reference structure configuration.

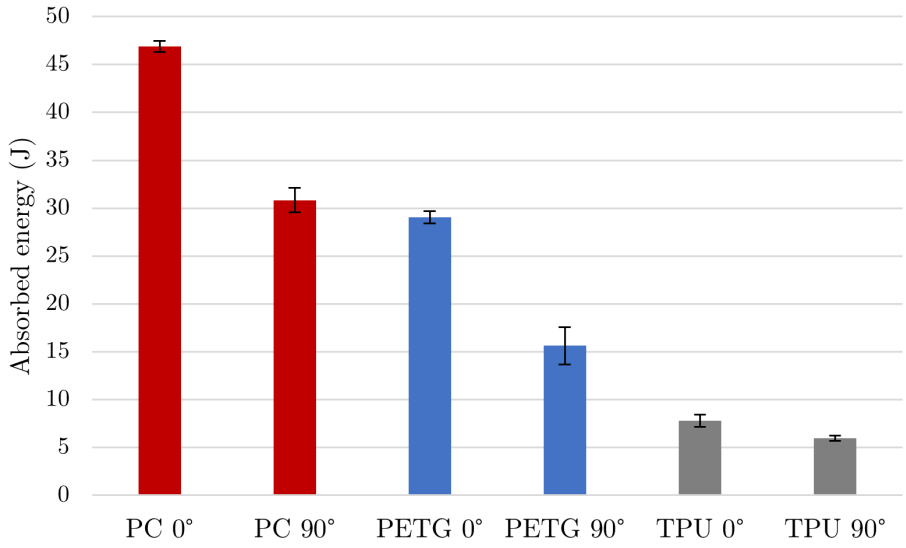

Figure 24: Comparison between the average absorbed energy values until a 10 mm reduction in height, for each material and build orientation.

As expected, polycarbonate structures registered the highest stiffness and highest crush load (plateau region) among the three materials - around 5 kN for the 0° structures. Hence, those were able to absorb and dissipate the most amount of energy among the three tested materials. Moreover, polycarbonate demonstrated the best printability among the three polymers. On the other hand, TPU structures obtained the lowest stiffness and energy absorption among the three tested materials when compressed until a 10 mm height reduction is attained. It also showed to be the hardest material to print, with excessive stringing being an issue, especially for the 90° structures.

It can be concluded that the build orientation plays a major role on the quality of the printed specimens and their deformation behaviour. The existing overhangs when printing the 90° structures lead to a worse appearance, when compared to the 0° counterparts,

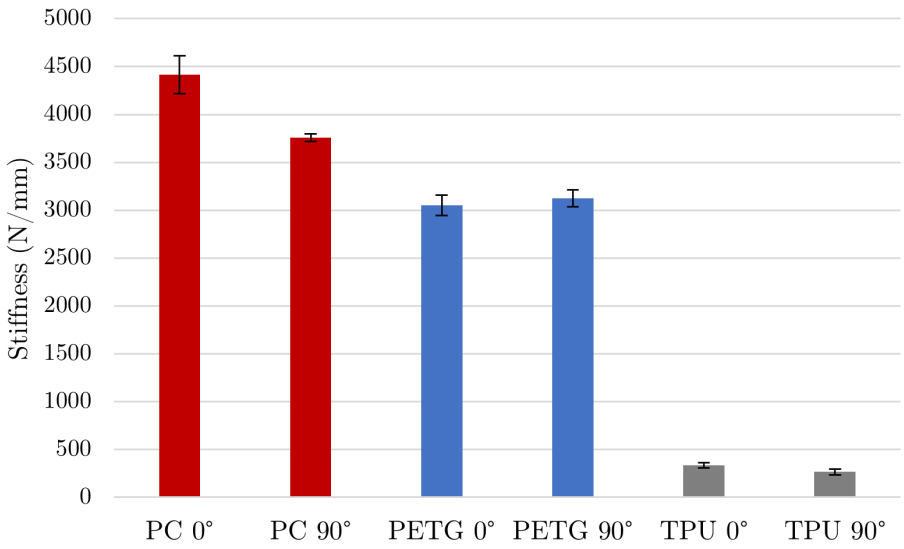

Figure 25: Comparison between the average stiffness, for each material and build orientation.

with some stringing and excessive oozing happening in some locations of the printed parts. The brittle fracture behaviour of PC and PETG 90° reference structures also shows the negative effect of that build orientation on the obtained mechanical properties. During compression, due to the poor cohesion between layers, the bending stresses generated along the structure walls lead to the opening of cracks in those locations. This translates into abrupt decreases of the exerted load and, consequently, a reduction of the absorbed energy by these structures, when compared to their 0° counterparts. The higher presence of structural defects that results from the build orientation, regarding 90° reference structures, also contributes to an irregular and more unpredictable failure process. This aspect is emphasized by the higher variability of the energy absorption values obtained for the 90° PC and PETG structures. Furthermore, the full compaction of the structures - densification - occurs slightly later when brittle fracture occurs, due to the detachment of splinters and the spreading of the material across a higher area.

5.3 Validation of material modelling

Table 12 shows the obtained values of X, Y and W, for each material. Once these three strength parameters were obtained, it was possible to predict the ultimate tensile stress for any angle by resorting to Eq.7. Figure 7 shows the prediction of the ultimate tensile stress values, regarding the raster angle, for each material.

It was then possible to calculate the values of F, G, H, and N parameters shown in 13.

The Hill's anisotropy coefficients could then be calculated, resorting to Eq.9 and inputted in Abaqus. These are shown in Table 14.

Table 12: Calculated values of X, Y and W.

Material	X (MPa)	Y (MPa)	W (MPa)
PC	63.1	45.4	35.2
PETG	44.8	33.9	17.7
TPU	31.8	17.3	15.1

Table 13: Calculated values of F, G, H, and N.

Material	F	G	H	N
PC	4.03×10^{-4}	1.25×10^{-4}	1.25×10^{-4}	4.04×10^{-4}
PETG	6.22×10^{-4}	2.49×10^{-4}	2.49×10^{-4}	1.59×10^{-3}
TPU	2.83×10^{-3}	4.94×10^{-4}	4.94×10^{-4}	2.20×10^{-3}

Table 14: Calculated anisotropy coefficients.

Material	R_{11}	R_{22}	R_{33}	R_{12}	R_{13}	R_{23}
PC	1	0.6892	0.6892	0.9654	1	1
PETG	1	0.7567	0.7567	0.6862	1	1
TPU	1	0.5448	0.5448	0.82	1	1

The true stress-plastic strain curves obtained for each material are shown in Figure 27. The correct definition of these curves is of utmost importance for the accurate prediction of the materials' behaviour since they provide information about their response to plastic deformation, including its strength, ductility, and strain hardening.

Figures 28-30 show the load-displacement curves obtained from the numerical simulations, for the 0° specimens, along with different stages of the numerically simulated deformation process. The onset of plastic deformation and neck propagation were accurately reproduced for PC and PETG. Regarding TPU, the numerical results accurately correlate to the experimental data until just above a 200 mm displacement. After that displacement value, the load starts to decrease and the numerical simulation stops due to the excessive elongation that the elements are subjected to.

Having the material model validated by the tensile tests simulations, the critical damage values, according to the already mentioned criteria, were obtained. The validity of

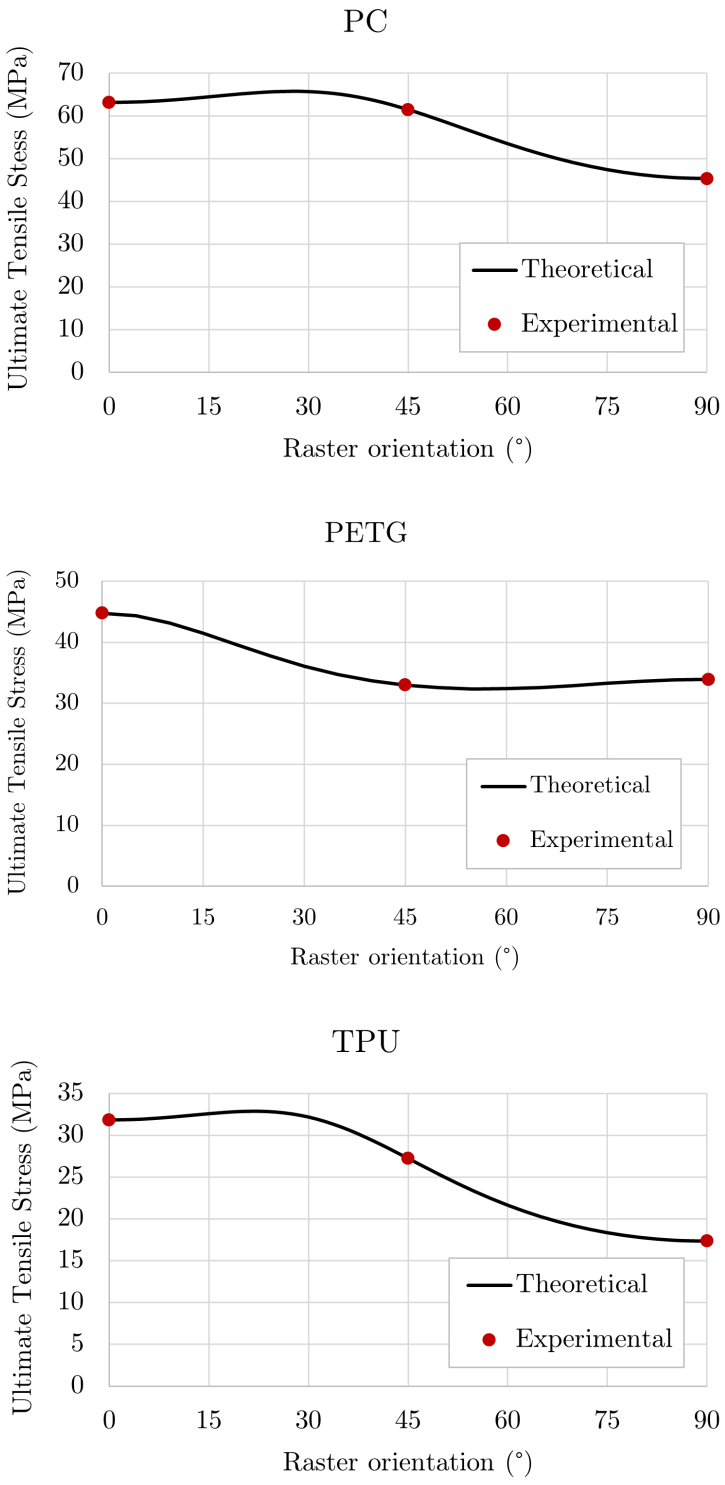

Figure 26: Comparison between experimental and theoretical ultimate tensile stress values, for each material.

the numerical model when applied to the compression of the reference EAS was then evaluated.

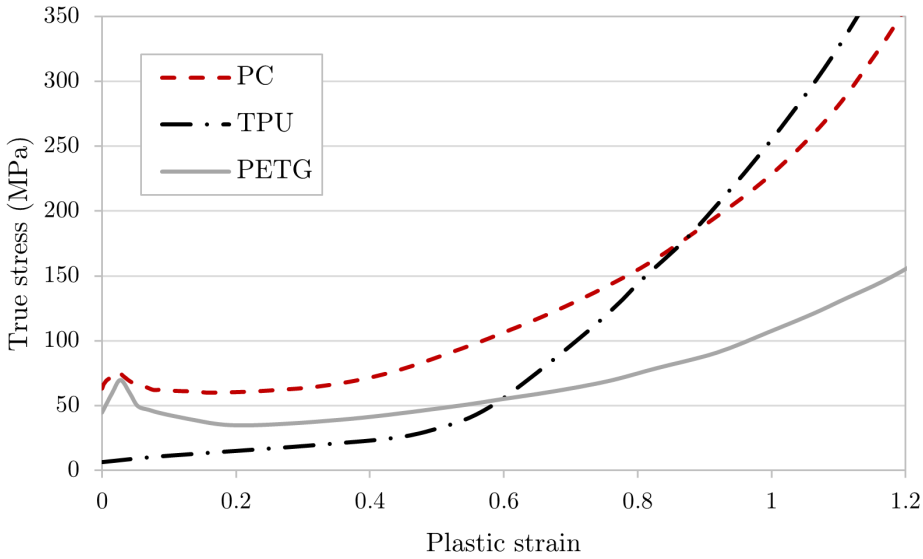

Figure 27: True stress-plastic strain curves obtained for PC, PETG and TPU.

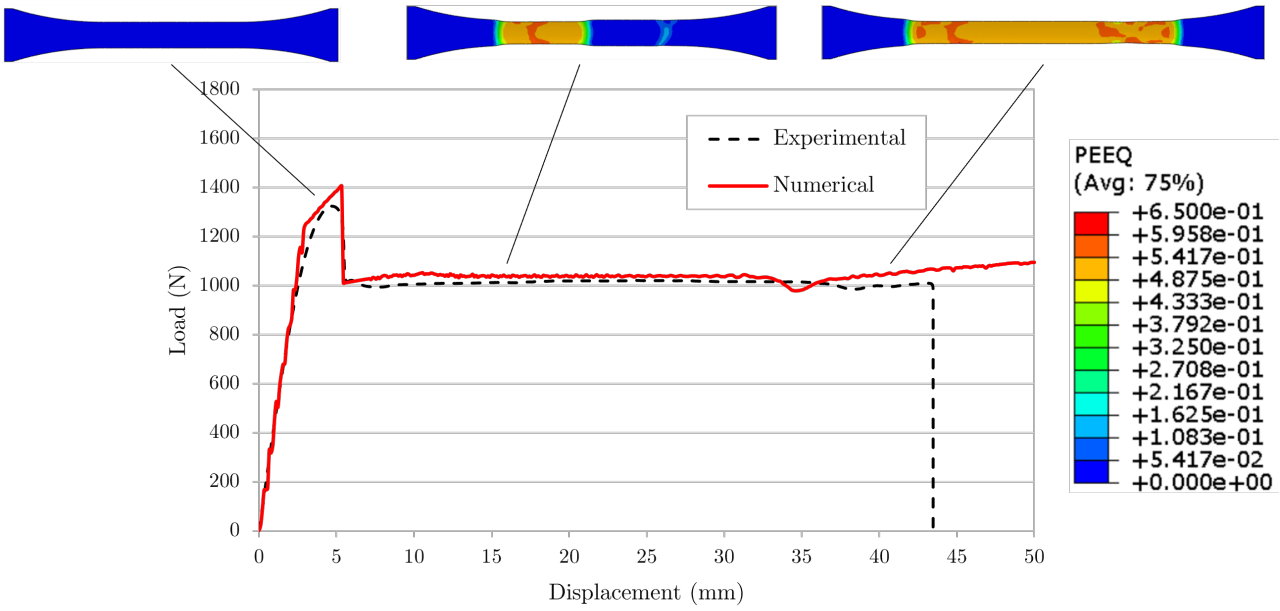

Figure 28: Comparison between PC experimental and numerical load vs displacement curves.

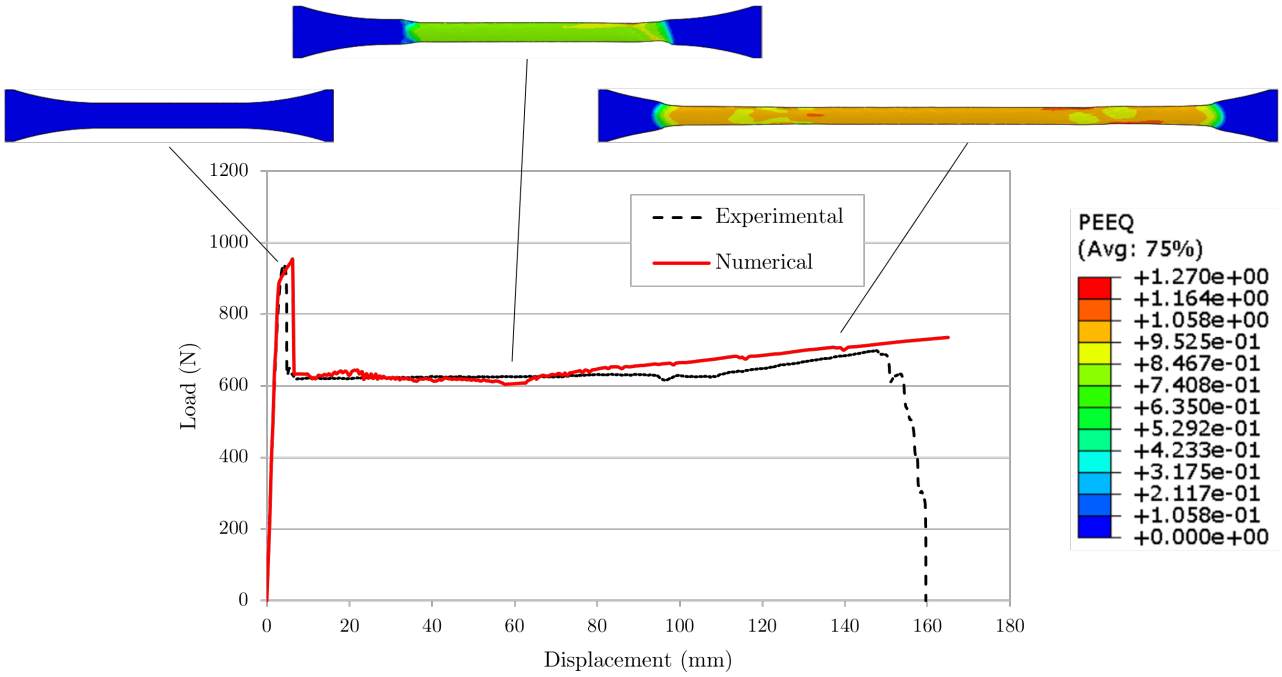

Figure 29: Comparison between PETG experimental and numerical load vs displacement curves.

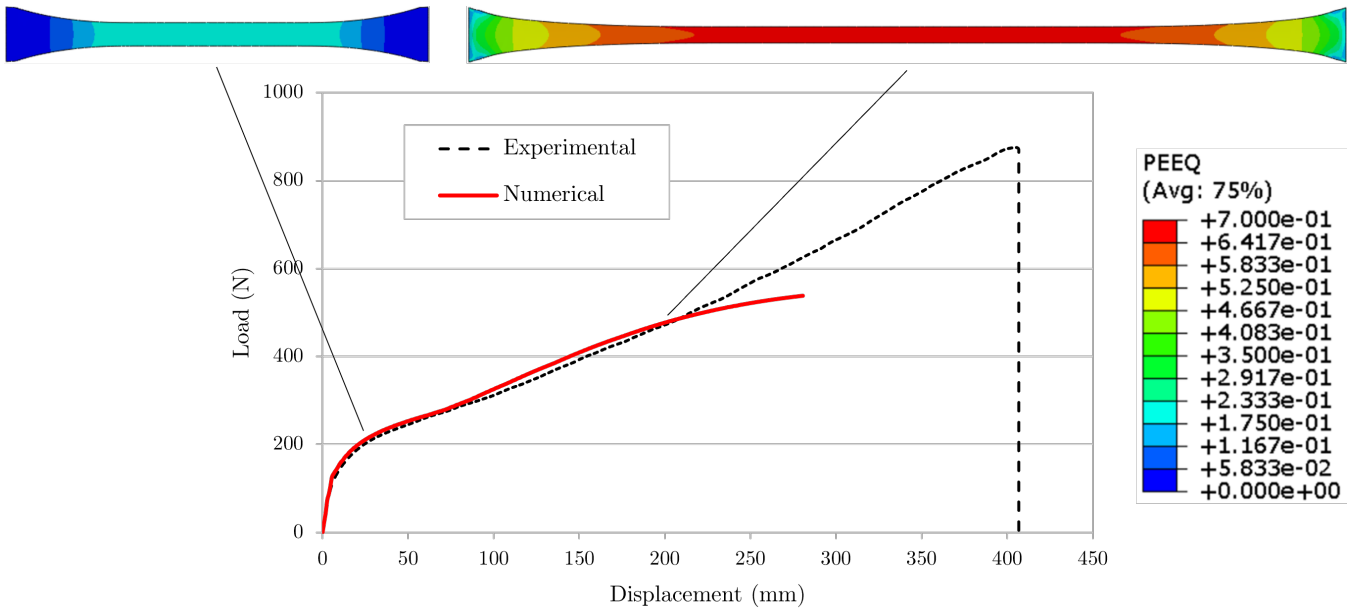

Figure 30: Comparison between TPU experimental and numerical load vs displacement curves.

5.4 Failure analysis

As already mentioned, a subroutine was used to determine the damage values, according to different ductile damage criteria, at the displacement at which the specimens failed in the tensile tests. The critical damage values for the PC and PETG 90° structures had to be calibrated by the compression tests, since there was a mixed failure mode of the structures, and not only ductile fracture. Hence, critical damage values were lower than the obtained from the numerical tensile tests, for these structures. The subroutine was then submitted in the numerical simulations of the compression tests of the reference structures, in order to induce fracture where and when the damage function reached those values. Since numerically it was not possible to reach the failure point of the TPU tensile specimens, it was also not possible to obtain the damage values which caused them to fail. Nevertheless, since no damage was observed during the experimental compression tests of the TPU structures, this did not affect the numerical analysis.

To select the most accurate ductile damage criterion among the three considered, three numerical simulations were run for the 90° PETG reference structure, each with a different model associated. The purpose of this analysis was to find out which one of the ductile damage models allowed a more accurate correlation between experimental and numerical load-displacement values and structural deformation process. The selection of the model was made based on the 90° structure, due to the greater amount of damage inflicted on those during compression and, consequently, the higher influence of the damage criteria on its compression behaviour, comparing to the 0° counterparts. Figure 31 shows a comparison between the numerical and experimental structural deformation behaviour and fracture modes for the 90° PETG reference EAS, employing the three candidate damage criteria.

Due to fracture occurring all over the PETG 90° structures when experimentally subjected to compression, and the corresponding extensive numerical element deletion, convergence issues arose past the point of fracture. However, it was possible to numerically validate the onset of fracture and fracture behaviour. In the experimental test, failure onset happens along the 45° plane with a slight deflection to the 0° plane.

As shown in the Figure 31, all three criteria accurately predict the critical regions and, hence, the deformation behaviour and fracture mode of the structure. However, there is a discrepancy in the damage predicted on their inner surfaces by the McClintock criterion compared to the other two criteria. Figure 32 shows the evolution of the damage distribution and detailed view of the fractured regions, for each criterion. This disparity is attributed to their varying fracture prediction capabilities. The McClintock criterion solely predicts tensile fracture, whereas the Brozzo and Normalized Cockroft-Latham criteria account for both tensile and shear fracture by considering Stress triaxiality and Normalized Lode angle parameters. On the outer surfaces, the damage is induced by

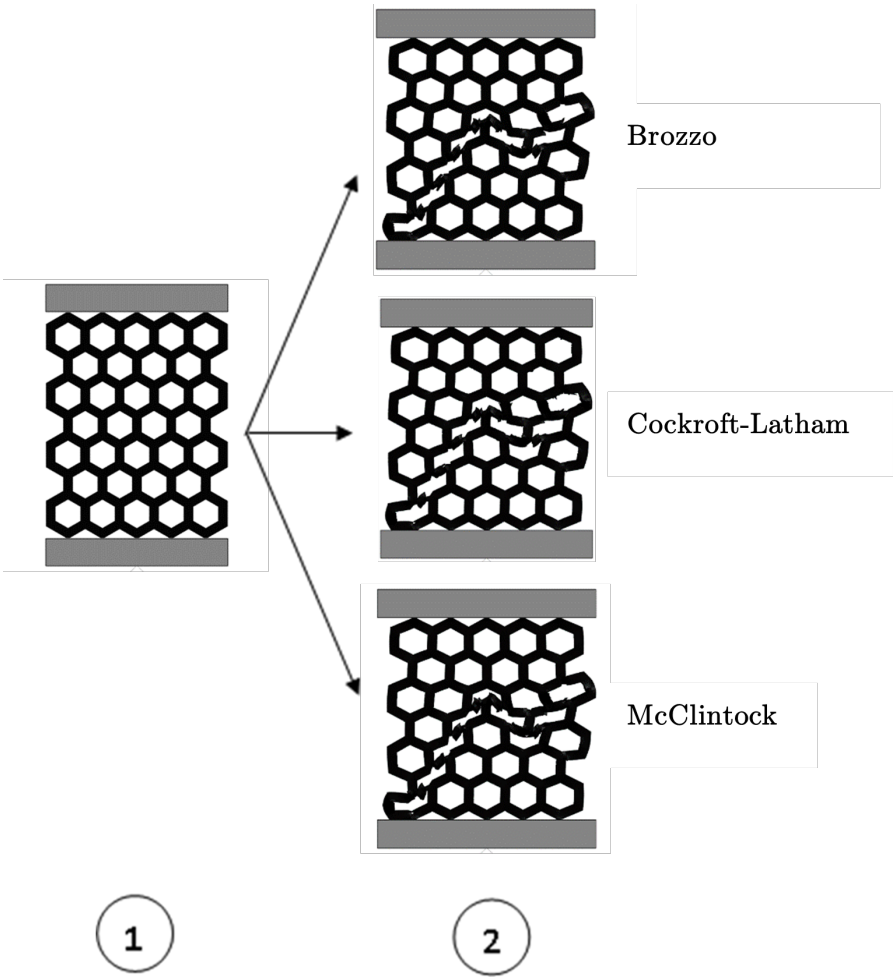

Figure 31: Comparison of PETG 90° reference EAS deformation process between numerical and experimental test, according to the considered ductile damage criteria.

tensile stresses resulting from bending (see Figure 33). This is why all three criteria correctly anticipate crack initiation at these points. On the other hand, the damage occurring on the inner surfaces is caused by shear stresses arising from the interaction of two adjacent bending areas. The McClintock criterion fails to account for this mechanism, leading to the disparity in predicted damage on the inner surfaces.

The fracture behavior observed suggests that tensile fracture primarily dominates in the critical regions during the compression of the 90^{o} structure. However, the Brozzo and Normalized Cockroft-Latham criteria provide slightly better accuracy as they consider the shear fracture that occurs in the structure under compression. Due to the more accurate correlation between numerical and experimental load values when employing Cockroft-Latham criterion, it was employed in the subsequent simulations. The critical damage values, according to this criterion, are shown in Table 15. The experimental and numerical load-displacement values obtained from the compression of the 90°PETG structure, employing Cockroft-Latham criterion, are shown in Figure 34.

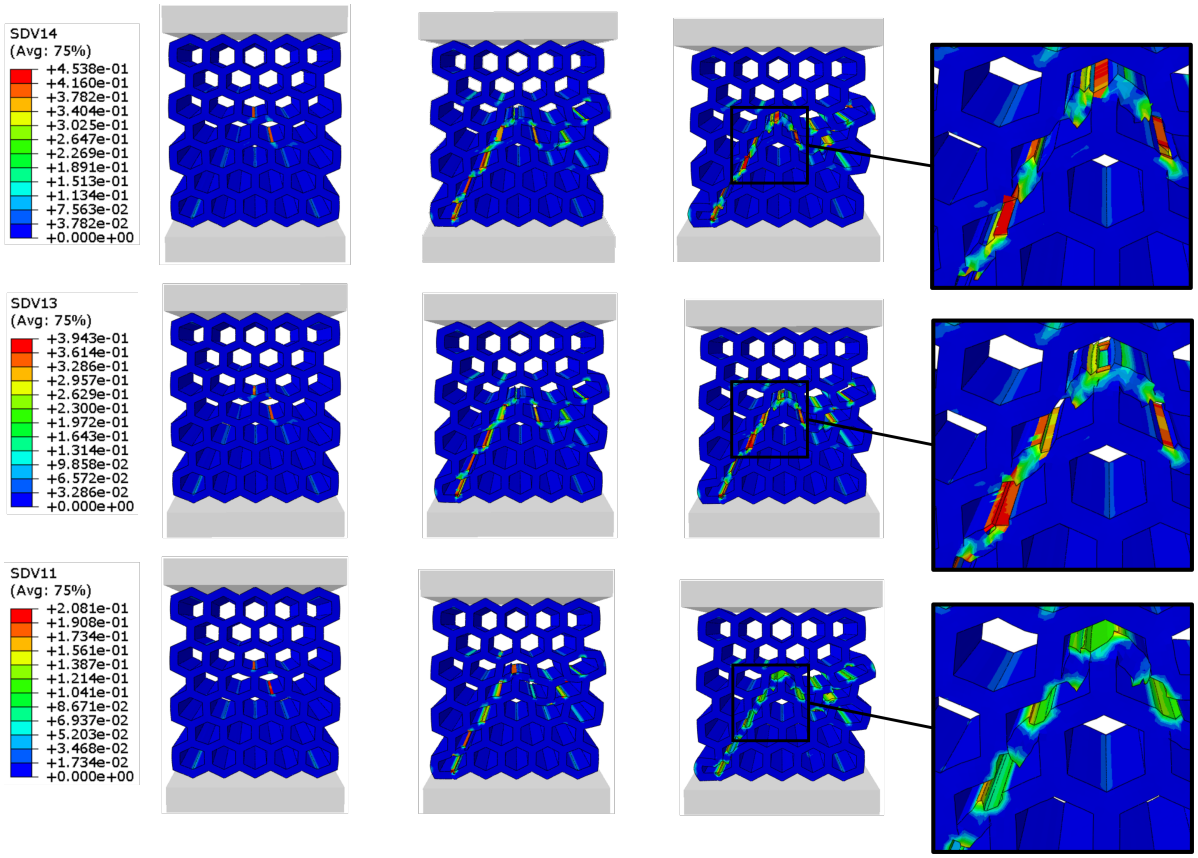

Figure 32: Damage distribution during three different stages of the numerical simulation, according to different ductile damage criteria: Brozzo (top), Cockroft-Latham (middle) and McClintock (bottom).

Table 15: Critical damage values (Cockroft-Latham criterion) obtained for 0° and 90° PETG and PC reference EAS.

		Critical damage values (Cockroft-Latham)
PETG	0°	1.26
	90°	0.3943
PC	0°	0.6257
	90°	0.3929

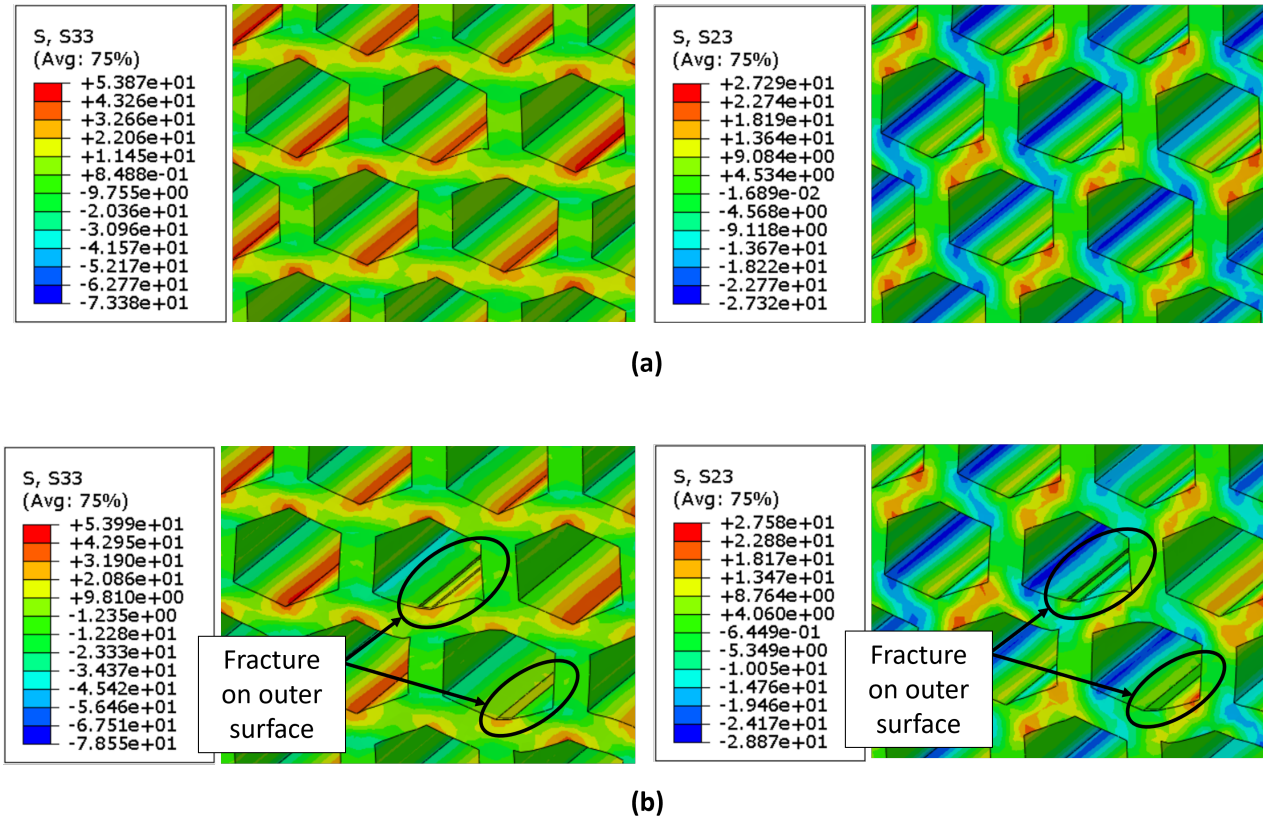

Figure 33: Tensile stress S33 (left) and shear stress S23 (right) distribution before (a) and after (b) the fracture onset on outer surface.

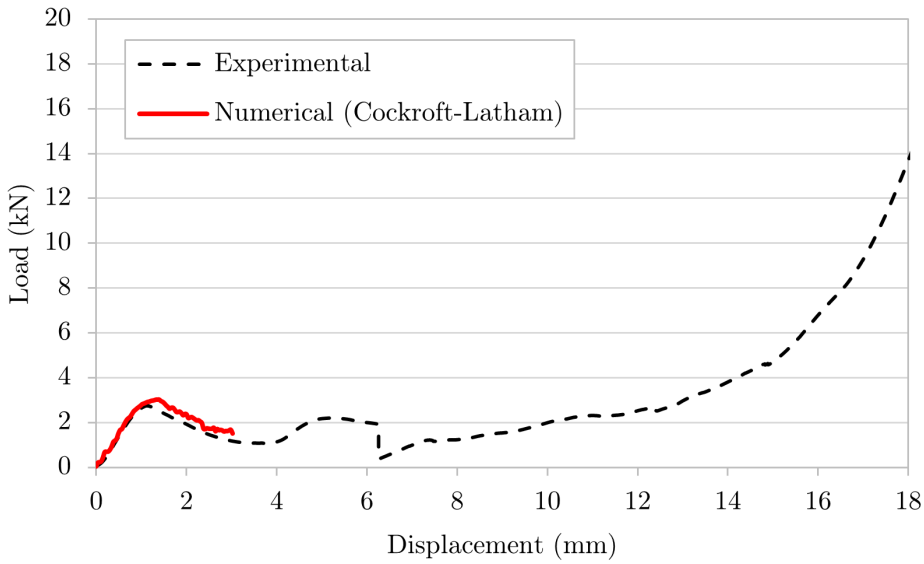

Figure 34: Comparison of PETG 90° reference EAS load-displacement values between numerical and experimental test.

The comparison between the deformation behaviour obtained in the experimental and numerical compression tests, for the 0° PETG structure, can be seen in Figure 35. A satisfactory agreement was reached, with the compression starting in the bottom cells and moving up through the structure. A good correlation between experimental and numerical load values was also reached (Figure 36).

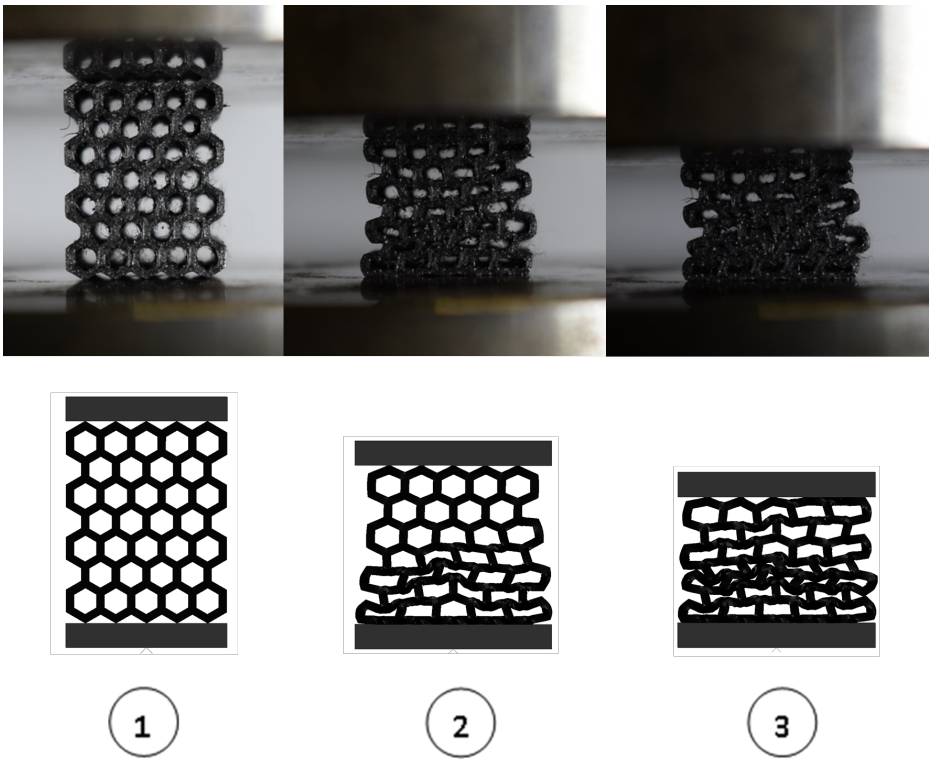

Figure 35: Comparison of PETG 0° reference EAS deformation process between numerical and experimental test, according to the considered ductile damage criteria.

Regarding the compression test of the 0° PC structure, it was possible to reach a satisfactory agreement between experimental and numerical load-displacement values, until the onset of densification at around 12 mm compression (see Figure 38). The deformation behaviour of this structure was also accurately reproduced by the numerical simulation, as shown in Figure 37. On the other hand, similarly to PETG, the mixed fracture mode with accentuated brittle behaviour of the 90° structures made so that only the onset of fracture could be accurately predicted by the numerical simulation (Figure 39). Convergence issues due to extensive element deletion hampered the running of the simulation past the point of initial failure. Although the fracture occurs along two planes in both experimental and numerical compression tests, theses planes are slightly dislocated regarding each test. This difference might be related to the structural defects that are inevitable during 3D printing, and the assumption of a perfect structure in the numerical simulation. Nevertheless, the load-displacement values, shown in Figure 40, are in good agreement.

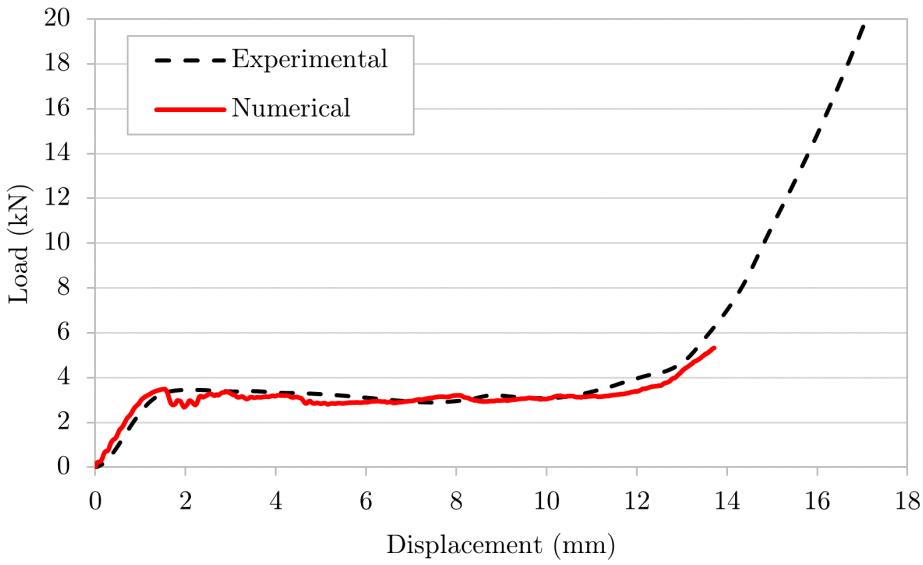

Figure 36: Comparison of PETG 0° reference EAS load-displacement values between numerical and experimental test.

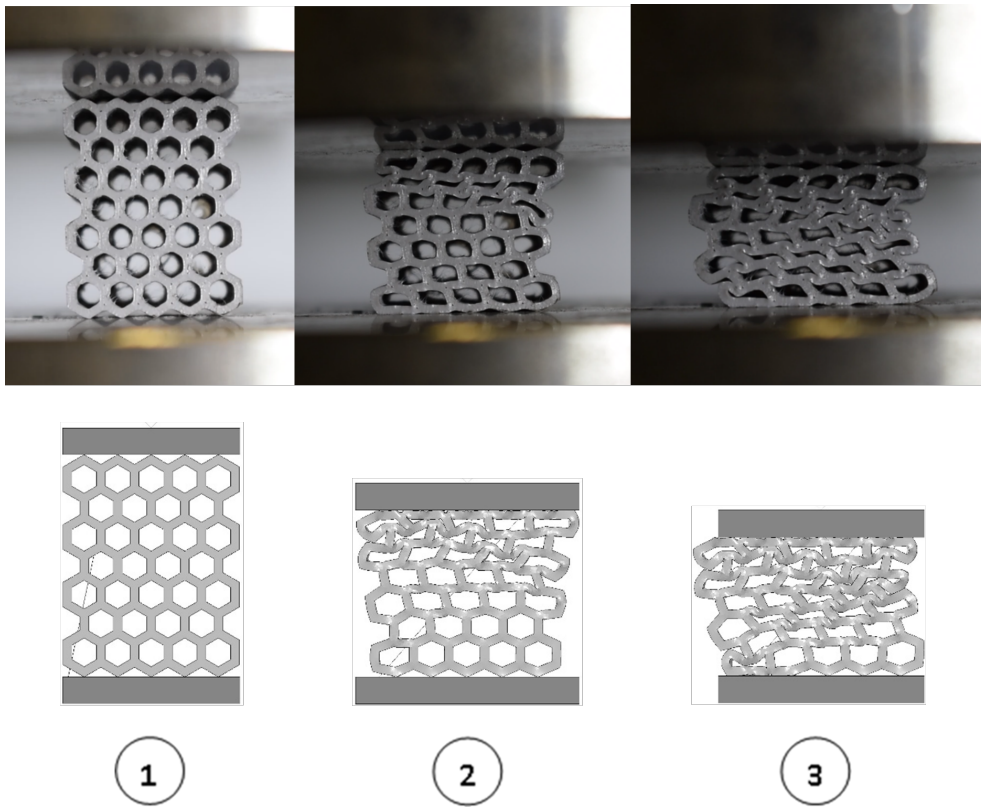

Figure 37: Comparison of PC 0° reference EAS deformation process between numerical and experimental test.

Due to the noticeably dissimilar behaviour of TPU when submitted to tension or compression loads, it was not possible to reach a good agreement between experimental and numerical results with the material's hardening curve calibrated by the tensile tests.

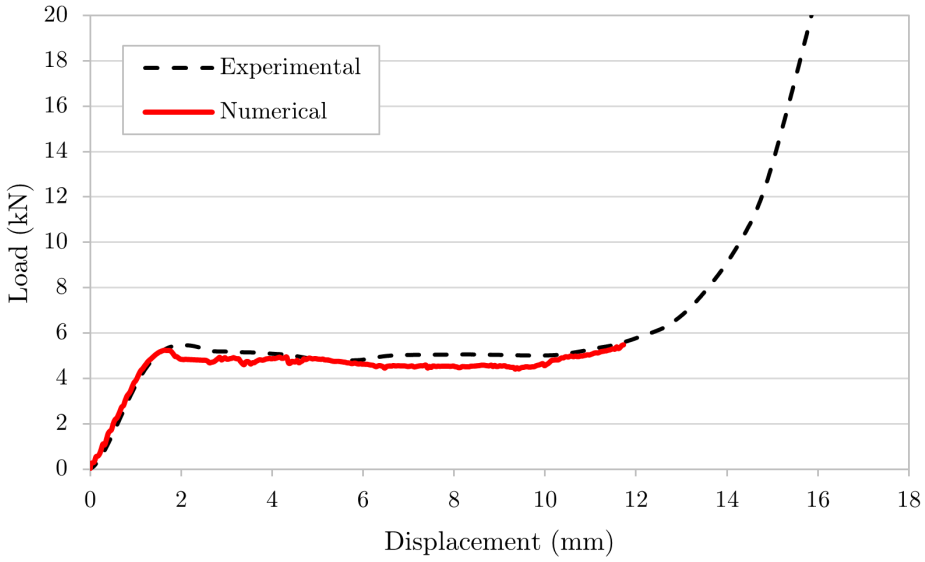

Figure 38: Comparison of PC 0° reference EAS load-displacement values between numerical and experimental test.

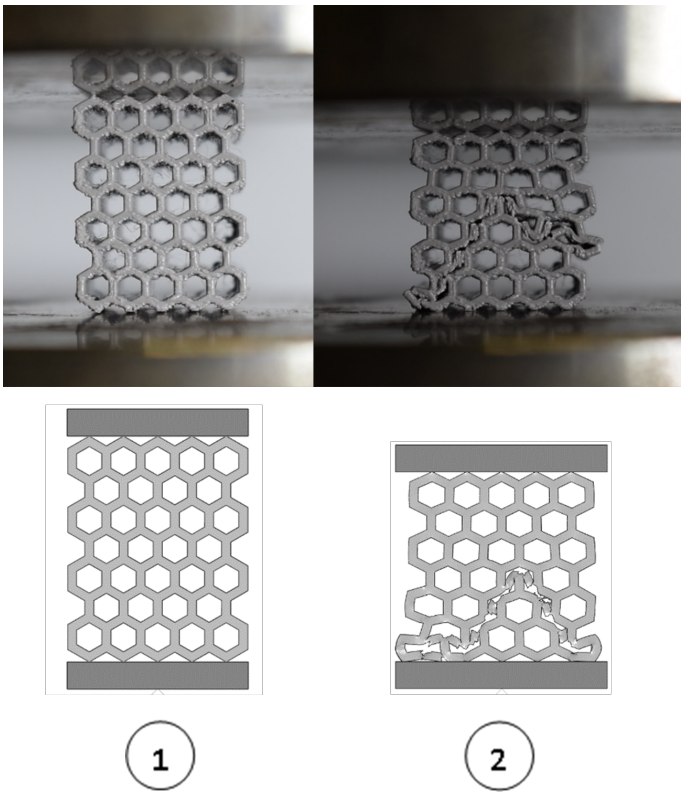

Figure 39: Comparison of PC 90° reference EAS deformation process between numerical and experimental test.

Further calibration of the TPU's material model, based on the reference EAS compression tests, was needed. Then, an accurate correlation of the deformation behaviour of the structure and load-displacement values were obtained along the entire course of the test,

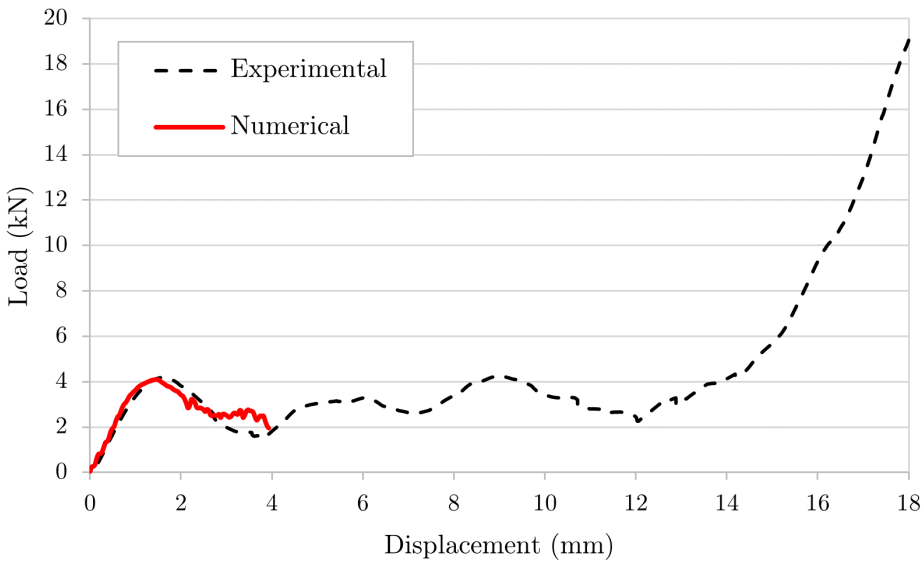

Figure 40: Comparison of PC 90° reference EAS load-displacement values between numerical and experimental test.

for both build orientation structures, as shown in Figures 42 and 44. Figures 41 and 43 shows the comparison between three stages of the experimental and numerical deformation process, before densification, for the 0° and 90° TPU reference EAS, respectively.

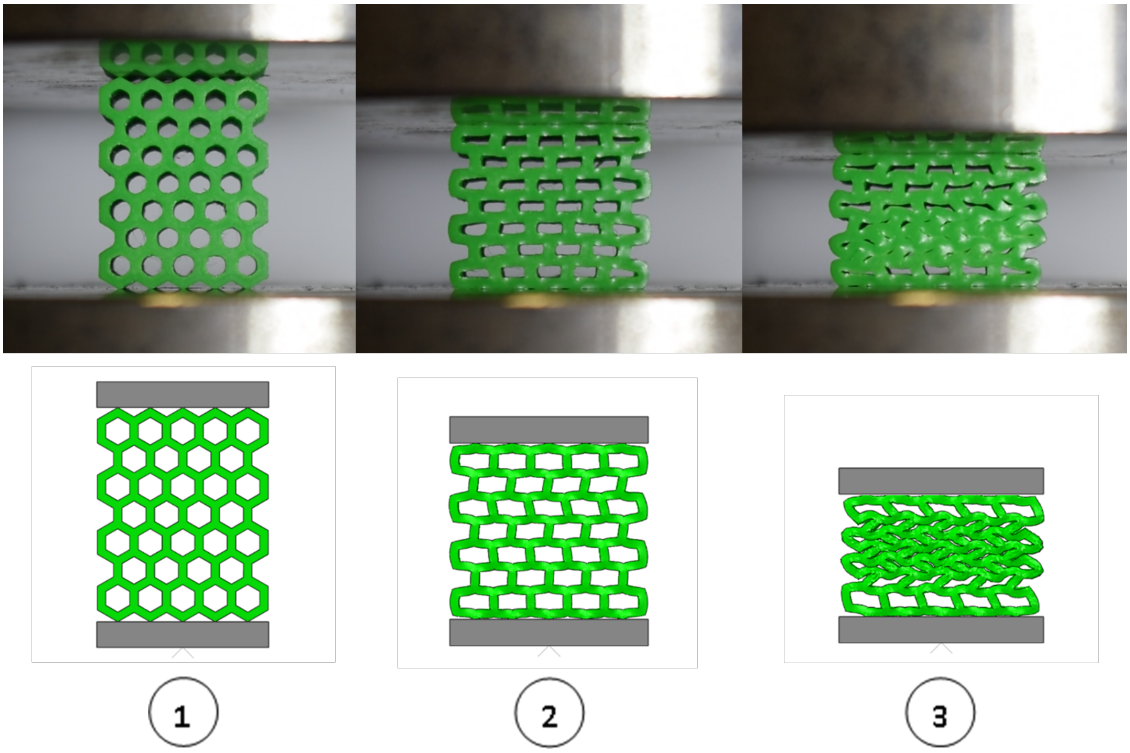

Figure 41: Comparison of TPU 0° reference EAS deformation process between numerical and experimental test.

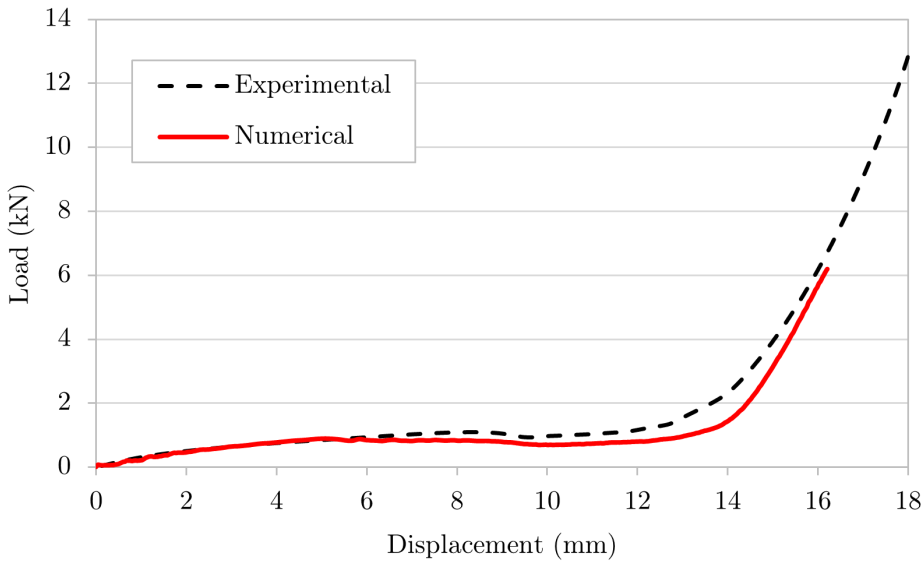

Figure 42: Comparison of TPU 0° reference EAS load-displacement values between numerical and experimental test.

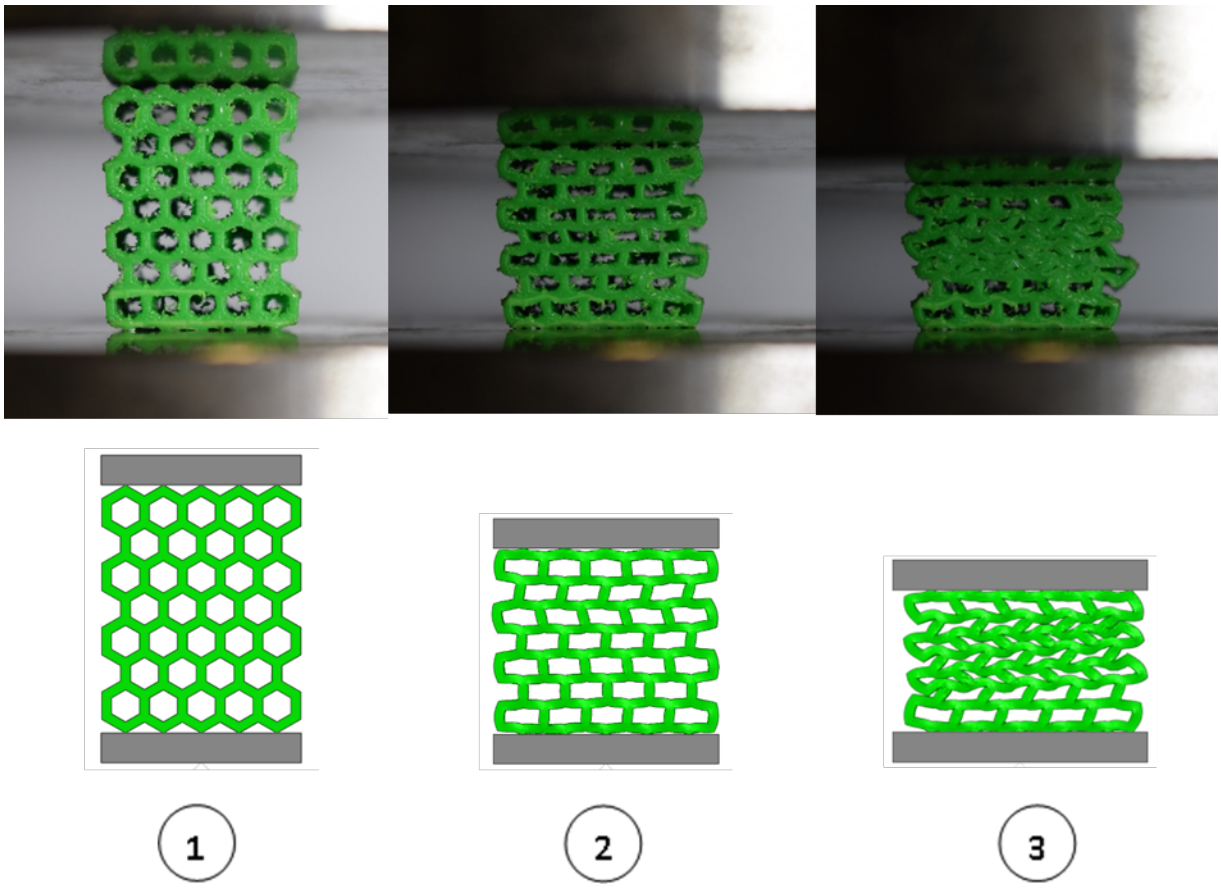

Figure 43: Comparison of TPU 90° reference EAS deformation process between numerical and experimental test.

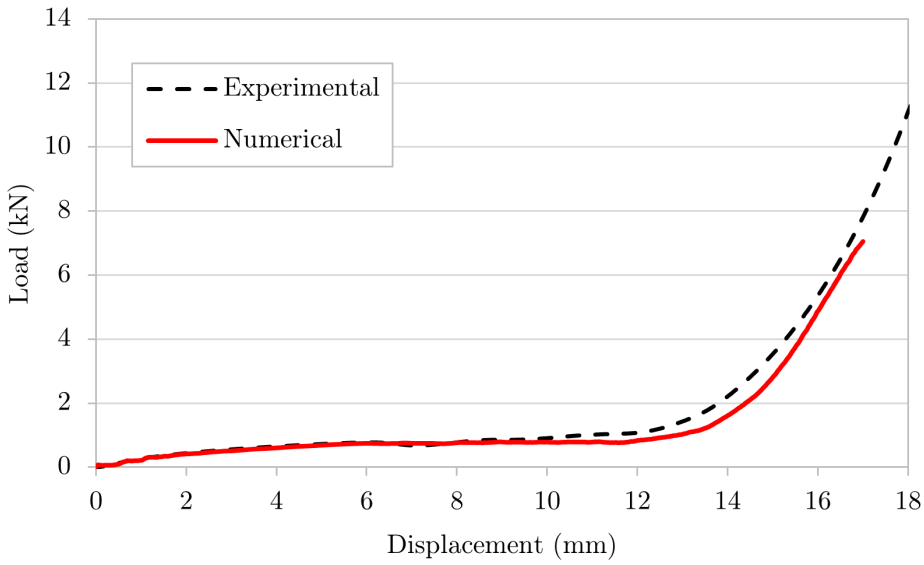

Figure 44: Comparison of TPU 90° reference EAS load-displacement values between numerical and experimental test.

6 Conclusions

A tensile characterization of multiple thermoplastics was performed in this study, in order to select the ones with most prominent mechanical properties to integrate an energy absorption structure. The anisotropic behaviour of the additively manufactured parts was assessed and modelled successfully, resorting to the Hill's yield model. For all materials, higher mechanical properties were obtained for the 0° raster orientation specimens, whereas a significant deterioration of those was verified when the raster was perpendicularly oriented to the applied load. The weak adhesion between adjacent filaments was responsible for granting this anisotropic behaviour of the 3D printed parts. PC, PETG, and TPU emerged has having the most interesting properties to be apart of an energy absorption structure.

A reference honeycomb EAS structure was modelled and tested to quasi-static in-plane compression. The influence of the build orientation on the collapsing behaviour of the structures became evident. While a parallel orientation of the layers, regarding the applied load, favours a smooth deformation process, a perpendicular orientation enhances the brittle failure of the structure, following the same trend of the tensile tests. The energy absorption capability of the tested structures was highly affected by the build orientation, with 0° being able to dissipate a higher amount. Furthermore, the notorious influence of the build orientation on the quality of 3D printed parts was noticed.

A numerical analysis was performed and the quasi-static tensile tests were simulated to calibrate the selected materials' hardening curves. A subroutine was employed so that the critical damage values, according to multiple ductile damage criteria, could be

obtained. The numerical model was then employed in the simulation of the reference EAS compression tests, for validation when applied to compression of a complex structure.

Overall, the developed model was able to accurately predict the behaviour under compression of the honeycomb structures, for both build orientations. A satisfactory agreement was reached for all three materials, with a good correlation between the fracture modes of the structures and load-displacements values. However, when brittle fracture was noticeable, only the initial failure mode could be predicted. Hence, the higher suitability of the developed numerical model for ductile and elastic materials, or build orientations that enhanced those characteristics, became evident. Regardless, it can be considered adequate for the numerical simulation of complex structures, such as energy absorption structures, under tensile and compression loading.

References

[1] S M Kabir, Kavita Mathur, and Abdel-Fattah M. Seyam. A critical review on 3d printed continuous fiber-reinforced composites: History, mechanism, materials and properties. *Composite Structures*, 232:111476, 2020.

[2] I. John Solomon, P. Sevvel, and J. Gunasekaran. A review on the various processing parameters in fdm. *Materials Today: Proceedings*, 37:509–514, 2021.

[3] B Garrido Silva, F Alves, M Sardinha, L Reis, M Leite, A M Deus, and M Fatima Vaz. Functionally graded cellular cores of sandwich panels fabricated by additive manufacturing. *Proceedings of the Institution of Mechanical Engineers, Part L: Journal of Materials: Design and Applications*, 236(9):1814–1828, 2022.

[4] Diogo Pereira, Frederico PD Alves, Luis Reis, Marco Leite, Augusto M Deus, Manuel Sardinha, and M Fatima Vaz. Cellular lattice cores of sandwich panels fabricated by additive manufacturing: Effect of dimensions and relative density on mechanical behaviour. *Proceedings of the Institution of Mechanical Engineers, Part L: Journal of Materials: Design and Applications*, 237(5):1188–1201, 2022.

[5] Ashok Dara, A Johnney Mertens, and M V Raju Bahubalendruni. Characterization of penetrate and interpenetrate tessellated cellular lattice structures for energy absorption. *Proceedings of the Institution of Mechanical Engineers, Part L: Journal of Materials: Design and Applications*, 237(4):906–913, 2022.

[6] J. Galante, G. M. F. Ramalho, M.Q. dos Reis, R. J. C. Carbas, E. A. S. Marques, and L. F. M. da Silva. *Mechanical Characterization of 3D Printed Specimens*, pages 149—-164. Springer, 2021.

[7] Manav Doshi, Ameya Mahale, Suraj Kumar Singh, and Samadhan Deshmukh. Printing parameters and materials affecting mechanical properties of fdm-3d printed parts: Perspective and prospects. *Materials Today: Proceedings*, 50:2269–2275, 2022.

[8] Mohammadreza Lalegani Dezaki, Mohd Khairol Ariffin, Ahmad Serjouei, Ali Zolfagharian, Saghi Hatami, and Mahdi Bodaghi. Influence of infill patterns generated by cad and fdm 3d printer on surface roughness and tensile strength properties. *Applied Sciences*, 11(16):7272, 2021.

[9] Mahmoud Moradi, Ahmad Aminzadeh, Davood Rahmatabadi, and Alireza Hakimi. Experimental investigation on mechanical characterization of 3d printed pla produced by fused deposition modeling (fdm). *Materials Research Express*, 8(3):035304, 2021.

[10] Cesar Omar Balderrama-Armendariz, Eric MacDonald, David Espalin, David Cortes-Saenz, Ryan Wicker, and Aide Maldonado-Macias. Torsion analysis of the anisotropic behavior of fdm technology. *The International Journal of Advanced Manufacturing Technology*, 96(1-4):307–317, 2018.

[11] Davood Rahmatabadi, Ahmad Aminzadeh, Mohammad Aberoumand, and Mahmoud Moradi. Mechanical characterization of fused deposition modeling (fdm) 3d printed parts. *Materials Forming, Machining and Tribology*, page 131–150, 2021.

[12] Patrich Ferretti, Christian Leon-Cardenas, Gian Maria Santi, Merve Sali, Elisa Ciotti, Leonardo Frizziero, Giampiero Donnici, and Alfredo Liverani. Relationship between fdm 3d printing parameters study: Parameter optimization for lower defects. *Polymers*, 13(13):2190, 2021.

[13] Ans Al Rashid and Muammer Koç. Numerical simulations on thermomechanical performance ofnbsp; nbsp; nbsp; nbsp; nbsp; nbsp; lt;scpgt;3dlt;/scpgt;nbsp; nbsp; nbsp; nbsp; nbsp; nbsp; printed chopped carbon fnbsp; nbsp; nbsp; nbsp; nbsp; nbsp; lt;scpgt;iber-reinforcedlt;/scpgt;nbsp; nbsp; nbsp; nbsp; nbsp; nbsp; polyamide-6 composites: Effect of infill design. *Journal of Applied Polymer Science*, 139(44), 2022.

[14] Mohammad Reza Khosravani, Shahed Rezaei, Hui Ruan, and Tamara Reinicke. Fracture behavior of anisotropic 3d-printed parts: Experiments and numerical simulations. *Journal of Materials Research and Technology*, 19:1260–1270, 2022.

[15] Martina Scapin and Lorenzo Peroni. Numerical simulations of components produced by fused deposition 3d printing. *Materials*, 14(16):4625, 2021.

[16] Philip Bean, Roberto A. Lopez-Anido, and Senthil Vel. Numerical modeling and experimental investigation of effective elastic properties of the 3d printed gyroid infill. *Applied Sciences*, 12(4):2180, 2022.

[17] S. K. Selvamani, M. Samykano, S. R. Subramaniam, W. K. Ngui, K. Kadirgama, G. Kanagaraj, and M. S. Idris. 3d printing: Overview of abs evolvement. *AIP Conference Proceedings*, 2019.

[18] Eda Hazal Tümer and Husnu Yildirim Erbil. Extrusion-based 3d printing applications of pla composites: A review. *Coatings*, 11(4):390, 2021.

[19] Sherri L. Messimer, Albert E. Patterson, Nasiha Muna, Akshay P. Deshpande, and Tais Rocha Pereira. Characterization and processing behavior of heated aluminum-polycarbonate composite build plates for the fdm additive manufacturing process. *Journal of Manufacturing and Materials Processing*, 2(1):12, 2018.

[20] Rebecca B. Dupaix and Mary C. Boyce. Finite strain behavior of poly(ethylene terephthalate) (pet) and poly(ethylene terephthalate)-glycol (petg). *Polymer*, 46(13):4827–4838, 2005.

[21] Qi-Wei Lu and Christopher W. Macosko. Comparing the compatibility of various functionalized polypropylenes with thermoplastic polyurethane (tpu). *Polymer*, 45(6):1981–1991, 2004.

[22] Prusa Research. Prusament. https://prusament.com/materials/, 2023.

[23] Filament PM. Filament PM. https://www.filament-pm.com/, 2023.

[24] Fillamentum. Fillamentum. https://fillamentum.com/collections/, 2023.

[25] John Ryan Dizon, Alejandro H. Espera, Qiyi Chen, and Rigoberto C. Advincula. Mechanical characterization of 3d-printed polymers. *Additive Manufacturing*, 20:44–67, 2018.

[26] Sachini Wickramasinghe, Truong Do, and Phuong Tran. Fdm-based 3d printing of polymer and associated composite: A review on mechanical properties, defects and treatments. *Polymers*, 12(7):1529, 2020.

[27] Shuheng Wang, Yongbin Ma, Zichen Deng, Kai Zhang, and Shi Dai. Implementation of an elastoplastic constitutive model for 3d-printed materials fabricated by stereolithography. *Additive Manufacturing*, 33:101104, 2020.

[28] Tianyun Yao, Zichen Deng, Kai Zhang, and Shiman Li. A method to predict the ultimate tensile strength of 3d printing polylactic acid (pla) materials with different printing orientations. *Composites Part B: Engineering*, 163:393–402, 2019.

B Paper B

Development and testing of additively manufactured bio-inspired structures for impact absorption

L.P.F. Garrido[1], M. M. Kasaei[2], F. Ramezani[2], E.A.S. Marques[1], R.J.C. Carbas[2], L.F.M. da Silva[1]

1 Mechanical Engineering Department, Faculty of Engineering (FEUP), University of Porto, Porto, Portugal

2 Institute of Science and Innovation in Mechanical and Industrial Engineering (INEGI), Porto, Portugal

Abstract:

The development of optimized, light-weight energy absorption structures (EAS) that can be incorporated in vehicles to attenuate the impact of a collision, as well as reducing the emission of CO_2 by reducing the weight of a vehicle, can contribute to both safety and sustainability. Bio-structures, such as honeycombs or spider webs, are naturally designed to endure foreign solicitations, and serve as inspiration for high performance mechanical structures. On the other hand, functionally grading the structure characteristics has been proven to enhance load-bearing efficiency and overall crashworthiness. Moreover, it can also be a way of reducing the weight of a structure. This study aims to develop and test two novel structural configurations and assess their potential for energy absorption. A multi-material honeycomb structure and a spider web graded structure were designed and fabricated through fused deposition modelling (FDM) Adhesive bonding was employed in the multi-material specimens to join the different materials. Three candidate thermoplastics, with crashworthiness potential, were chosen for this study: polycarbonate (PC), polyethylene terephthalate glycol (PETG), and thermoplastic polyurethane (TPU). Single and multi-material honeycomb and graded spider web EAS were developed and tested under quasi-static, high-rate and impact. Multiple crashworthiness parameters were calculated to assess the effect of stiffness grading and size on energy absorption capabilities. A delay in the onset of densification was observed as a result of the multi-material integration. The peak force measured during the compression of a structure was noticed to only depend on the presence of the stiffer material, and not on its proportion. Hence no influence of the size in energy absorption efficiency and specific parameters was observed. The feasibility of the multi-material solution in energy absorption applications became questionable due to unstable deformation under impact and assembly procedure. On the other hand, the spider web configuration stood out due to its better performance and ease in manufacturing.

Keywords: 3D printing, Stiffness grading, Crashworthiness

1 Introduction

In what concerns vehicle design and engineering, the capacity of managing and attenuating the energy transmitted by a collision is a key factor for vehicle safety. The integration of energy absorption structures has become a practical mean to reduce the harm caused by accidents, and increase passenger safety. These structures are intended to deform and absorb the energy in a controlled manner, thereby reducing the force transmitted to the occupants. These are distributed by the vehicle and consist on specially engineered parts that can be in the form of collapsible structures, crumple zones, or impact beams.

This paper will focus on one of these energy absorption structure (EAS): the crash box. It consists on a deformation device that is mounted between the front rail and bumper of the car, to reduce the damage caused by low-speed crashes. During a collision, crash boxes must collapse prior to adjacent structures, in order to dissipate the kinetic energy and minimize the damage inflicted to the cabin and passengers [1]. These are traditionally made of steel or aluminium, being that the latter is the most common material to integrate in these applications due to its lightweight, yet strong profile. Weight-saving demands in the automotive industry have lead manufacturers to invest in new structure designs and implementation of new materials with crashworthiness potential [2]. A potential reduction in weight of such structures allows for a greater fuel efficiency and helps to reduce the ecological footprint caused by pollutant emissions, while a more efficient energy absorption contributes to vehicle safety and can help to reduce road fatalities. The implementation of composites and hybrid materials on these energy absorption structures can be an effective way to achieve this [1]. Studies on the development of a glass reinforced plastic EAS, and the influence of different geometries on the rate of energy absorbed, when subjected to axial crush loading are reported in [2]. Furthermore, a hybrid aluminium/CFRP cylindrical EAS was compared to aluminium and CFRP net structures when submitted to different quasi-static loading angles [3]. Also, natural fibres have been being studied for a long time as substitutes of synthetic fibres, aiming towards a more environmentally friendly production. Hemp was considered as a promising candidate for sustainable energy absorption structures, with hemp fibre composite and carbon fibre composite structures obtaining similar specific energy absorption (SEA) values [4].

Geometry and material properties are the most significant influencing parameters on the efficiency of the absorption of the kinetic energy transmitted by a collision [1, 2]. Hence, multiple studies have been conducted on testing novel energy absorption structures configurations, integrating non-traditional materials or geometries, such as lattice structures [5–7], sandwich structures [8, 9], honeycomb structures [10–12], and multi-tubular structures [13]. Specially designed features such as foam-filled structures, functionally graded thicknesses or nested tubes have been reported as enhancers of the energy absorption capability of such structures [2]. In [14], a mild-steel pre-deformed EAS was

numerically submitted to crushing loads and compared to its non-deformed counterpart. The inclusion of imperfections (triggers) such as grooves or pre-deformations on energy absorption structures, in order to stabilise the deformation and reduce the peak force, has also been indicated as performance enhancer of such structures. These "crash initiators" have been reported has having an significant effect on the energy absorption performance can help reduce the rate of energy absorption, what is desirable for the safety of the passengers. Moreover, cellular structures, such as honeycombs, are able to dissipate a large amount of energy and so, these have been a topic of interest among the research community. In [15], the hexagonal honeycomb emerged as the most capable of efficient energy absorption,when nine different honeycomb structures were numerically tested to compression. Grading of these structures, in order to optimize their energy absorption capabilities has been extensively studied. Different size graded lattice/honeycomb single material structures were numerically tested in [16], along with dual-material honeycomb structures. the conclusion was made that the graded structures were effectively more capable of energy absorption, as were the multi-material solutions when compared to their single material counterparts. The same argument was made in [10], where an analytical model was used to predict the stress-strain behaviour of 3-stage density graded honeycomb structures. Furthermore, the density grading of a 3D printed (FDM) thermoplastic polyurethane (TPU) honeycomb structure allowed the increase of the densification strain and, consequently, of the total energy absorbed up to that point, when submitted to impact [11]. The retardation of the densification onset allows a more gradual energy absorption and transfers a lower stress to the part being protected. Besides honeycomb cellular structures, other bio-structures such, as bamboo structural core, fish scales or even bone structure, have been studied as potential candidates to integrate a EAS ([17]).

Conventional processes are only able to manufacture relatively simple parts. The possibility of enhancing the crashworthiness performance through geometry tuning can be magnified when resorting to non-traditional manufacturing processes such as 3D printing. Additive manufacturing is not restrained by the limitations of traditional methods, allowing for a much greater design freedom. This allows the production of lighter, more cost-effective, and environmentally friendly parts. The wastage created by traditional manufacturing techniques is also replaced by a near net shape production [18].

This paper aims to study the crashworthiness potential of bio-inspired 3D printed EAS. Firstly, an uniform honeycomb structure, tested in Paper A) was used as the reference for comparison of crashworthiness parameters and assessment of the stiffness grading effect. The size effect was also assessed. Furthermore, a spider web inspired graded EAS was developed and its crashworthiness potential was compared to the multi-material honeycomb EAS. The structures were additively manufactured resorting to fused deposition modelling (FDM) technology, and three materials were employed: polycarbonate (PC), polyethylene terephthalate glycol (PETG) and thermoplastic polyurethane (TPU). These

were submitted to quasi-static, high-rate and impact tests, and multiple crashworthiness indexes were evaluated and compared.

2 Experimental procedures

2.1 Materials

The selection of the materials to integrate the developed energy absorption structures was based on the study conducted on Paper A. A tensile characterization of 3D printed specimens was done for five thermoplastic materials - PLA, ABS, PC, PETG, and TPU -, and the anisotropic behaviour induced by the raster orientation was assessed (see Figure 1). It was concluded that PC, PETG and TPU had the most potential to integrate a 3D printed EAS, among the five tested. Furthermore, uniform honeycomb structures integrating these materials were tested to compression.

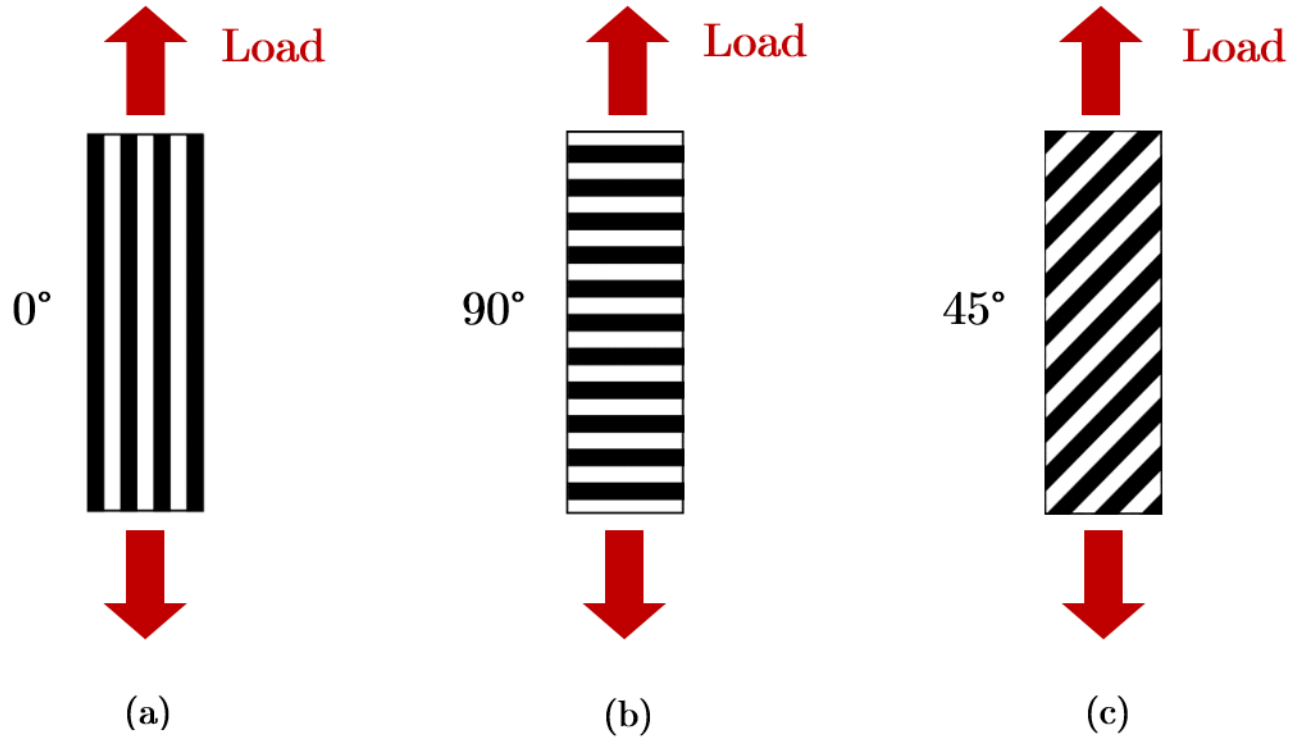

Figure 1: (a) Representative configuration of 0° specimen; (b) Representative configuration of 90° specimen; (c) Representative configuration of 45° specimen.

Tables 1-3 show the tensile mechanical properties, regarding raster orientation, determined in Paper A for PC, PETG and TPU. It is possible to conclude that PC is the stiffest and strongest among the three. On the other hand, PETG shows a much higher ductility than PC with an average strain to failure close to 200% when printed with 0° raster angle, and reasonable strength. TPU, an elastomer, has low stiffness and a very high strain to failure, being able to reach 4 times its initial size before rupture.

Table 1: Experimentally obtained mechanical properties of PETG specimens.

	Young's modulus (MPa)	Tensile strength	Strain to failure (%)
PETG 0°	1855 ± 71.3	45.7 ± 0.3	187.8 ± 31.7
PETG 45°	1653 ± 142.7	33 ± 1.4	3.8 ± 0.4
PETG 90°	1775 ± 255.9	33.9 ± 3.2	2.6 ± 0.3

Table 2: Experimentally obtained mechanical properties of PC specimens.

	Young's modulus (MPa)	Tensile strength	Strain to failure (%)
PC 0°	2300 ± 130.7	63.1 ± 0.8	86.2 ± 25.1
PC 45°	2309 ± 24.4	61.5 ± 1.2	11.8 ± 5.1
PC 90°	2230 ± 335.1	45.3 ± 5.2	2.7 ± 0.2

Table 3: Experimentally obtained mechanical properties of TPU specimens.

	Young's modulus (MPa)	Tensile strength	Strain to failure (%)
TPU 0°	96 ± 28.3	41.4 ± 1.8	420.1 ± 36.2
TPU 45°	121 ± 20.4	27.2 ± 2.4	348.5 ± 8.8
TPU 90°	104 ± 15.5	17.3 ± 0.5	186.1 ± 17.0

Furthermore, a two-part methacrylate adhesive - Plexus MA590 - was employed in the manufacturing process of the honeycomb multi-material structures. It is used for structural bonding of thermoplastics, among other materials. The mechanical properties of the adhesive are reported in Table 4

Table 4: Mechanical properties of Plexus MA590 adhesive.

	Young's modulus (MPa)	Tensile strength	Strain to failure (%)
Plexus MA590	482 - 827	13.8 - 17.2	> 130

2.2 Geometry

In this study, the honeycomb and spider web geometries were employed in the developed energy absorption structures. The functional grading of those aims to optimize their crashworthiness potential. The literature proposes multiple indicators used to quantify and assess the crashworthiness of a structure. Among those, the specific energy absorption (SEA) is a very relevant one. It quantifies the energy absorbed by a structure during the compression process, per unit of mass. SEA can be calculated by the following equation:

$$SEA = \frac{EA}{m} \tag{1}$$

Where EA corresponds to energy absorbed and m is the mass of the structure. EA can be obtained by integrating the area under the load-displacement curve originated from the compression test:

$$EA = \int_0^{\delta} F(x)\, dx \tag{2}$$

Where δ is the crushing displacement and $F(x)$ is the instant crushing load. Furthermore, peak crushing force (PCF) is also an indicator of great relevance. It corresponds to the highest value of $F(x)$ registered during the compression of a structure, and is directly correlated to the damage caused to a vehicle and its occupants in a collision, being one of the injury-based metrics. An excessive PCF translates into a high energy absorption rate and can lead to injuries and casualties during an impact, due to the high stress that is transmitted to the vehicle and its occupants [14]. It is then of great importance to have a reduced value of this parameter. The stiffness grading of an energy absorption structure allows a more constant energy absorption rate by decreasing the peak force generated by an impact, when compared to its uniform counterpart. Consequentially, the stress transmitted to other parts and occupants will also be reduced. The crash force efficiency (CFE) consists on the ratio between the peak crushing force and the mean crushing force (MCF).

$$CFE = \frac{PCF}{MCF} \tag{3}$$

Where MCF can be obtained by the following equation:

$$MCF = \frac{EA}{\delta} \tag{4}$$

The protection is enhanced for a high values of CFE. Ideally, CFE is equal to 1.

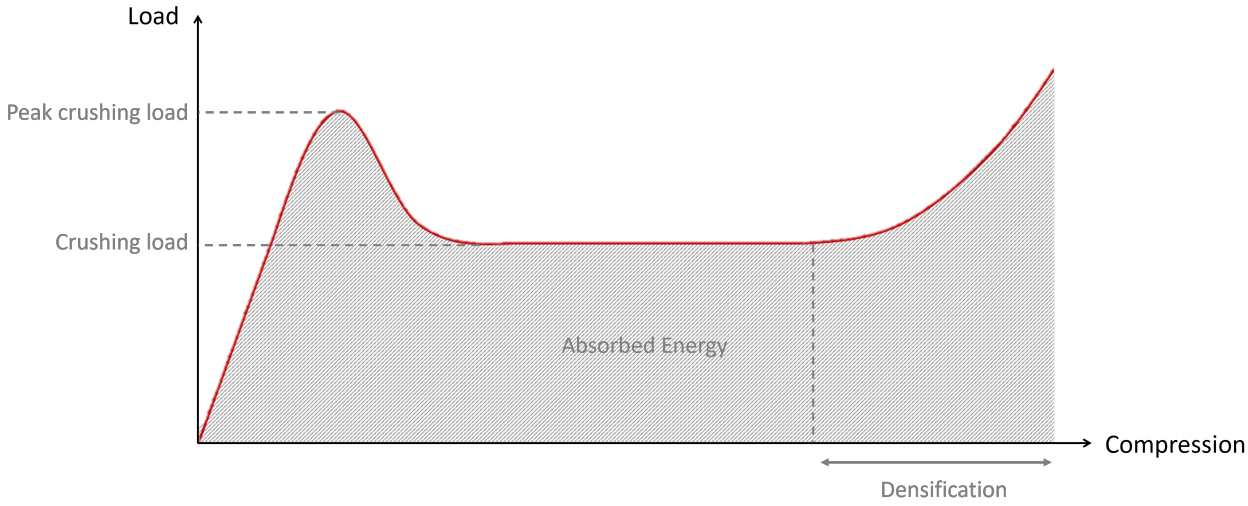

Figure 2: Representative load-displacement curve of a compression test.

As mentioned, honeycomb structures are highly efficient when it comes to energy absorption, while maintaining a good ratio between energy absorption values and structural mass (specific energy absorption). Hence, these are commonly employed in applications where impact loads need to be dissipated.

An uniform honeycomb structure, characterized to quasi-static compression in Paper A, was employed as the reference for comparison and assessment of the stiffness grading influence on the crashworthiness of the developed structures. Figure 3 shows its dimensions.

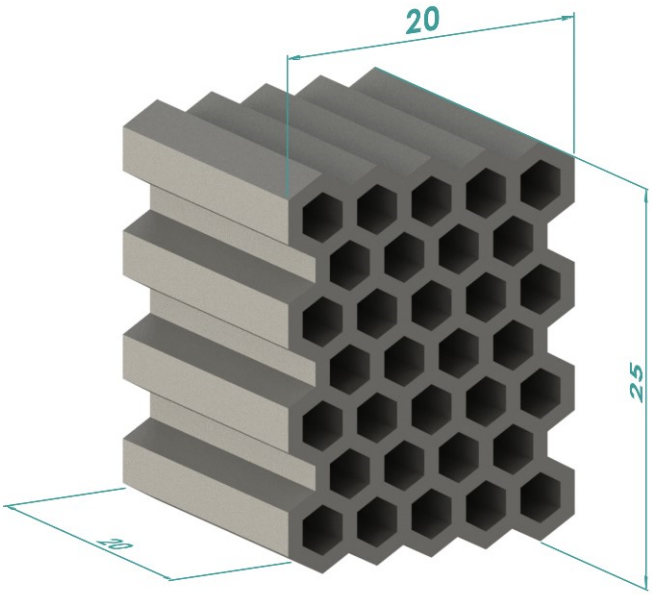

Figure 3: Dimensions of uniform honeycomb reference structure (mm).

Regarding the honeycomb multi-material EAS, its stiffness grading was achieved by

integrating multiple materials in the same structure. This way, it is possible to vary structural properties along the length of the EAS. Three materials, with different stiffness values, were integrated in the honeycomb EAS: PC, PETG and TPU. The materials with the highest and lowest stiffness, PC and TPU, respectively, were integrated on opposite ends of the structure, with PETG integrating the middle part of the EAS since its stiffness value falls between the ones of those. Hence, a sequential order of stiffness was achieved. The dimensions and material configuration of the multi-material honeycomb energy absorption structures are represented in Figure 4. These were printed in two different sizes, in order to evaluate its effect on energy absorption capabilities.

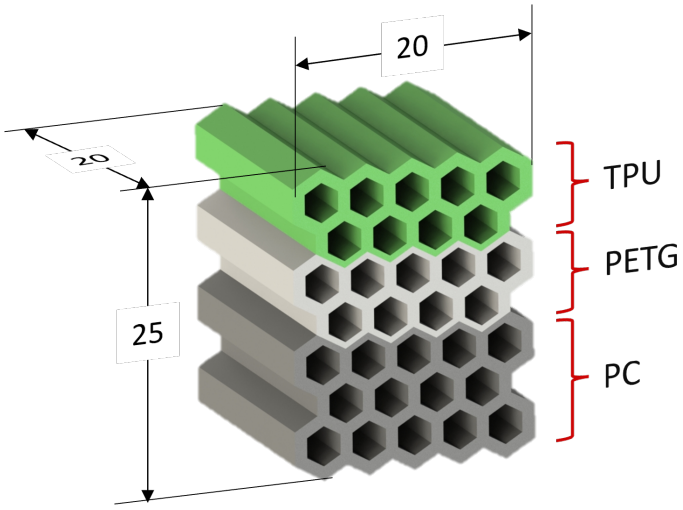

Figure 4: Dimensions (mm) and material configuration of honeycomb EAS.

The spider web geometry, unlike the honeycomb, has not been extensively studied as a potential energy absorption structure. Contrary to the developed honeycomb structure, the spider web inspired graded EAS designed for this study is a single material structure that obtains its stiffness grading through the variation of the structural density. As we progress deeper along the structure, the number of spiral threads increases, and so does its stiffness (see Figure 5). The spider web graded EAS was printed in PC, PETG and TPU.

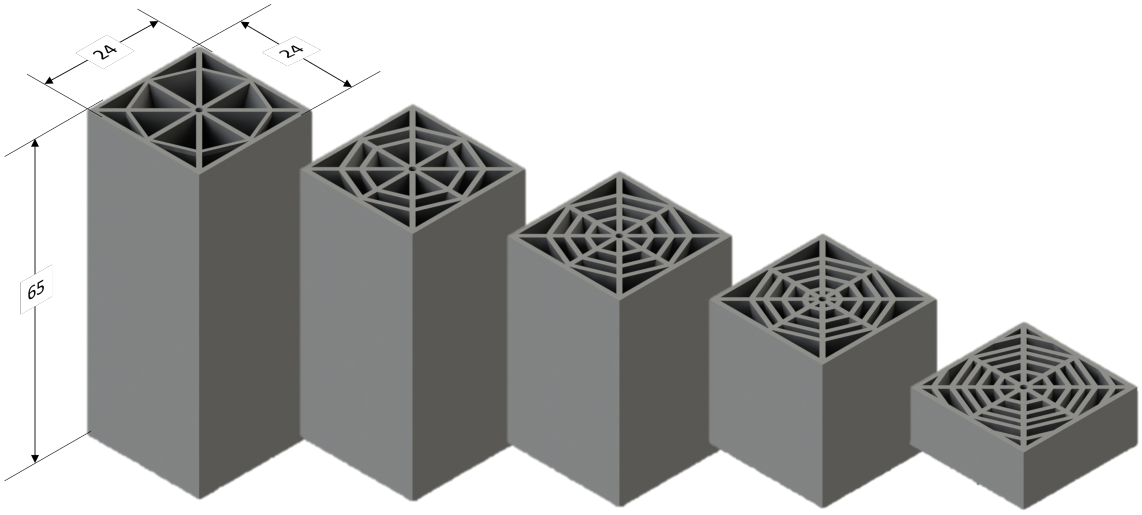

Figure 5: Dimensions (mm) and cross-section views of the spider web inspired EAS.

2.3 3D printing

The multi-material honeycomb structures were made by adhesively bonding three distinct 3D printed honeycomb structures, one of each material. These were designed to fit each other and originate a final part with an uniform geometry, only varying in the material properties. The volume fraction of each material's part composed roughly one third of the total volume of the honeycomb EAS.

These structures were 3D printed, separately, via fused deposition modelling, in a Prusa i3 MK3S+ (Prusa Research, Prague, Czech Republic). The parts for testing were printed at a reduced speed and with a layer height of 0.05 mm, with exception of the first layer that had a height of 0.2 mm to grant improved adhesion and tolerance, by mitigating possible slight errors in leveling. To minimize the occurrence of structural defects during printing and enhance the mechanical properties of the structures, regarding the direction of the compression loads, these were printed flat on the print bed. This build direction ensures layer continuity within the honeycomb cross-section and thus prevents an excessive degree of brittle fracture of the structures when compressed, as seen in Paper A.

Before bonding the distinct parts to create the final honeycomb multi-material EAS, the bonding surfaces were subjected to a plasma treatment to increase their surface energy and facilitate the bonding of the adhesive. The adhesive utilized for bonding the structures was Plexus MA590, a two-part methacrylate adhesive developed for structural bonding of thermoplastic, metal, and composite assemblies. The bonded structures were then left to cure for at least 24 hours, before being tested.

Similarly to the honeycomb structures, the spider web graded structures were printed via fused deposition modelling, in the same Prusa i3 MK3S+ equipment, with a first layer height of 0.2 mm and 0.05 mm for the subsequent layers. These structures were printed

in PC, PET and TPU. Figure 6 shows their build orientation.

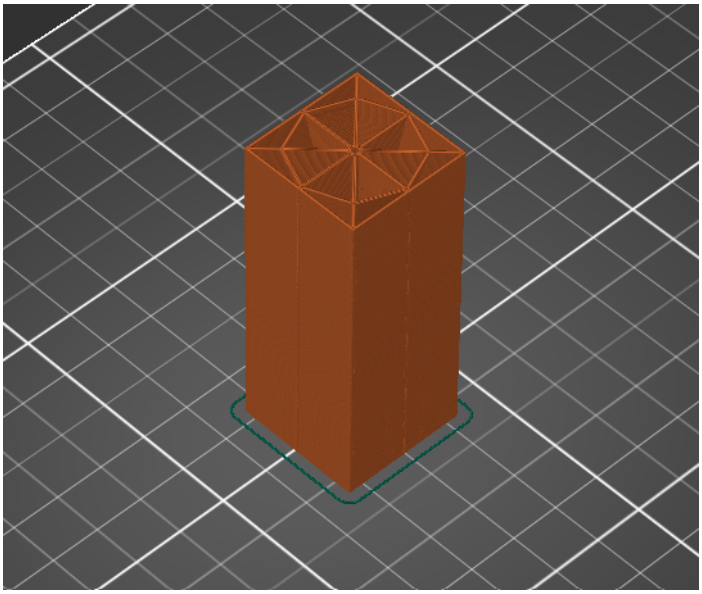

Figure 6: Build orientation of spider web graded structures.

The printing temperatures set for each material are shown in Table 5.

Table 5: Printing temperatures for each material.

Material	Printing temperature (°C)	
	Print bed	Nozzle
ABS	110	260
PC	115	280
PETG	90	255
PLA	60	220
TPU	50	245

2.4 Structure testing

In order to assess the collapse behaviour and crashworthiness potential and the effect of the developed structures, these were tested to compression under different loading regimes: quasi-static compression, high-rate compression and impact.

The quasi-static compression tests were performed in Instron 3367 universal testing machine (Instron, Norwood, MA, USA) equipped with a 30 kN load cell, at a constant cross-head displacement rate of 1 mm/min. The compression tests were run until the load value reached 30 kN, the load cell limit.

The high-rate compression tests were performed in a Instron 8801 servo-hydraulic universal testing machine equipped with a 100 kN load cell, at a rate of 0.1 m/min. The limit displacement set for the movable plate allowed the running of the tests until full densification of the structures.

The impact tests were conducted in a drop-weight machine. The velocity of impact was set at 3 m/s. The set mass for the impactor was set, according to the structured being testes. While for the uniform honeycomb structures and its multi-material counterparts a 9.5 kg mass was employed, translating in an impact energy of 42.98 J, for the testing of the large honeycomb and spider web graded structures a mass of 27.51 kg was used, leading up to impact energy of 122.9 J.

3 Results and discussion

3.1 Quasi-static compression

As a result of the stiffness grading, a staggered compression was observed during the quasi-static compression of both honeycomb and spider web graded structures.

For the honeycomb multi-material structures, 3 distinct compression stages can be identified, corresponding to the compression of each material, as Figures 7 shows. TPU, being the material with the lowest stiffness, gets compressed first. PETG then starts to deform once the TPU portion of the structure gets compacted. Finally, PC starts to undergo plastic deformation once the above structures densify, and there is overall compaction of the structure.

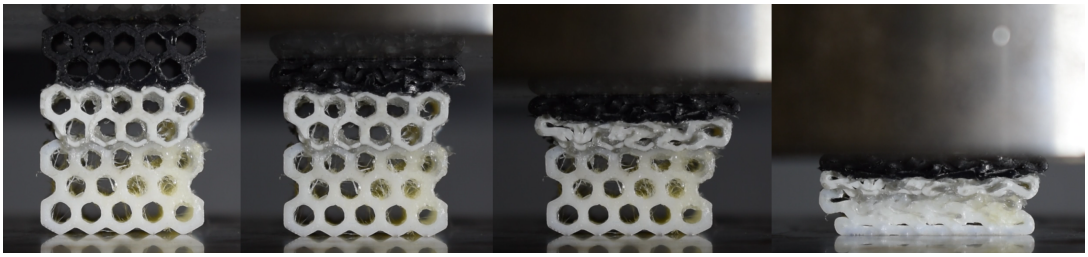

Figure 7: Staggered deformation of multi-material honeycomb structure under quasi-static compression loading.

This staggered behaviour is clearly shown by the load-displacement data obtained from the compression tests, where three distinct compression stages can be identified, as can be seen in Figure 8. In each stage there is a linear elastic deformation phase, followed by a plateau that corresponds to plastic deformation associated to the crushing of the structure, and the final densification phase, when there is an increase in the load values and the onset elastic deformation of the subsequent material starts. Since there is an

independent collapse of each part of the honeycomb multi-material structure, the corresponding crushing load (plateau region) of each corresponds to the same of its uniform counterpart. Furthermore, because the collapsing of each part starts after the densification onset of the adjacent one, the overall densification of the structure is delayed, when comparing to the uniform counterparts.

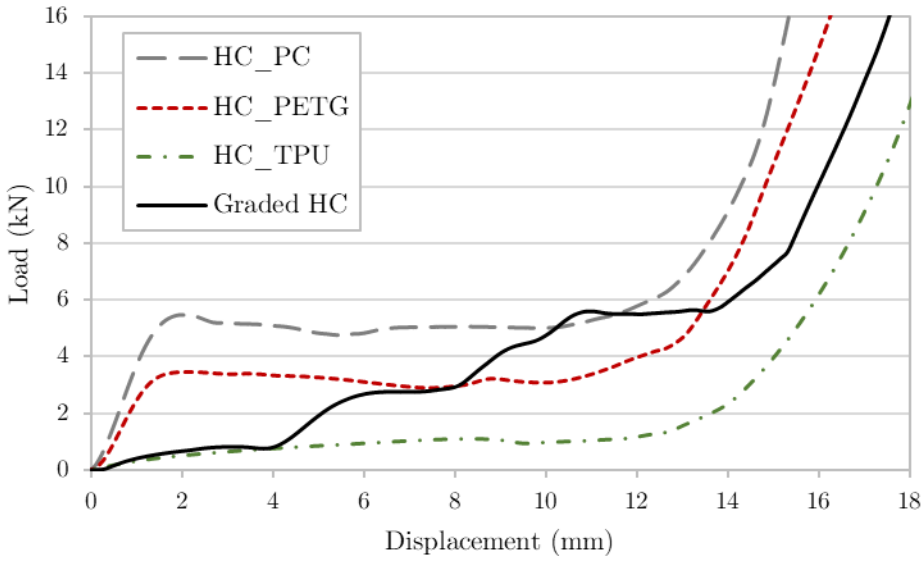

Figure 8: Load-displacement curves obtained from quasi-static compression of uniform and multi-material honeycomb structures.

Regarding the spider web graded structures, the collapsing modes under quasi-static compression differed, regarding the employed material. However, a staggered compression was observed for all structures, due to the stiffness grading feature. Hence, the structures started to collapse on the lowest stiffness region, with a progressive deformation of the adjacent, higher stiffness ones. Figure 9 shows different stages of the quasi-static compression of the spider web graded structures.

It is possible to see that, at the beginning of the compression, a patterned deformation appears all over the specimens, being more noticeable in the regions where the stiffness is lower, near the top. These wave patterns then translate into a collapse by folding, that start from the top and propagate through the structure as it gets compressed. Moreover, it was possible to observe, in PC (Figure 9a) and PETG (Figure 9b) structures, the opening of cracks along the the layers' interface. These result from the tensile stress that arise from the localized bending in the folds. Close to densification of these structures, it was also possible to see some vertical crack propagation on the interface between the outside walls and then inner spider web structure, due to the stresses generated by the buckling of the outside and inner vertical walls.

On the other hand, no fracture was observed during the quasi-static compression of

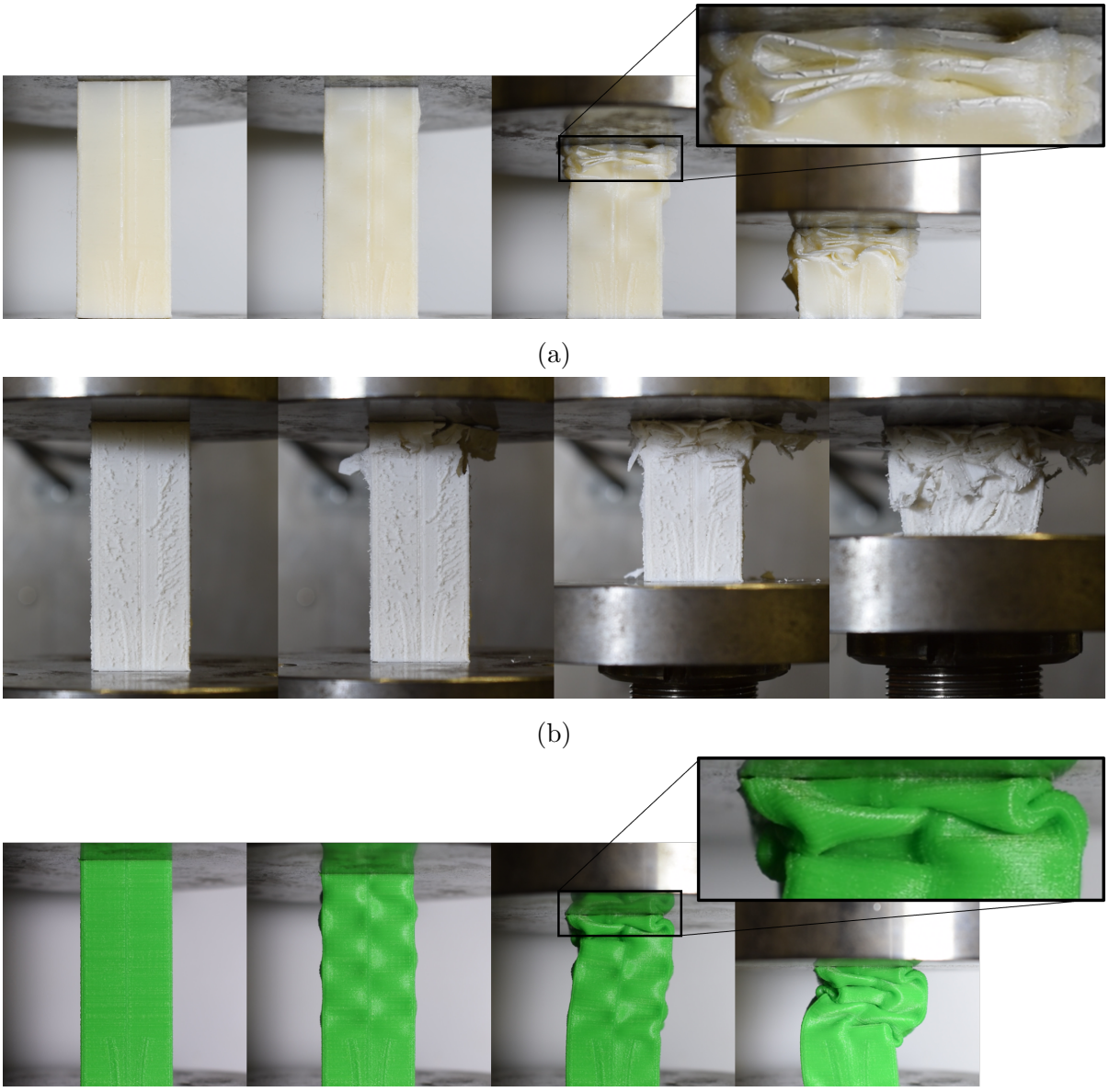

Figure 9: Collapse behaviour of different material spider web graded structures under quasi-static compression: (a) PC, (b) PETG, (c) TPU.

TPU spider web structures. Due to its elastic nature, these are able to sustain a considerable amount of strain without deforming plastically. Hence, these recovered most of their initial shape when decompressed. The buckling of TPU structures was also observed, being more noticeable when the higher stiffness regions started to get compressed. This comes as consequence of the viscoelastic behaviour of TPU, which makes it able to adapt and dissipate the stresses.

Figure 10 shows a comparison between the load-displacement curves obtained from the quasi-static compression of spider web graded structures. A initial peak can be observed for PC and PETG curves, that corresponds to the onset of plastic deformation and conse-

quent folding, after which an increasing staggered trend can be seen. This results from the successive collapsing of higher stiffness regions, that require higher loads to be deformed. The staggered compression is less noticeable than on the multi-material honeycomb, since there is a more gradual stiffness grading with five different stiffness regions. Moreover, the densification of a region and the onset of deformation of the adjacent, higher stiffness one, overlap. On the other hand, due to low force necessary to deform the TPU region, this graded behaviour is not as noticeable. However, an increasing trend is also observed.

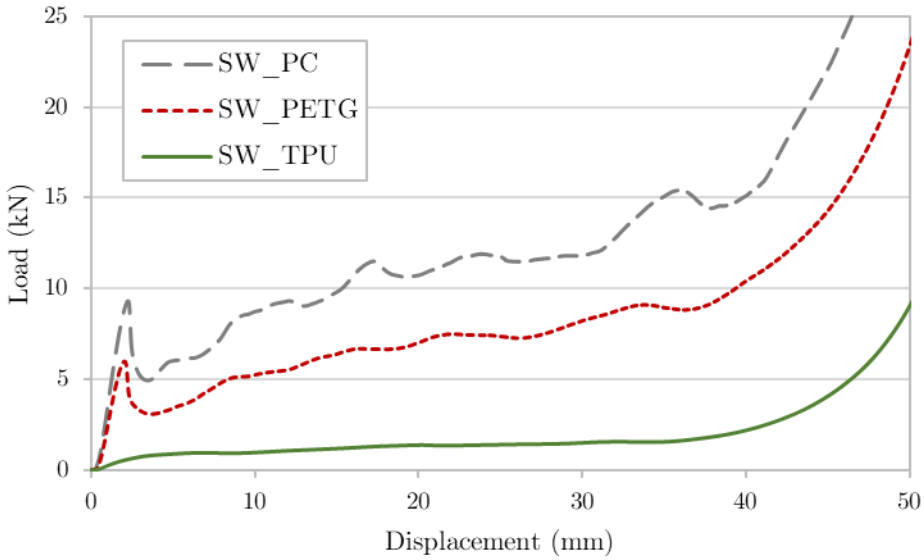

Figure 10: Load-displacement curves obtained from quasi-static compression of graded spider web structures.

3.2 High-rate compression

Regarding the honeycomb, multi-material structures, the same staggered behaviour, with three independent compression stages was observed (see Figure 11). However, because of the higher strain at which the tests were conducted, the strain hardening effect was noticeable. This led to higher loads being needed to plastically deform the structures, when comparing to quasi-static loading. Furthermore, PETG's brittle behaviour was enhanced. Along with plastic deformation, brittle fracture was observed in the PETG part of the multi-material honeycomb. Figure 12 shows the load-displacement curved obtained from the high rate compression of the uniform and multi-material honeycomb structures. As in the quasi-static regime, the grading feature of the multi-material honeycomb delayed the onset of densification.

PETG showed an excessively brittle behaviour under these conditions. While the PC and TPU structure showed an initial patterned deformation, with subsequent collapse by folding, the PETG structure showed a progressive collapse promoted by brittle fracture

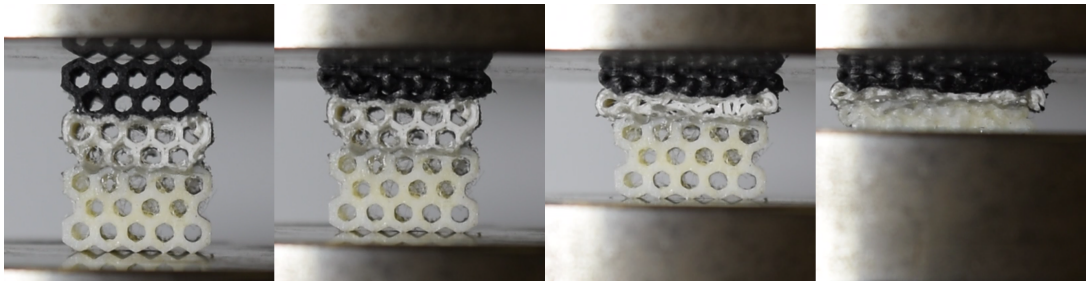

Figure 11: Staggered deformation of multi-material honeycomb structure under high-rate compression loading.

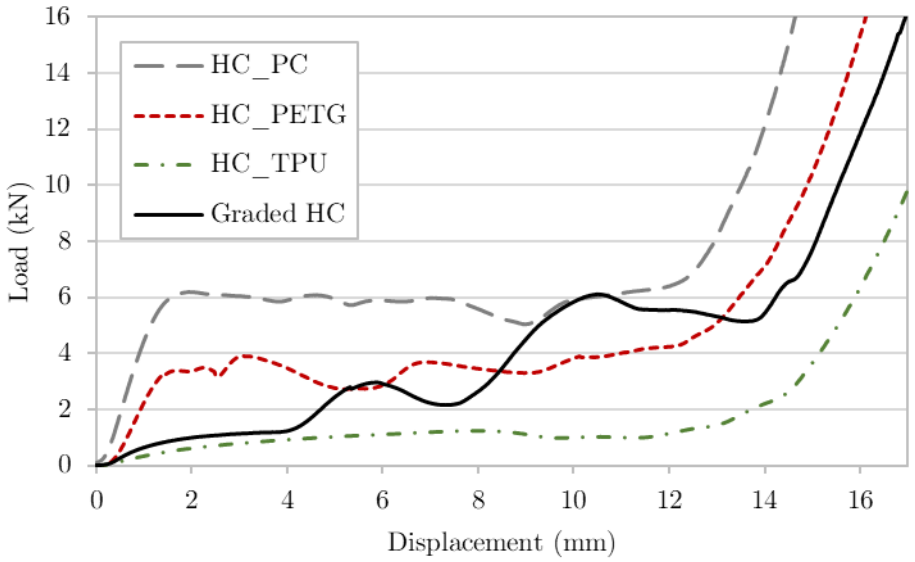

Figure 12: Load-displacement curves obtained from high-rate compression of uniform and multi-material honeycomb structures.

with the release of splinters and chunks of the structure (see Figure 14). As in the quasi-static tests, fracture promoted by bending was observed in the PC structure. Furthermore, buckling of the TPU structure was also observed.

Figure 13 shows the load-displacement curves obtained from the high-rate compression tests of the spider web graded structures.

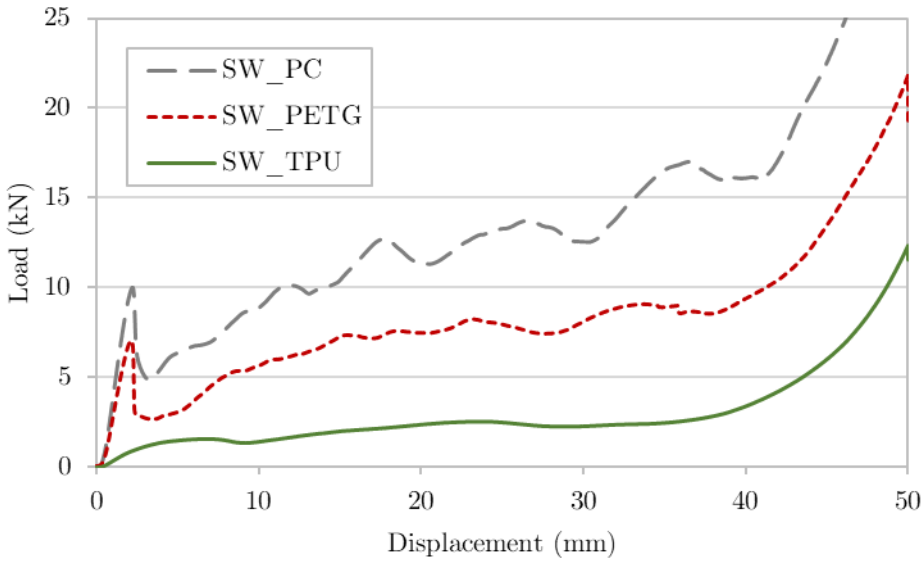

Figure 13: Load-displacement curves obtained from high-rate compression of graded spider web structures.

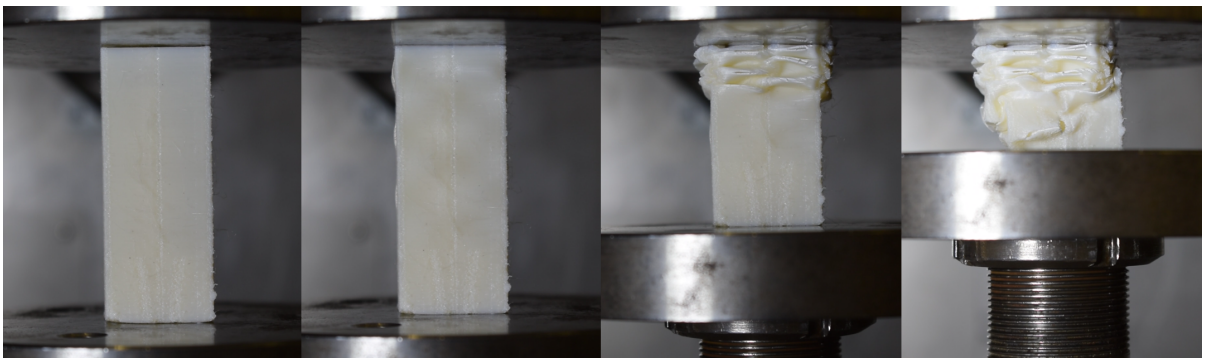

(a)

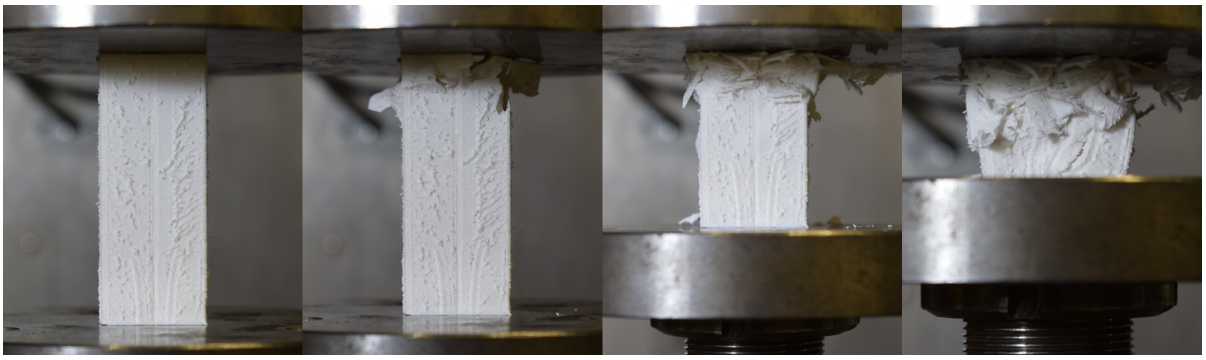

(b)

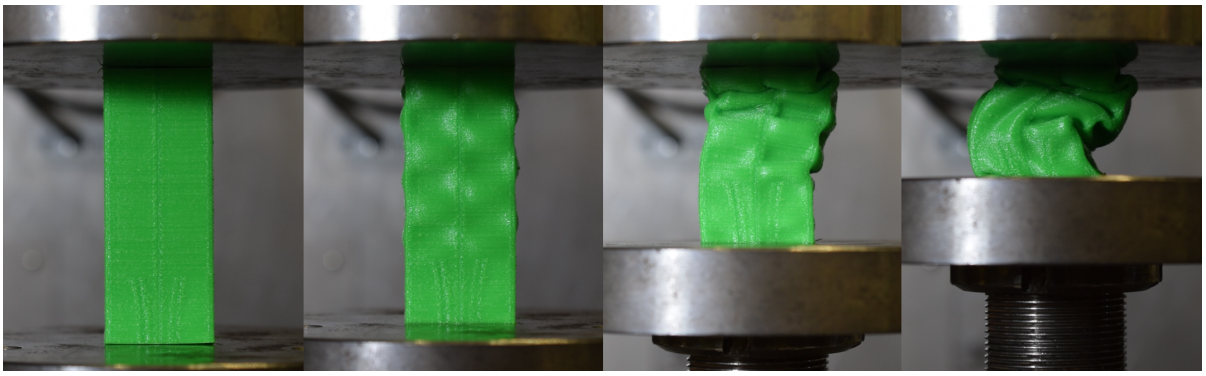

(c)

Figure 14: Collapse behaviour of different material spider web graded structures under high-rate compression: (a) PC, (b) PETG, (c) TPU.

3.3 Impact

The developed structures were submitted to impact tests to assess their behaviour under close to real-world conditions and crashworthiness potential.

Figure 15 shows the evolution of the load value with the time during impact, for the uniform and multi-material honeycomb structures. For the TPU and PETG uniform structures, it is possible to observe a sudden load increase in the final stage of the compression, that corresponds to the densification of those materials. Nevertheless, the peak force registered for the impact test of the TPU structure was much lower than for PETG. Due to the brittle collapse of the PETG structure, the energy of impact absorbed by this material in a initial phase was minimal. Thus, most of the impact energy was absorbed after full compaction, leading to an accentuated peak force. Concerning PC, plastic deformation of the structure along with brittle fracture was observed. The energy of impact was dissipated before densification.

The collapse behaviour of the multi-material structure is seen in Figure 16. A combination of the failure modes described before was observed. After an initial deformation of the TPU portion of the structure, brittle fracture occurs on the central PETG block, which shattered and released splinters and chunks of material, leading to the decrease in load at roughly 2 ms into the impact (see Figure 16). The brittle behaviour of PETG made so that its contribution for impact absorption was minimal. Finally, plastic deformation, along with brittle fracture, is observed in PC bottom part.

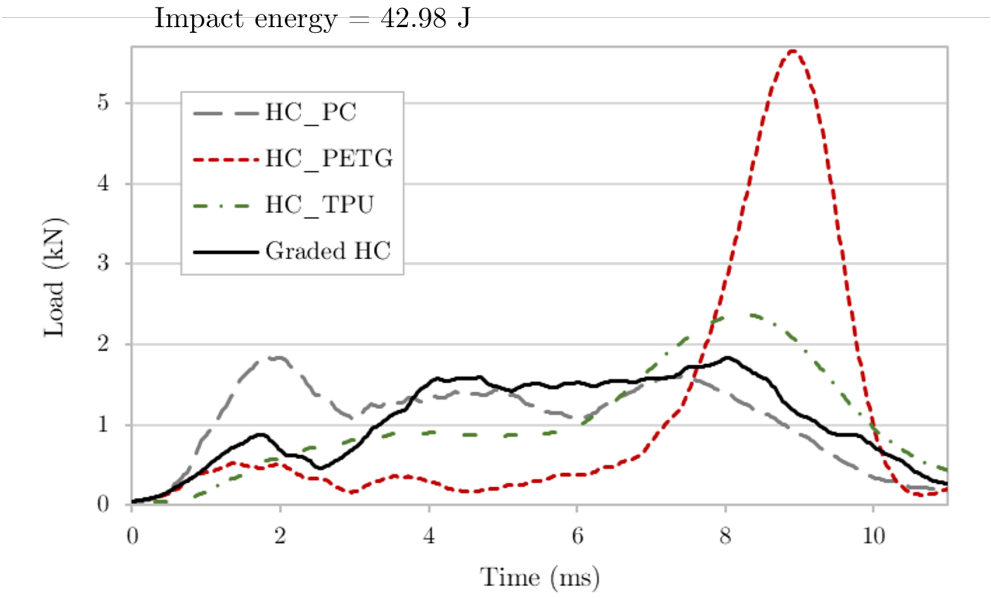

Figure 15: Evolution of load values during impact of uniform and multi-material honeycomb structures.

The spider web graded structure specimens, after impact, are shown in Figure 17. For

Figure 16: Collapse behaviour of multi-material honeycomb structure under impact.

PC, a collapse by folding along with fracture along the layers interface in the fold was observed, similarly to when submitted to quasi-static and high-rate loading. On the other hand, brittle fracture was observed during the collapse of the PETG structure. The TPU structure collapsed by folding (see Figure 18) and recovered to its initial form after the impact, suffering almost no plastic deformation.

Figure 17: Spider web graded structures after impact: PC (left), PETG (middle), TPU (right).

Due to its higher stiffness, the energy absorption rate was the highest when employing the PC structure, as it is possible to infer by the earlier decrease in the load value during the impact, shown in Figure 19. This is also corroborated by the lower decrease in height suffered by that structure, when compared to the PETG counterpart. PETG and TPU structures were able to dissipate the energy of impact more gradually. It is worth noting that the longer the displacement, i.e. the stroke, the lower the energy absorption rate is. This translates into a lower stress being transmitted to the parts being protected by the EAS [19].

Figure 18: Collapse by folding of TPU spider web graded structure during impact.

Furthermore, due to the stiffness grading of the structures, an increasing trend of the load value can be seen, as the impactor compresses each consecutive higher stiffness part of the structures. This trend is more noticeable the higher the stiffness of the material is.

It is worth noting that since the entirety of the impact energy was transmitted to the specimens during the performed impact tests, the absorbed energy does not depend on the crushing displacement. Hence, only load based metrics were calculated to evaluate the performance of the tested structures under this kind of loading.

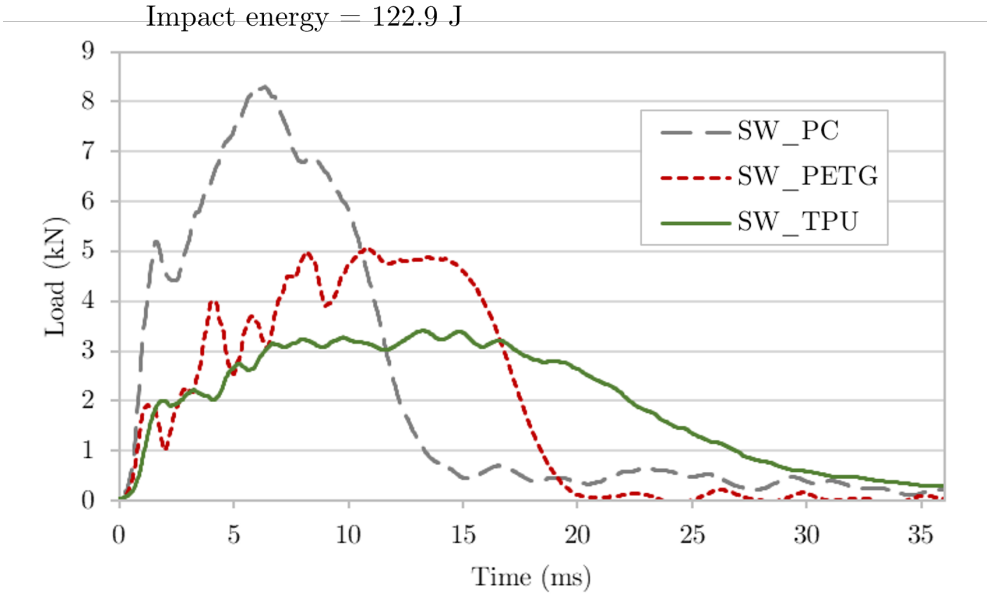

Figure 19: Evolution of load values during impact of spider web graded structures.

3.4 Influence of stiffness grading

Figures 20-23 show a comparison between the average values of SEA, PCF, MCF and CFE obtained for the uniform and multi-material honeycomb structures, under different loading regimes. The multi-material structure showed to have a higher specific energy absorption than the PETG and TPU counterparts. This comes as result of the integration of PC and the delayed onset of densification caused by the grading feature.

Due to the integration of PC on the multi-material structure, the average peak force under quasi-static and high-rate loading was identical to that obtained for the PC uniform structure. Although the efficiency of the multi-material structure was lower than the remaining under quasi-static and high-rate compression, it showed the lowest decrease among the tested structures when passing from these loading regimes to impact conditions, proving to be as efficient as the PC counterpart. However, its performance was hampered by the brittle behaviour shown by PETG under high strain rate. It could be observed that the peak force measured during the compression of the structures only depended on the presence of the stiffer material, and not on its proportion. On the other hand, the mean crushing force can effectively be decreased by the integration of lower stiffness materials, allowing a more efficient energy absorption under impact by avoiding a excessively high initial peak resulting form the initial impact.

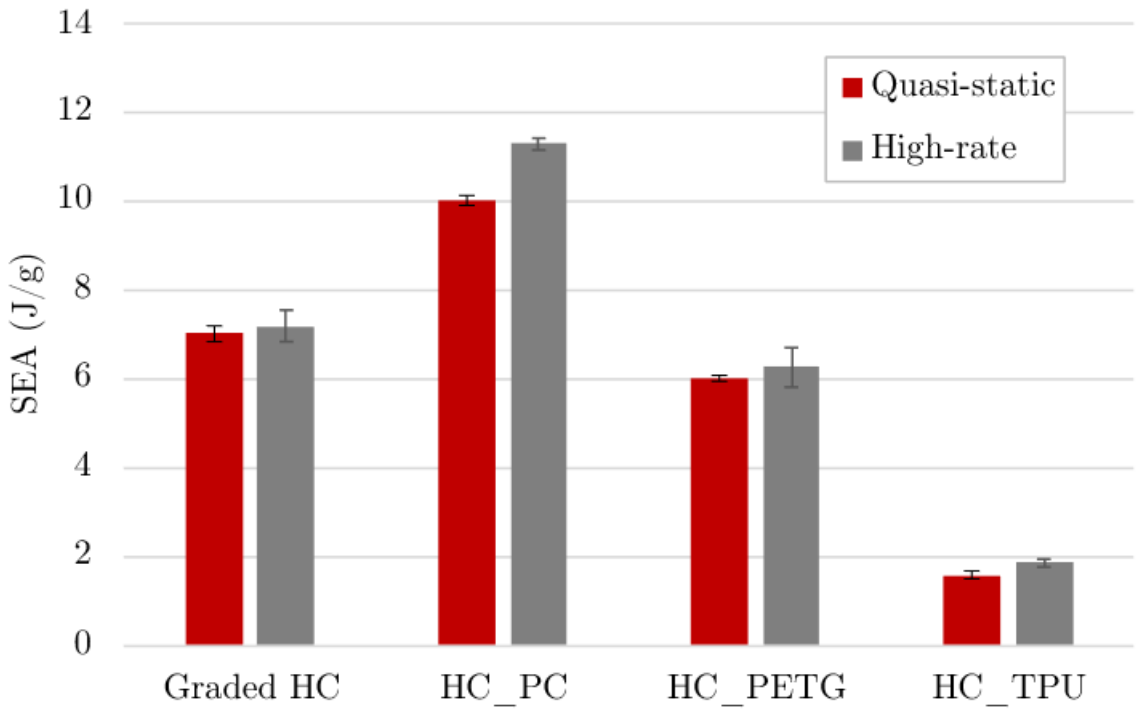

Figure 20: Obtained SEA values for uniform and multi-material honeycomb structures.

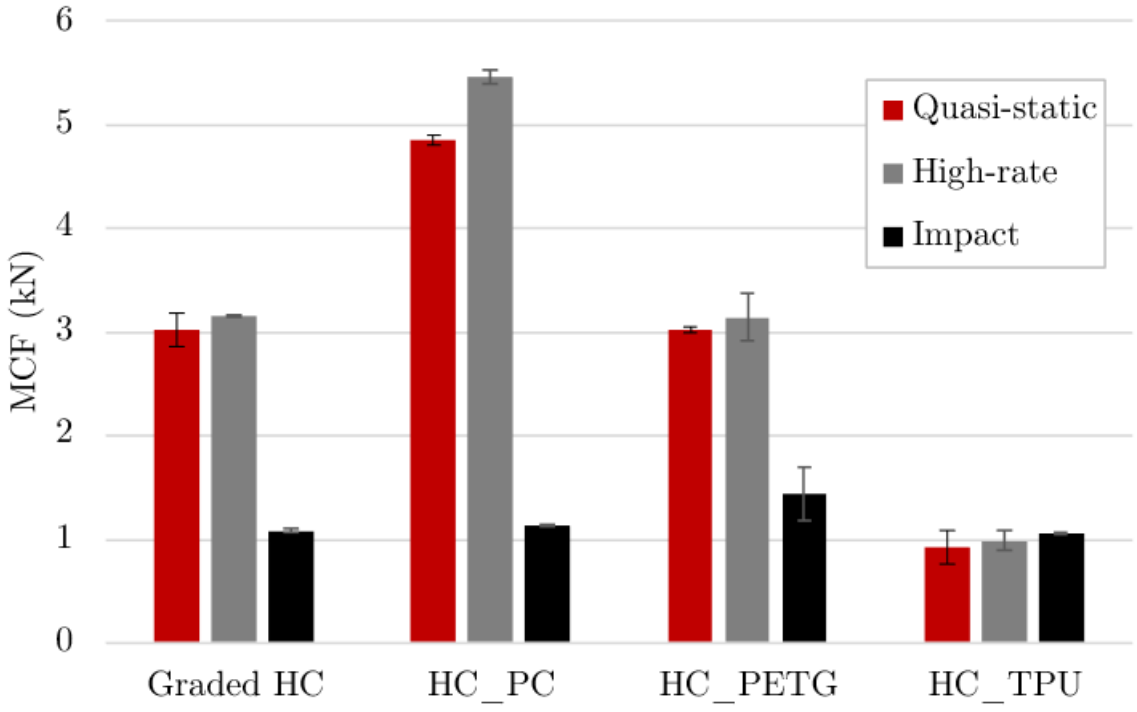

Figure 21: Obtained MCF values for uniform and multi-material honeycomb structures.

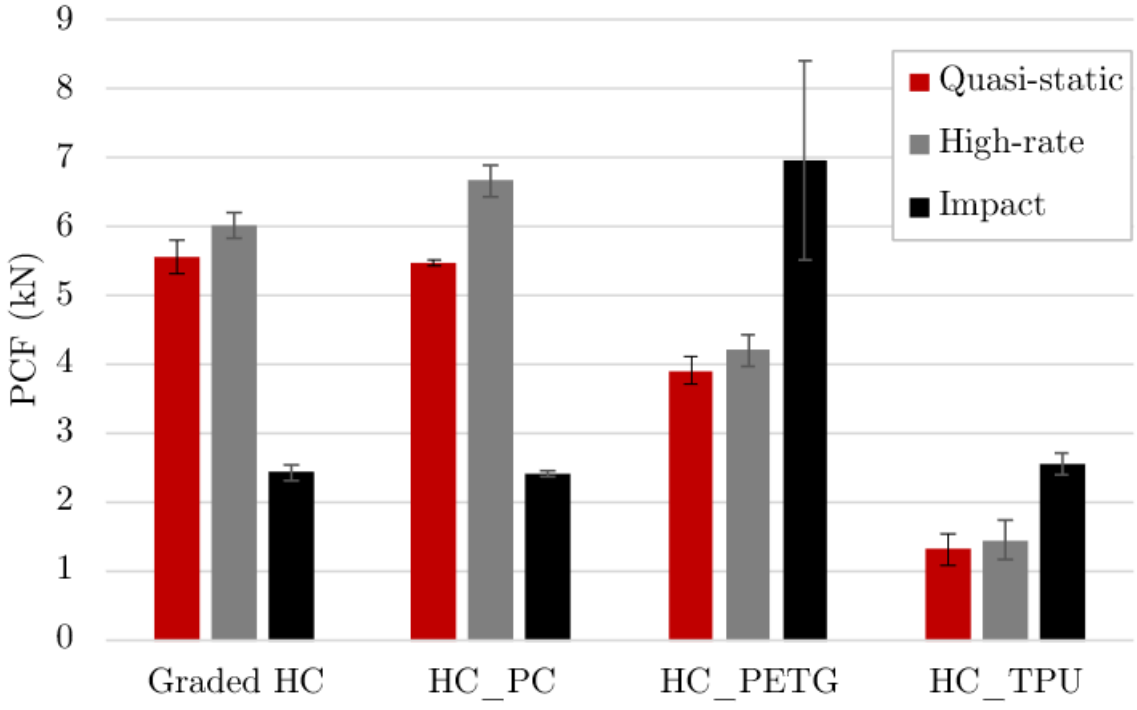

Figure 22: Obtained PCF values for uniform and multi-material honeycomb structures.

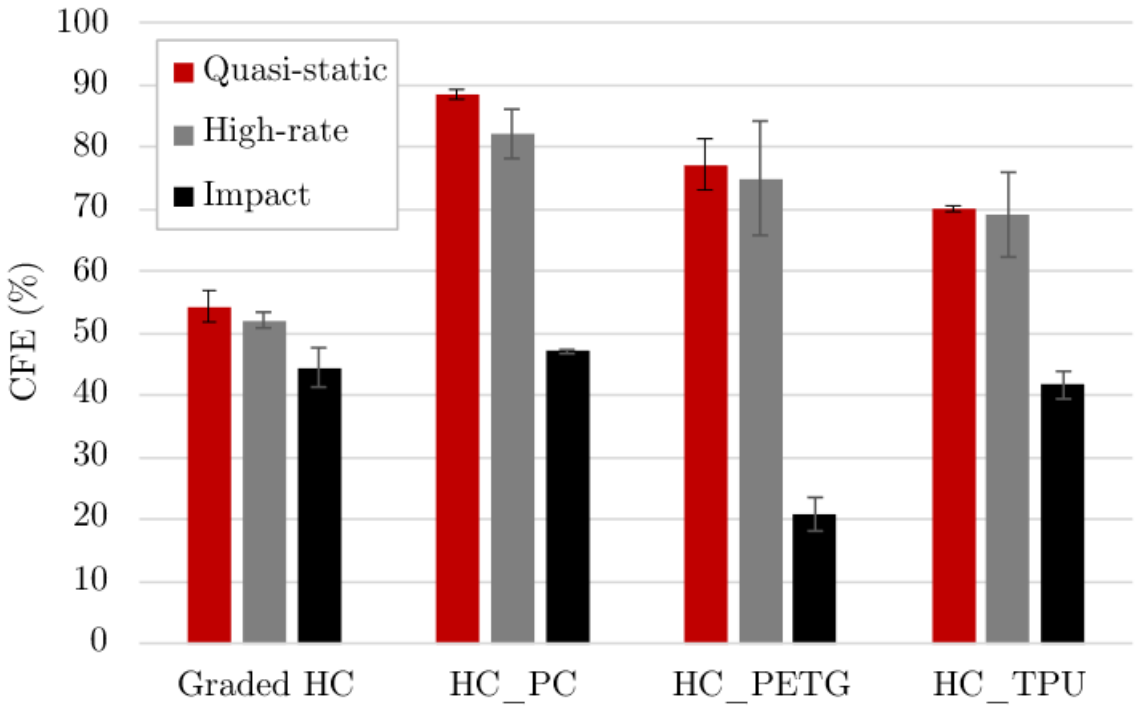

Figure 23: Obtained CFE values for uniform and multi-material honeycomb structures.

3.5 Size effect

To evaluate the influence of size in energy absorption capabilities a large honeycomb multi-material structure, with the same material configuration of the tested one and roughly three times its height was developed (see Figure 24). Due to its height, stability issues arose when testing it to impact, leading to buckling and further detachment of the constituent parts of the structure. However, quasi-static and high-rate compression tests were able to be performed. Hence the size effect could still be evaluated under these two loading regimes.

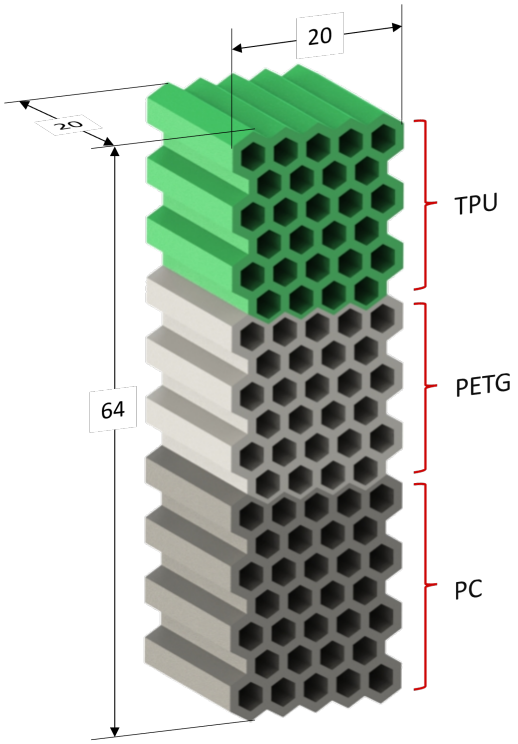

Figure 24: Dimensions (mm) of large honeycomb multi-material structure.

Figure 25 shows the curves obtained for the compression tests performed on the large honeycomb structure. As expected, it follows a staggered compression, similarly to the smaller structure. Due to strain hardening, higher load values are registered for the high-rate compression.

As expected, due the higher compression stroke, more energy was absorbed by the bigger size strcuture. However, as can be seen in Figures 26-29, the difference between the values of SEA, MCF, PCF and CFE obtained for each structure is negligible. Hence, the energy absorption capacity of a structure can be predicted by testing a smaller counterpart with the same configuration, for both loading regimes. Furthermore, it is possible to observe that the crushing plateaus, that correspond to the plastic deformation of each part of the structures, occur at the same load level for each material, in both structures. The values at which the yielding and consequent plastic deformation of a structure occurs

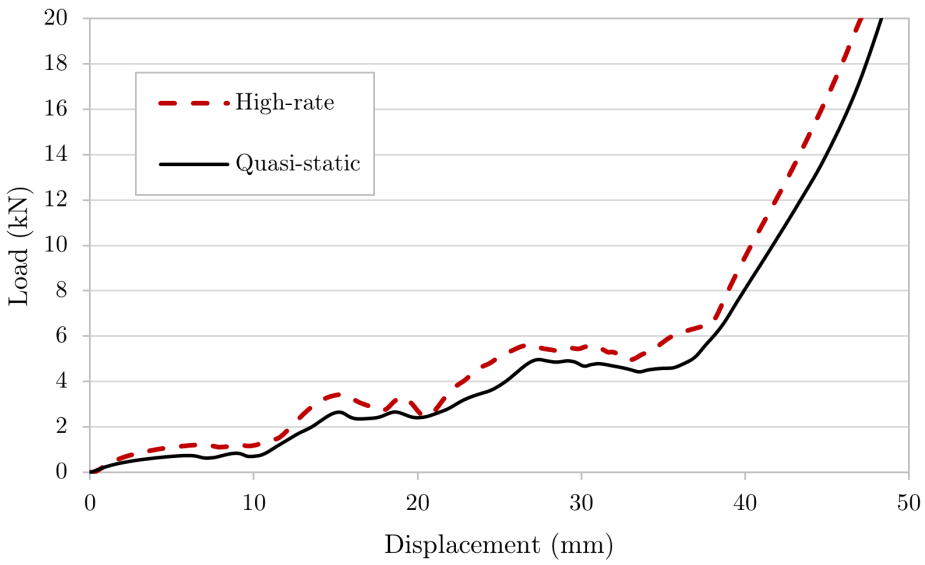

Figure 25: Load-displacement curves obtained from quasi-static and high-rate compression of large honeycomb multi-material structure.

depends on its geometry and material. Hence, it is also possible to obtain the crushing force efficiency of a structure by testing a smaller counterpart.

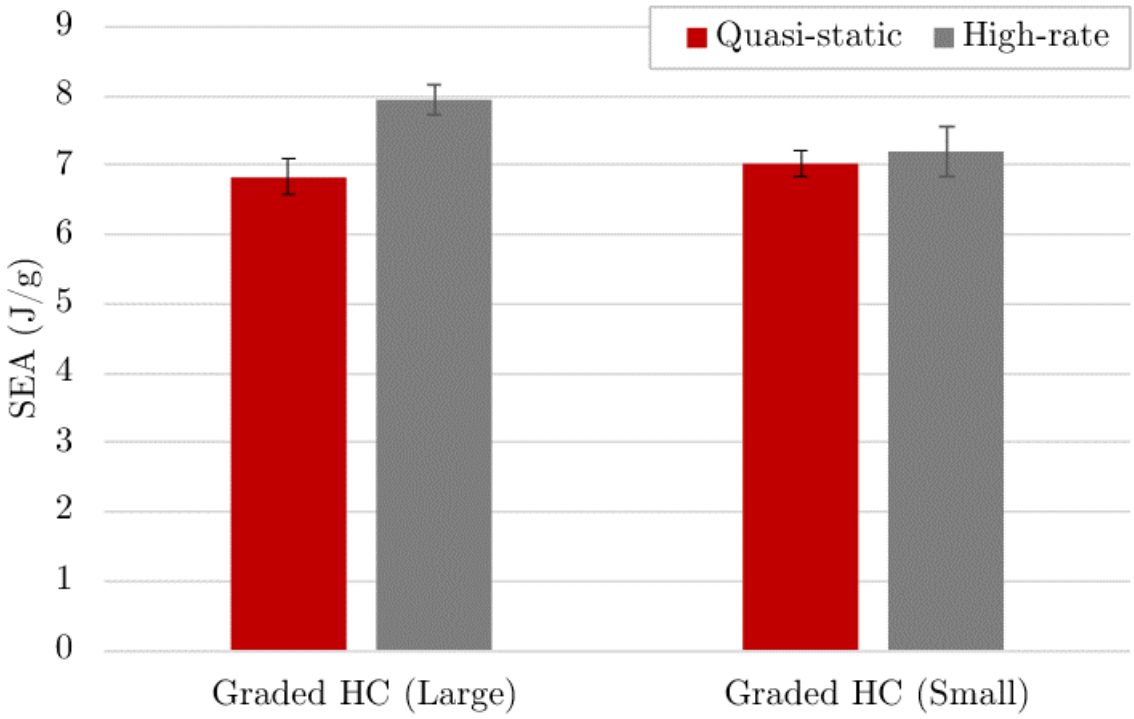

Figure 26: Obtained SEA values for two size multi-material honeycomb structures.

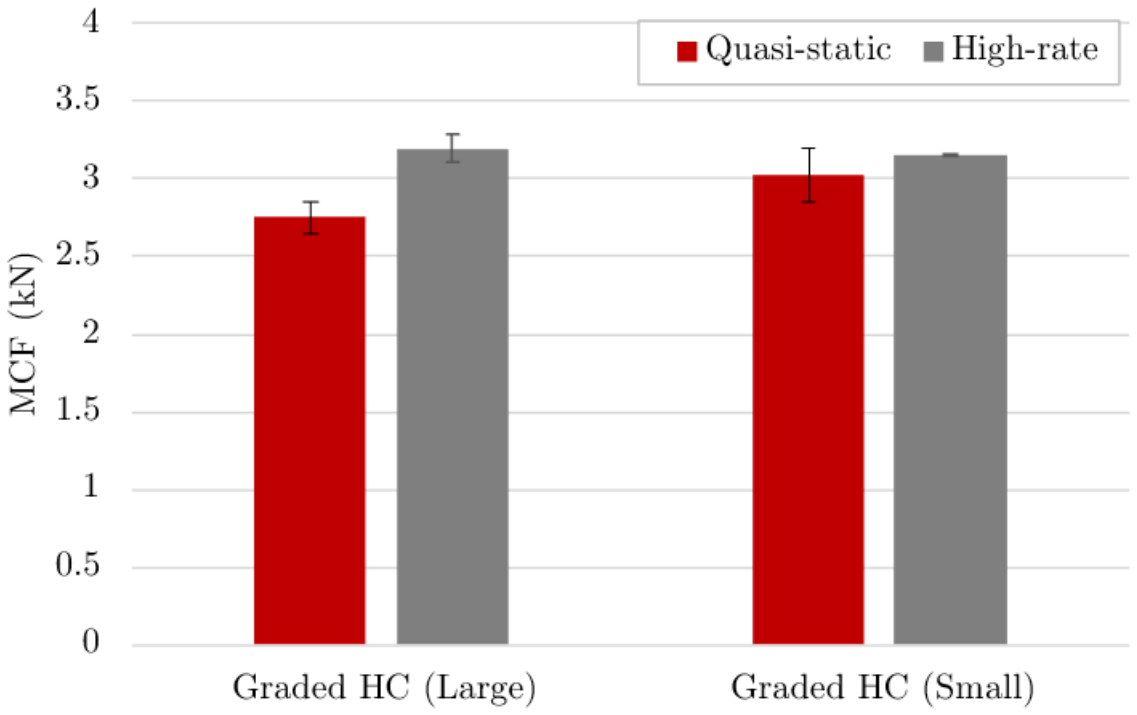

Figure 27: Obtained MCF values for two size multi-material honeycomb structures.

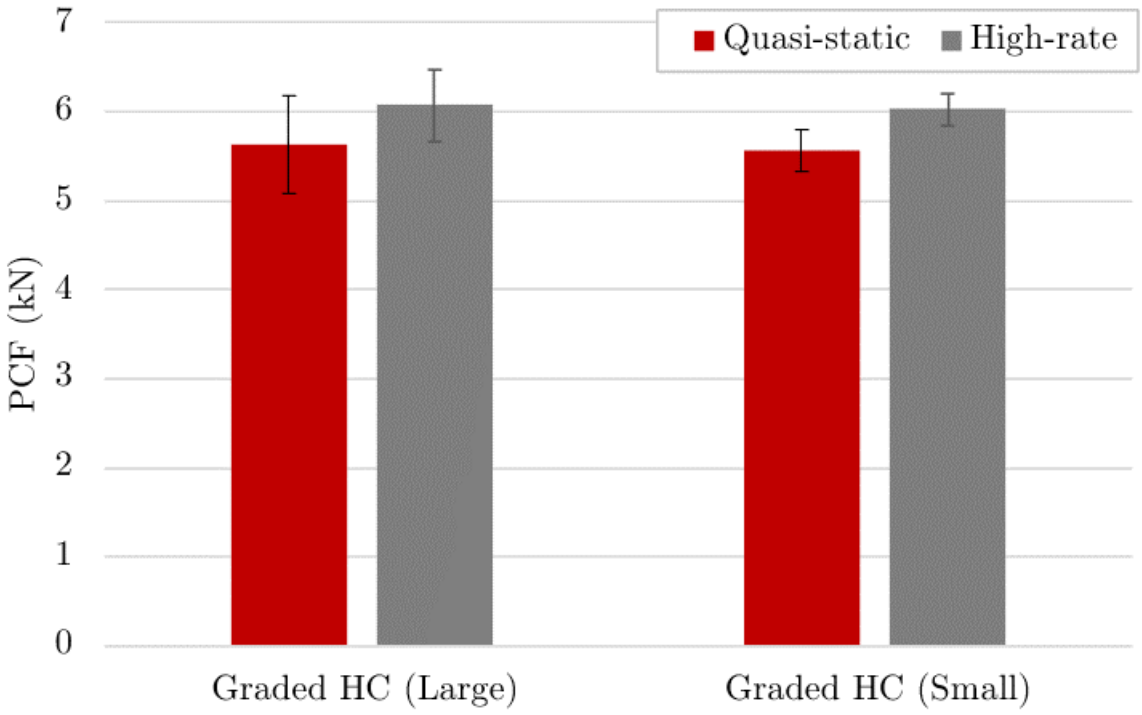

Figure 28: Obtained PCF values for two size multi-material honeycomb structures.

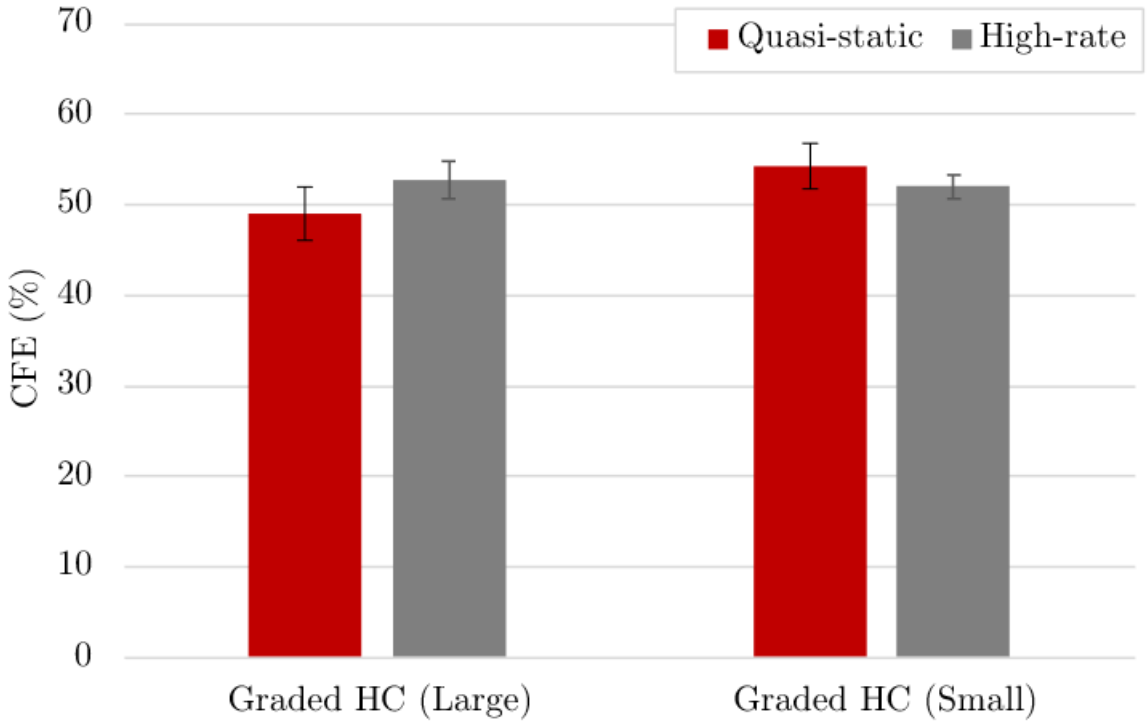

Figure 29: Obtained CFE values for two size multi-material honeycomb structures.

3.6 Comparison of EAS concepts

Unlike the spider web graded structures, the large honeycomb multi-material structure was not able to sustain impact without disintegrating, making it impossible to make a direct comparison between the two under this mode of loading. Figures 30-33 show a comparison of the crashworthiness indexes obtained for both structures, under quasi-static and high-rate compression.

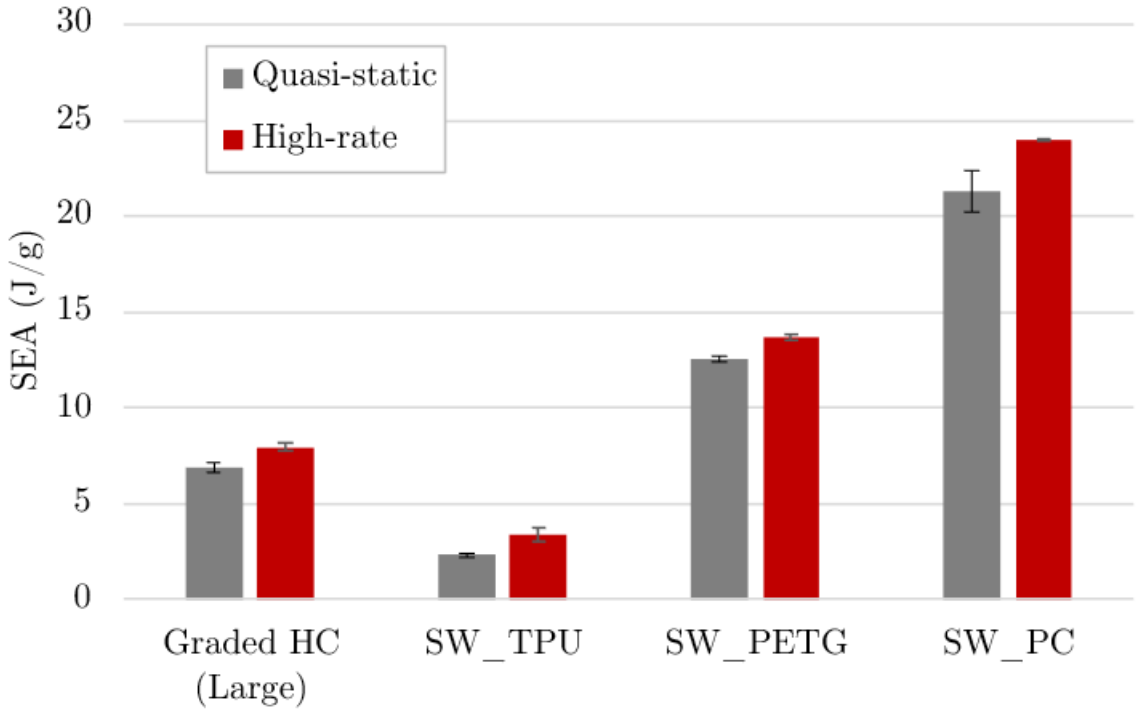

Figure 30: Obtained SEA values for two size graded honeycomb structures.

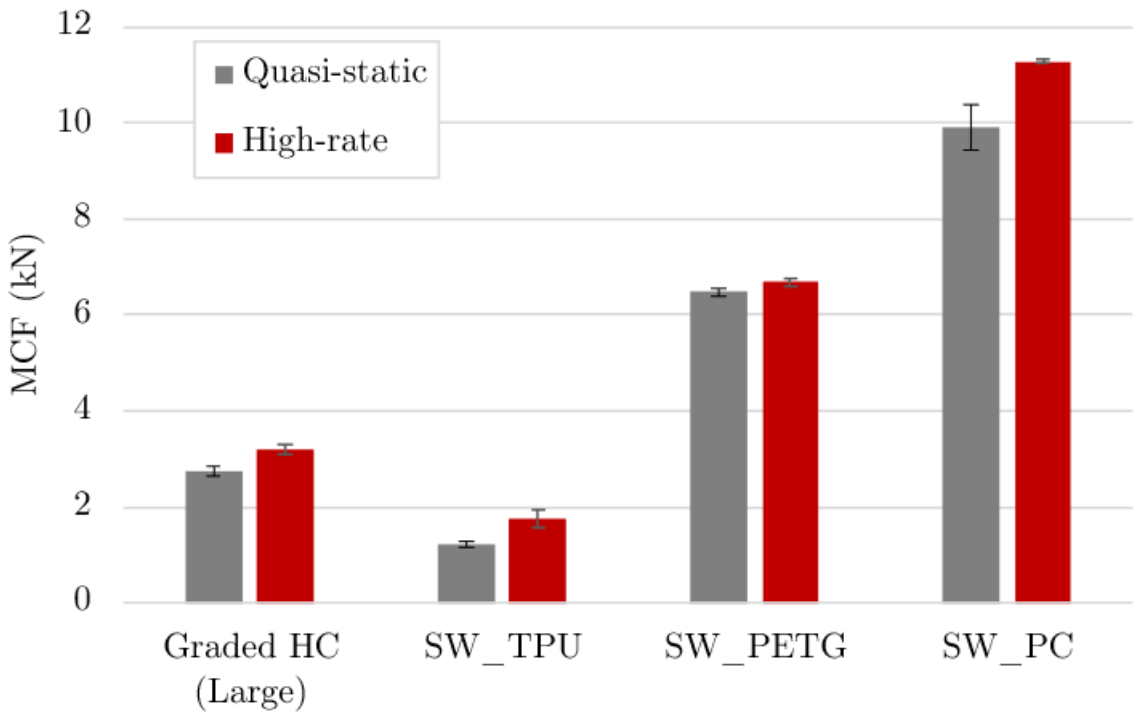

Figure 31: Obtained MCF values for two size multi-material honeycomb structures.

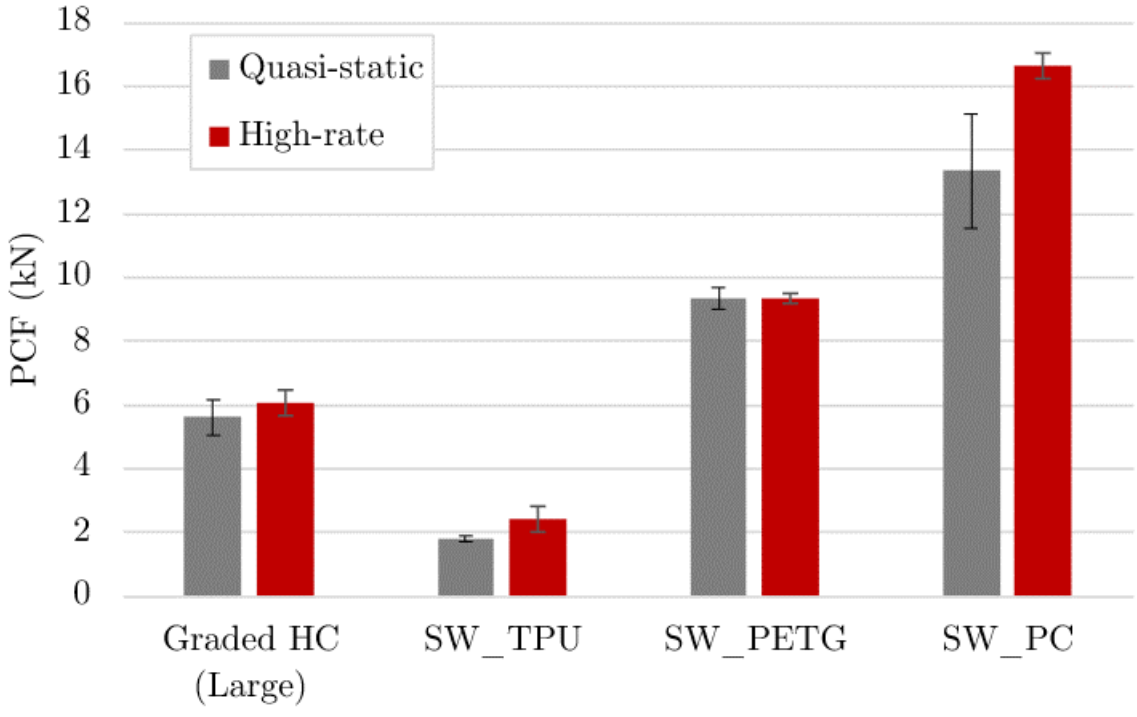

Figure 32: Obtained PCF values for two size multi-material honeycomb structures.

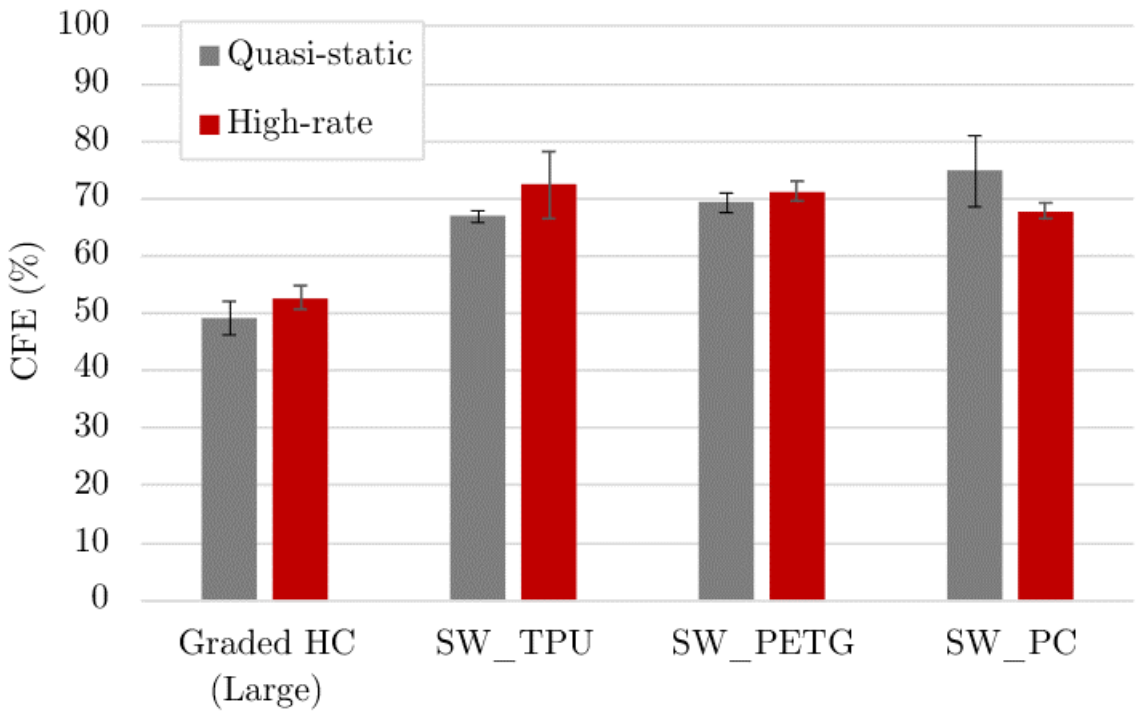

Figure 33: Obtained CFE values for two size multi-material honeycomb structures.

Analysing the obtained crahworthiness indexes, it becomes clear the superiority of the developed spider web structure as an energy absorption structure. With the exception of the TPU structure, all the spider web graded EAS were able to absorb a higher amount of energy, for the same structural mass. Nevertheless, TPU structure showed the highest efficiency, under high-rate loading. This comes as a result of identical values of peak and mean crushing force.

When submitted to impact, the TPU spider web structure outperformed the PC and PETG counterpart. It was able to dissipate the energy of impact over a longer period of time, thus resulting in more phased, lower energy absorption rate. Due to its higher stiffness and higher loads required to deform it, the PC structure promoted a higher energy absorption rate by stopping the impactor by sustaining a low compression stroke. It is important to mention that the performance of these structures depends mainly on the magnitude of the impact energy, as PC might attain better performance than the TPU counterpart for higher impact energy values. Figures 34 and 35 show the crashworthiness parameters calculated for the performed impact tests.

The graded spider web configuration reveals to be more suitable than the multi-material counterpart for energy absorption capabilities, due to its superior performance under the different loading regimes and higher stability, leading to a more predictable collapse mode under high loading rates. Furthermore, for implementation in a real application the production of a single material part would more feasible, when comparing to a multi-material counterpart.

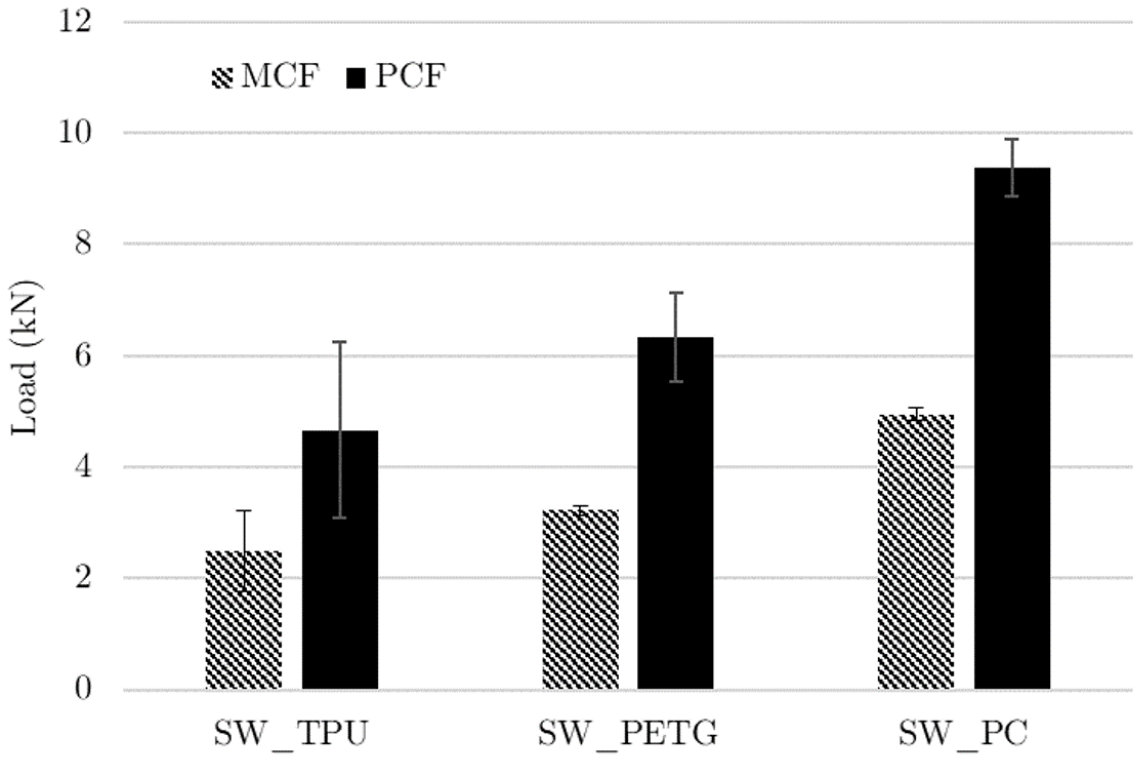

Figure 34: Comparison between obtained MCF and PCF values for single-material spider web graded structures.

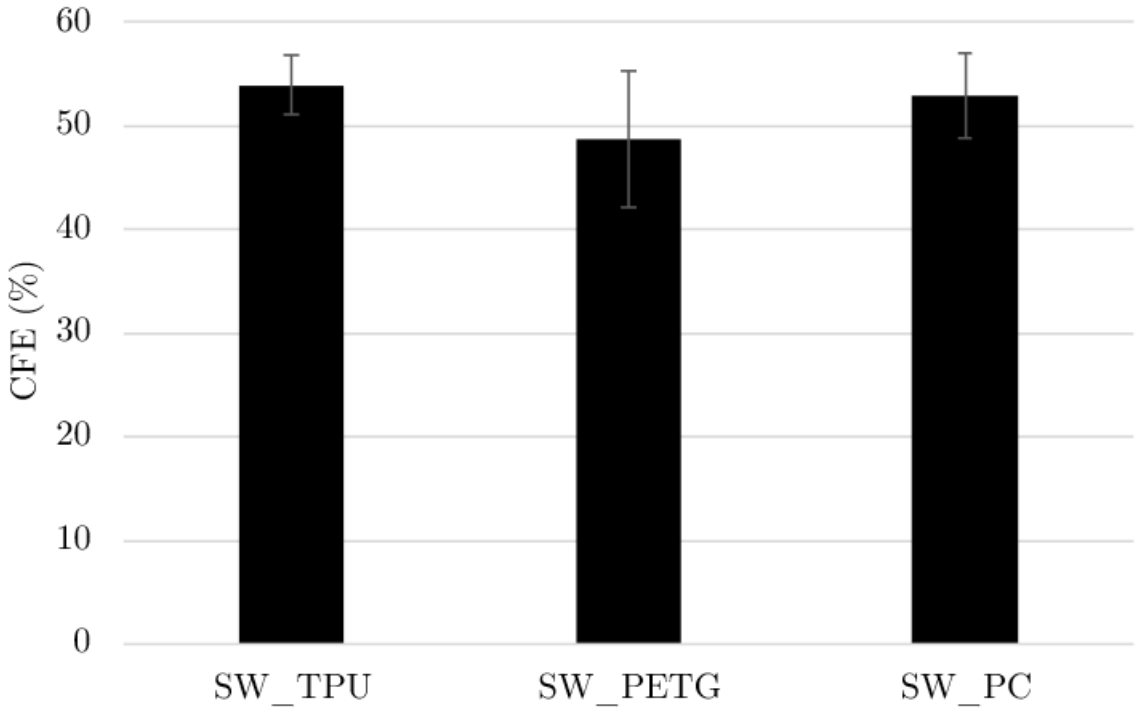

Figure 35: Comparison between obtained CFE values for single-material spider web graded structures.

4 Conclusions and future work

Two different EAS concepts, with variable/graded stiffness along their length, were developed in this work. This variation is achieved through changes of material properties and modification of the structural density, applied to honeycomb and a spider web structure, respectively.

The influence of stiffness grading was assessed by testing the developed honeycomb multi-material structure to compression, under different loading rates, and comparing its behaviour with uniform, single material counterparts. The stiffness grading of the honeycomb structure allowed the delay of densification, contributing for the energy absorption, when compared to PETG and TPU uniform counterparts. Futhermore, it was noticed that the maximum load generated during the compression is material depedendent and does not account for it proportion.

Although no significant improvement was made with use of multiple materials, when compared with the uniform PC counterpart, the multi-material structure was able be as efficient at dissipating the impact energy. However, PETG revealed a high sensitivity to strain rate by showing a remarkably brittle behaviour under impact, that hampered the performance of the multi-material honeycomb structure. The use of material other than PETG has the potential to result in significant performance improvements.

Furthermore, the size effect was also assessed by testing a scaled multi-material honeycomb structure. A proportional relation between energy absorption capabilities of scaled counterparts was found. The increase of structure's size lead to an unstable compression with associated buckling and further detachment of the structure parts, under high impact loading.

Concerning the structural geometry, the spider web specimens revealed a higher potential for energy absorption applications, when compared to the developed honeycomb counterparts, attaining a higher energy absorption capability and efficiency. When subjected to impact, the TPU structure stood out by effectively dissipating the total energy of impact over a longer period of time, what would result in a lower stress being transmitted to adjacent components that it would be protecting.

As a future project, a numerical analysis of a multi-material structure under impact can provide valuable insight for improvement of this concept, by exploring the ideal material properties for enhanced energy absorption performance.

References

[1] N.S.B. Yusof, S.M. Sapuan, M.T.H. Sultan, M. Jawaid, and M.A. Maleque. Design and materials development of automotive crash box: A review. *Ciência amp; Tecnologia dos Materiais*, 29(3):129–144, 2017.

[2] N.A.Z. Abdullah, M.S.M. Sani, M.S. Salwani, and N.A. Husain. A review on crashworthiness studies of crash box structure. *Thin-Walled Structures*, 153:106795, 2020.

[3] Guohua Zhu, Guangyong Sun, Hang Yu, Shunfeng Li, and Qing Li. Energy absorption of metal, composite and metal/composite hybrid structures under oblique crushing loading. *International Journal of Mechanical Sciences*, 135:458–483, 2018.

[4] James Meredith, Richard Ebsworth, Stuart R. Coles, Benjamin M. Wood, and Kerry Kirwan. Natural fibre composite energy absorption structures. *Composites Science and Technology*, 72(2):211–217, 2012.

[5] Carlo Boursier Niutta, Raffaele Ciardiello, and Andrea Tridello. Experimental and numerical investigation of a lattice structure for energy absorption: Application to the design of an automotive crash absorber. *Polymers*, 14(6):1116, 2022.

[6] Fatah Habib, Pio Iovenitti, Syed Masood, Mostafa Nikzad, and Dong Ruan. Design and evaluation of 3d printed polymeric cellular materials for dynamic energy absorption. *The International Journal of Advanced Manufacturing Technology*, 103(5–8):2347–2361, 2019.

[7] Ashok Dara, A Johnney Mertens, and M V Raju Bahubalendruni. Characterization of penetrate and interpenetrate tessellated cellular lattice structures for energy absorption. *Proceedings of the Institution of Mechanical Engineers, Part L: Journal of Materials: Design and Applications*, 237(4):906–913, 2022.

[8] B Garrido Silva, F Alves, M Sardinha, L Reis, M Leite, A M Deus, and M Fatima Vaz. Functionally graded cellular cores of sandwich panels fabricated by additive manufacturing. *Proceedings of the Institution of Mechanical Engineers, Part L: Journal of Materials: Design and Applications*, 236(9):1814–1828, 2022.

[9] Diogo Pereira, Frederico PD Alves, Luis Reis, Marco Leite, Augusto M Deus, Manuel Sardinha, and M Fatima Vaz. Cellular lattice cores of sandwich panels fabricated by additive manufacturing: Effect of dimensions and relative density on mechanical behaviour. *Proceedings of the Institution of Mechanical Engineers, Part L: Journal of Materials: Design and Applications*, 237(5):1188–1201, 2022.

[10] Oyindamola Rahman and Behrad Koohbor. Optimization of energy absorption performance of polymer honeycombs by density gradation. *Composites Part C: Open Access*, 3:100052, 2020.

[11] Simon R.G. Bates, Ian R. Farrow, and Richard S. Trask. Compressive behaviour of 3d printed thermoplastic polyurethane honeycombs with graded densities. *Materials amp; Design*, 162:130–142, 2019.

[12] Yuze Nian, Shui Wan, Mo Li, and Qiang Su. Crashworthiness design of self-similar graded honeycomb-filled composite circular structures. *Construction and Building Materials*, 233:117344, 2020.

[13] A. Praveen Kumar, M. Shunmugasundaram, S. Sivasankar, and L. Ponraj Sankar. Numerical analysis on the axial deformation and energy absorption behaviour of tri-tubular structures. *Materials Today: Proceedings*, 27:866–870, 2020.

[14] Abraham Segade, Alvaro J. Bolano, José A. López-Campos, Enrique Casarejos, J. R. Fernández, and J. A. Vilán. Study of a crash box design optimized for a uniform load profile. 2018.

[15] F. N. Habib, P. Iovenitti, S. H. Masood, and M. Nikzad. Cell geometry effect on in-plane energy absorption of periodic honeycomb structures. *The International Journal of Advanced Manufacturing Technology*, 94(5–8):2369–2380, 2017.

[16] Hafizur Rahman, Ebrahim Yarali, Ali Zolfagharian, Ahmad Serjouei, and Mahdi Bodaghi. Energy absorption and mechanical performance of functionally graded soft–hard lattice structures. *Materials*, 14(6):1366, 2021.

[17] Ngoc San Ha and Guoxing Lu. A review of recent research on bio-inspired structures and materials for energy absorption applications. *Composites Part B: Engineering*, 181:107496, 2020.

[18] Chukwuemeke William Isaac and Fabian Duddeck. Current trends in additively manufactured (3d printed) energy absorbing structures for crashworthiness application – a review. *Virtual and Physical Prototyping*, 17(4):1058–1101, 2022.

[19] G. Lu and T. X. Yu. *Energy absorption of structures and materials*. Woodhead, 2003.